INL/RPT-25XXXX

NEAMS

Advancing Thermal-Hydraulic Modeling Capabilities for Molten Salt Reactors in Pronghorn

M2 Report

AUGUST 2024

Mauricio Tano, Ramiro Freile, Victor Coppo Leite

Thermal Fluids Systems Methods and Analysis

Mengnan Li, Joshua Hansel
Guillaume Giudicelli, Lise Charlot

Computational Frameworks

Idaho National Laboratory

Battelle Energy Alliance manages INL for the U.S. Department of Energy's Office of Nuclear Energy

INL/RPT-25XXXX

Advancing Thermal-Hydraulic Modeling Capabilities for Molten Salt Reactors in Pronghorn

M2 Report

Mauricio Tano, Ramiro Freile, Victor Coppo Leite
Thermal Fluids Systems Methods and Analysis
Mengnan Li, Joshua Hansel
Guillaume Giudicelli, Lise Charlot
Computational Frameworks

August 2024

Idaho National Laboratory
Advanced Scientific Computing
Idaho Falls, Idaho 83415

http://www.inl.gov

Prepared for the
U.S. Department of Energy
Office of Nuclear Energy
Under DOE Idaho Operations Office
Contract DE-AC07-05ID14517

Page intentionally left blank

ABSTRACT

This work focuses on advancing the modeling and simulation capabilities for Molten Salt Reactors (MSRs) within Pronghorn, addressing key thermal-hydraulic challenges that must be addressed for the safe and efficient operation of these advanced reactors. This report summarizes the development and validation of the following new models in Pronghorn: (i) two-equation RANS turbulence models, (ii) near-wall turbulence corrections due to curvature and roughness, and (iii) multidimensional two-phase drift-flux models. For each of these cases, along with the experimental validation, an application study of interest to MSRs is presented. In addition, this report also presents recent improvements in the domain-overlapping coupling between Pronghorn and SAM to address the cases of weakly compressible flow and flow reversal. Finally, an MSR action that greatly simplifies the setup of MSR models using NEAMS tools is described.

SUMMARY

This work advances the modeling and simulation capabilities for MSRs within Pronghorn, focusing on key thermal-hydraulic challenges essential for reactor operation. This report summarizes the following developments and validation activities:

1. Turbulence modeling capabilities of Pronghorn have been extended with the integration of two-equation k-ϵ and k-ω-SST Reynolds-Averaged Navier-Stokes (RANS) turbulence models. These models have been validated against experimental data and applied and benchmarked to thermal-hydraulic models in an open-source model of the Molten Chloride Reactor Experiment (MCRE).

2. Corrections for wall roughness and curvature effects have been introduced for near-wall turbulence modeling. This is particularly relevant due to the corrosive nature of molten salts and complex geometries in MSRs. These corrections improve the accuracy of near-wall flow predictions, which are validated by experimental comparisons. The effect of these corrections is analyzed for modeling the operation of the open-source version of the MCRE model.

3. A multidimensional two-phase drift-flux model has been implemented to address the behavior of gas bubbles in MSRs. This model resolves the void fraction and interfacial concentration for two-phase flow. The models are verified against analytical solutions and validated against experimental data. The models are then applied to study the effect of model dimensionality on void distribution and operating metrics for the Molten Salt Reactor Experiment (MSRE).

4. The domain-overlapping coupling between Pronghorn and SAM has been improved and extended to weakly compressible flows and flow reversal scenarios. These improvements are demonstrated via incompressible and weakly-compressible simulations of unheated and heated pipes and compared against an analytical solution. Also, the flow reversal is demonstrated for a loop with a pump that inverts its pressure head.

5. An MSR-specific action has been developed in Pronghorn to simplify the setup of MSR models using the NEAMS toolkit. This new input syntax reduces setup complexity, increasing accessibility and efficiency in MSR modeling. The contributions of this thesis enhance Pronghorn's capability for MSR modeling by simplifying simulation workflows.

The contributions of this work enhance the capability of Pronghorn for MSR modeling by addressing thermal-hydraulic challenges through the development and validation of new models, improvements in domain coupling, and the simplification of simulation workflows. These advancements push the boundaries of current MSR simulation capabilities, supporting the design and analysis of safer and more efficient MSR technologies.

ACKNOWLEDGMENTS

This report was authored by a contractor of the U.S. Government under Contract DE-AC07-05ID14517. Accordingly, the U.S. Government retains a non-exclusive, royalty-free license to publish or reproduce the published form of this contribution, or allow others to do so, for U.S. Government purposes. Funding was provided by the Nuclear Energy Advanced Modeling and Simulation program.

This research made use of the resources of the High Performance Computing Center at Idaho National Laboratory, which is supported by the Office of Nuclear Energy of the U.S. Department of Energy and the Nuclear Science User Facilities under Contract No. DE-AC07-05ID14517.

Page intentionally left blank

CONTENTS

FIGURES

TABLES

Page intentionally left blank

ACRONYMS

CFD	Computational Fluid Dynamics
DOE	United States Department of Energy
INL	Idaho National Laboratory
L-MCR	Lotus Molten Chloride Reactor
LES	Large Eddy Simulations
MOOSE	Multiphysics Object-Oriented Simulation Environment
MSFR	Molten Salt Fast Reactor
MSR	Molten Salt Reactor
MSRE	Molten Salt Reactor Experiment
NEAMS	Nuclear Energy Advanced Modeling and Simulation
RANS	Reynolds-Average Navier Stokes

Page intentionally left blank

Advancing Thermal-Hydraulic Modeling Capabilities for Molten Salt Reactors in Pronghorn

M2 Report

1. INTRODUCTION

Advanced nuclear reactors propose innovative reactor designs and novel fuels and coolants. Among advanced reactors, Molten Salt Reactor (MSR)s present a potential paradigm shift in nuclear reactor design. These reactors utilize a molten salt to simultaneously serve as fuel and coolant. This fundamental shift in the fuel configuration introduces many engineering challenges that are both unique to MSRs and critical to their successful deployment. This work has focus primarily on the thermal-hydraulics challenges associated to modeling these reactors. However, it must be noted that addressing these challenges requires a deep understanding of the complex MSR systems that involve coupled neutronics, thermal-hydraulics, materials science, and system dynamics issues, all of which are crucial to ensuring the safe and efficient operation of these reactors. The next subsections present in more detail each of the challenges identified for MSR modeling from the thermal-hydraulics perspective.

1.1. Thermal-Hydraulics Challenges in MSR Engineering and Design

Thermal-hydraulics in MSRs are primarily related to the liquid nuclear fuel employed by these reactors. These challenges are related to the thermophysical properties of the molten salts, the dynamic behavior of liquid-fuel systems, and the relatively complex flow geometries and operational conditions typical of MSRs. The following subsections provide a review of the main challenges identified.

1.1.1. Fluid Dynamics and Heat Transfer

In MSRs, the neutronics power source is directly deposited in the liquid nuclear fuel. This results in a highly coupled system where fluid dynamics and heat transfer are tightly linked with reactor neutronics. Due to this tight coupling, a high accuracy is required for modeling the flow and temperature fields or, otherwise, errors in thermal-hydraulics modeling can propagate to considerably affect the reactor dynamics. Note that this is different than solid fuel reactors for which thermal-hydraulics plays a delayed role in fuel cooling and hence, does not play a fundamental role in short-term reactor dynamics.

One key challenge related to increasing the accuracy of resolving thermal-hydraulics fields in MSRs is capturing the turbulent flow fields in the liquid nuclear fuel. Either in the thermal version of MSRs, which involve internal moderator structures in the core, or the fast version of MSR, where the core is designed as an opened cavity, the flow through the primary loop of the MSR is highly turbulent. Hence, for neutronics-temperature feedback and precursor transport, models must capture accurately the effective mixing and the resulting velocity and temperature distributions in this turbulent flow. Additionally, for routine design, engineering, and operation support tasks, these models should have reasonable run-times and associated computational resources.

Another challenge for thermal-hydraulics modeling of MSRs is the presence of bubbles generated during the operation of MSRs. These bubbles may appear as a by-product of MSR operation, due to volatilizing fission gases, entertainment into the fuel of cover gases, or may be intentionally added to the salt to enhance

salt degassing via sparging operations. The bubbles in the salt have implications in reactor dynamics and in species transport in MSRs. For reactor dynamics, the added void of bubbles reduces the reactivity of the reactor core and adds compressibility to the fuel salt that changes the density and temperature feedback coefficients. For species transport, gas bubbles consist of nucleation sites for insoluble species in the liquid fuel. These fission products are either transported as gases inside the bubbles or adhere at the liquid-gas interfaces. Hence, accurately capturing the generation and distribution of void fraction in MSRs is a fundamental task that must preceed refined computations of reactor physics and species accountancy at the reactor core.

Another challenge is the accurate modeling of heat transfer in the presence of complex MRS geometries. MSRs often include intricate structures and arrangements of heat exchangers, piping, and pumps, each contributing to the overall thermal-hydraulic performance of the system. For routine engineering analyses, these arrangements must be simplified into a flow treatment that can be solved without involving substantial computational resources and the need of detailed component specifications. For this purpose, correlations are generally needed for modeling momentum, heat sources, and sinks in these components. However, this is generally challenging for molten salt as its low thermal diffusivity entails a slow development of the thermal-boundary layers, which complicates the homogenized momentum and heat transfer approach proposed by correlations. To address these issues, the current reasoning is that thermal-hydraulics codes must rely on multi-scale approaches, where high-fidelity, engineering-scale, and systems codes are coupled either offline or online to accurately modeling MSR systems.

1.1.2. Corrosion and Material Degradation

In MSRs, the continuous circulation of molten salts at high temperatures poses significant challenges related to corrosion and material degradation. The molten salts, while being adequate heat carriers, can be highly chemically reactive with structural materials if the Redox potential of the salt is not properly handled. Redox potential control becomes particularly challenging due to the conditions in the liquid fuel created by the high neutron flux and radiation environment typical of MSR operation. The degradation of materials not only compromises the reactor's structural integrity but also alters the thermal-hydraulic performance due to changes in surface roughness, flow dynamics, and heat transfer properties. Additionally, appropriate modeling of the flow field near the reactor structures is fundamental for determining the temperature and chemical composition of the salt in contact with the walls, which, ultimately, determine the transport mechanisms leading to corrosion.

A key challenge in addressing corrosion and material degradation in MSRs is the accurate prediction of material behavior over time. This prediction requires integrating thermal-hydraulics models with corrosion kinetics and material science. The conjugated effects created by flow-induced stresses, temperature gradients, and chemical reactions in the molten salt environment need to be understood to predict how materials will degrade under operational conditions. Corrosion can lead to localized hot spots, material embrittlement, and the potential release of radioactive materials out of the primary loop, all of which have direct implications for reactor safety and performance.

Another challenge is the development of corrosion-resistant materials and coatings that can withstand the aggressive environment within MSRs. These materials must maintain their mechanical and thermal properties over long operational periods. Thermal-hydraulics models must therefore be coupled with material degradation models to assess the effectiveness of these materials under various operational scenarios. This coupling allows for more accurate predictions of the reactor performance over time, considering both the gradual degradation of materials and the impact on heat transfer and fluid flow.

The presence of corrosion products in the molten salt further complicates the thermal-hydraulics modeling. These products can precipitate and form deposits on heat exchanger surfaces and within the reactor core,

leading to reduced heat transfer efficiency and potential flow blockages. The modeling of these effects requires detailed simulations of both the fluid dynamics and the chemical interactions between the molten salt and reactor materials. A multiscale approach is necessary to capture the complex interactions between corrosion processes and the thermal-hydraulic performance of MSRs, enabling more accurate predictions of long-term reactor behavior and the development of effective mitigation strategies.

1.1.3. System Integration and Control

In MSRs, system integration and control are needed for ensuring that the tightly coupled thermal-hydraulics, neutronics, and chemical processes are managed effectively to maintain safe and efficient reactor operation. The dynamic nature of MSR systems, characterized by the continuous flow of liquid fuel in the reactor primary and intermediate loops, the generation of gaseous fission products, and the heat exchange processes characterized by direct deposition of power in the fuel salt and cooling or heating at heat exchangers, demands control strategies that can respond rapidly to changes in reactor conditions.

One of the primary challenges in system integration and control is the real-time monitoring and regulation of key reactor parameters, such as temperature, pressure, flow rates, and reactivity. The coupling in MSRs results in that any perturbation in one parameter can have immediate and significant impacts on the others. For example, changes in the flow rate can directly affect the temperature distribution and, consequently, the reactivity of the reactor core. Accurate thermal-hydraulics modeling is therefore a fundamental component for developing control algorithms that can anticipate and compensate for these interactions, ensuring stable and safe reactor operation.

Another challenge is the integration of multiple subsystems, including the primary, intermediate, and secondary cooling loops, fuel processing units, and power conversion systems, into a cohesive operational framework. Each subsystem has its own thermal-hydraulic characteristics, and their interactions must be managed to prevent cascading failures or operational inefficiencies. For example, the efficiency of heat exchangers in transferring heat from the molten salt to the secondary coolant is critical for maintaining optimal reactor performance. Any degradation in heat exchanger performance, due to fouling or corrosion, can lead to elevated temperatures in the reactor core, increasing the risk of material failure or fuel degradation. Hence, multiscale models are needed to capture both the integral behaviour of the reactor plant and the thermal-hydraulics effects associated with rapid reactor dynamics in the reactor core.

To address these challenges, advanced control systems must be developed that can handle the multiscale, multiphysics nature of MSR operations. These systems should be capable of integrating real-time data from various sensors, running predictive thermal-hydraulic models, and making adjustments to reactor operation in real-time. The development of these control systems requires high-accuracy models for understanding of the thermal-hydraulic behavior of the MSR, including the effects of transient conditions such as startup, shutdown, and load-following operations. Additionally, the integration of these control systems with safety systems is critical for ensuring that any deviations from normal operation are detected early and mitigated effectively.

1.1.4. Safety and Accident Analysis

Safety and accident analysis in MSRs is linked to the thermal-hydraulic behavior of the reactor, particularly under off-normal and accident conditions. The design of MSRs, where the fuel is in a liquid state and directly involved in the heat removal process, presents both opportunities and challenges for ensuring reactor safety. The ability of the liquid fuel to flow and redistribute heat passively is a key safety feature, but it also introduces

complications in predicting the reactor's response to transient and accident scenarios.

One of the primary challenges in safety analysis is accurately modeling the progression of accidents, such as loss of flow, reactivity insertion, or loss of heat sink events. In these scenarios, the thermal-hydraulic response of the reactor is critical in determining the transient outcome. For example, in a loss of flow accident, the ability of the molten salt to continue removing heat via natural circulation is dependent on the accurate prediction of fluid dynamics and heat transfer within the reactor. Similarly, in reactivity insertion scenarios, the rapid change in reactor power must be matched by equally rapid adjustments in heat removal to prevent overheating and potential fuel damage.

Another significant challenge is the modeling of potential fuel salt solidification during accidents. If the temperature of the molten salt drops below its freezing point, it could solidify within the reactor or coolant loops, leading to blockages that hinder heat removal and potentially cause localized overheating. The thermal-hydraulics models must therefore account for phase change phenomena and the associated changes in flow dynamics and heat transfer.

The presence of gas bubbles and their interaction with the liquid fuel adds another layer of complexity to safety analysis. During accidents, the formation and redistribution of gas bubbles can affect both reactivity and heat transfer. For instance, an increase in void fraction due to gas bubble formation can lead to a reduction in reactivity, but it also changes the thermal properties of the coolant, potentially leading to uneven temperature distributions and hot spots. Accurate modeling of these multiphase flow dynamics is essential for predicting the reactor's behavior under accident conditions and for designing effective safety systems.

Finally, the integration of thermal-hydraulic models with neutronics and chemical kinetics is crucial for a comprehensive safety analysis. The tightly coupled nature of MSRs means that changes in one domain can have immediate and significant impacts on others. For example, a change in reactivity due to fuel composition changes must be matched by corresponding adjustments in heat removal to maintain safe operating temperatures. Advanced simulation tools that integrate these various physical phenomena are necessary for accurately predicting the reactor's response to accidents and for designing robust safety systems that ensure the continued protection of the reactor and the surrounding environment.

1.1.5. Thermal-Hydraulics Model Validation Challenges

One of the foremost challenges for thermal-hydraulics validation of MSR models is the scarcity of high-fidelity experimental data specific to the thermal-hydraulic conditions in MSRs. The operational history of MSRs is limited, and much of the available data comes from older experiments like the Molten Salt Reactor Experiment (MSRE), which may not fully capture the conditions in modern MSR designs. This lack of comprehensive experimental benchmarks makes it difficult to validate models across the diverse operating regimes of MSRs, particularly under the extreme temperature and flow conditions typical of these reactors.

The multiphase nature of the flow within MSRs introduces additional complexity to thermal-hydraulic model validation. The presence of gas bubbles, either from fission gas release or intentional sparging, significantly impacts the fluid dynamics and heat transfer processes. Validating models that accurately predict the formation, distribution, and behavior of these bubbles is challenging because experimental data on gas-liquid interactions within molten salts is limited. The complexity of capturing the void fraction and its effects on reactor behavior, such as changes in reactivity and heat transfer efficiency, requires detailed experimental setups that are currently scarce.

Another significant challenge lies in the accurate modeling of heat transfer in the presence of the unique geometrical configurations found in MSRs. The molten salt coolant interacts with a variety of structural materials and components, including heat exchangers, piping, and pumps, all of which contribute to the overall

thermal-hydraulic behavior of the system. The low thermal diffusivity of molten salts means that heat transfer processes are slower and more complex compared to other coolants, making it difficult to develop and validate models that can capture these nuances accurately. This challenge is compounded by the need to simplify these complex geometries into manageable computational models without losing the essential physics, which is often achieved through the use of empirical correlations that require validation against experimental data.

The dynamic behavior of thermal-hydraulic systems in MSRs, particularly under transient conditions, further complicates model validation. The ability of the molten salt to flow and redistribute heat during transients, combined with the potential for significant changes in fluid properties such as viscosity and density with temperature and depletion during operation, requires models that can accurately simulate these rapid changes. However, obtaining experimental data under these dynamic conditions is difficult, and existing data may not fully represent the operational challenges of modern MSRs. This makes it challenging to validate models for scenarios such as rapid power changes, loss-of-flow accidents, or other transients that are critical for reactor safety.

While this work uses data from other fluids to validate the thermal-hydraulics models, there is a need for dedicated experimental programs focused on the thermal-hydraulic aspects of MSRs to address these challenges. These programs should aim to provide high-quality data under a variety of conditions, including steady-state and transient operations, to cover the range of scenarios that MSRs might encounter. Additionally, advancements in experimental techniques, such as high-fidelity measurements of void fraction and temperature distributions, are crucial for improving the accuracy of the models. Coupling these experimental efforts with advanced computational techniques, such as uncertainty quantification and sensitivity analysis, can help identify the most critical areas for validation and improve the reliability of thermal-hydraulic models for MSRs.

1.2. Contributions to Address the MSR Problematic

This report describes the contributions made this fiscal year to advance the thermal hydraulics capabilities of the NEAMS tool Pronghorn for MSR modeling. It is presented as a compendium of article pre-prints or independent sections each related to a specific topic. The articles presented in this compendium collectively address the general problematic of MSR modeling and simulation, with a specific focus on overcoming the thermal-hydraulic challenges outlined above. Through the development of advanced modeling techniques, improved coupling methodologies, and streamlined workflows, these works push the boundaries of current MSR research and contribute to the advancement of safe and efficient MSR designs.

1.2.1. Turbulence Models for MSR Applications

Problematic: The accurate prediction of fluid flow and heat transfer in MSRs is heavily dependent on the ability to model turbulence accurately. Traditional turbulence models, such as those used for solid-fuel reactors, are often inadequate for capturing the complex flow behaviors in MSRs, where turbulent mixing, heat transfer, and fluid-structure interactions play a critical role.

Importance for MSR Modeling: Turbulence in MSRs affects not only the heat transfer efficiency but also the distribution of neutron precursors and fission products within the molten salt. Inaccurate turbulence modeling can lead to significant errors in predicting the reactor's thermal and neutronic behavior, potentially compromising safety and performance.

Key Developments: This article introduces new turbulence models tailored specifically for MSR conditions, including weakly compressible Reynolds-Average Navier Stokes (RANS) equations and a refined

treatment of turbulent Prandtl numbers. These models are validated against experimental data and shown to provide improved predictions of fluid flow and heat transfer in MSR environments.

Highlights: The article demonstrates the successful development and validation of RANS models in Pronghorn. Also, an application to the Lotus Molten Chloride Reactor (L-MCR), which is a reactor model developed for numerical studies purposes based open-source specifications of the Molten Chloride Reactor Experiment, is presented, highlighting their ability to capture the interactions between fluid dynamics and heat transfer. The use of weakly compressible RANS equations allows for more accurate simulations of MSR operating conditions, particularly in regions with high thermal gradients.

Advancement Beyond the State of the Art: This work advances the state of the art by providing MSR-specific turbulence models that enhance the predictive capabilities of thermal-hydraulic simulations. These models enable more accurate assessments of reactor performance and safety, contributing to the development of more reliable MSR designs.

1.2.2. Near-Wall Turbulence Modeling

Problematic: Molten Salt Reactors (MSRs) pose unique challenges in the context of near-wall turbulence modeling due to the presence of significant temperature gradients, low thermal diffusivity of molten salts, and the corrosive nature of these salts, which can lead to wall roughness and degradation. Standard near-wall turbulence models, typically employed in Computational Fluid Dynamics (CFD) simulations, are often inadequate for accurately capturing the complex flow phenomena near the reactor walls in MSRs. Specifically, the effects of wall roughness and curvature, which are prevalent in MSRs due to corrosion and the reactor's intricate geometries, are not well-accounted for in traditional models.

Importance for MSR Modeling: Near-wall turbulence directly influences the heat transfer, shear stress, and fluid flow patterns adjacent to the reactor walls, which are critical parameters for ensuring the reactor's thermal and structural integrity. Inaccurate modeling of near-wall turbulence can lead to significant errors in predicting wall temperatures, heat fluxes, and the overall behavior of the reactor under various operating conditions. This, in turn, can compromise the reactor's safety, efficiency, and lifespan.

Key Developments: This article introduces a set of corrections to the standard near-wall turbulence models implemented in the Multiphysics Object-Oriented Simulation Environment (MOOSE) framework, specifically addressing the effects of wall roughness and transverse curvature. The corrections include a roughness model based on the equivalent sand grain roughness approach, which adjusts the velocity profiles near rough walls to account for the increased friction and altered turbulence structure. Additionally, a transverse curvature correction is introduced, which modifies the turbulent viscosity and velocity profiles to account for the effects of swirling flows and curved surfaces commonly found in MSR designs.

Highlights: The study includes a comprehensive validation of the proposed corrections against experimental data, including comparisons with the Moody chart for friction factors in rough pipes and detailed simulations of swirling flows in curved geometries. The corrections are then applied to the modeling of a generic MSR, specifically the L-MCR, to assess their impact on the reactor's operational parameters. The results demonstrate that the roughness corrections lead to significant changes in the predicted mass flow rates and heat transfer characteristics, while the curvature corrections improve the accuracy of velocity and temperature predictions near the reactor walls.

Advancement Beyond the State of the Art: The developed corrections advance the state of near-wall turbulence modeling for MSRs by providing more accurate and physically representative models of the flow phenomena occurring near rough and curved walls. These improvements enable better predictions of the thermal-hydraulic behavior of MSRs, particularly in regions where traditional models would fail to capture

the complexity of the flow. As a result, the corrected models contribute to the design and analysis of more reliable and efficient MSR systems, enhancing the safety and performance of these reactors.

1.2.3. Multiphase Flow and Species Tracking

Problematic: The behavior of gaseous phases in Molten Salt Reactors (MSRs), specifically the transport and accumulation of fission products such as xenon and krypton, poses significant challenges for reactor safety and performance. These challenges are compounded by the complex interactions between the molten salt, the gas bubbles, and the reactor's operational parameters. Modeling these multiphase flow dynamics is crucial to accurately predicting the reactor's behavior under various conditions.

Importance for MSR Modeling: Precise modeling of multiphase flow and species transport is essential for controlling reactivity, managing heat transfer, and ensuring structural integrity within the reactor. Gaseous fission products can alter the fuel salt's density and temperature distribution, affecting the reactor's reactivity and potentially leading to power fluctuations or localized overheating. Without accurate modeling, these phenomena could lead to underestimation of radiation hazards, reduced reactor efficiency, and compromised safety.

Key Developments: This article presents a detailed two-phase flow model developed within the MOOSE framework, specifically tailored for MSRs. The model integrates a multidimensional drift-flux formulation with an interface area concentration model, providing a comprehensive tool for simulating the transport of gaseous fission products. This model advances beyond traditional one-dimensional and two-dimensional approaches by offering higher fidelity in capturing the complex interactions within the reactor core and plenum.

Highlights: The developed framework is applied to the MSRE, where it successfully predicts the distribution of void fractions and interface area concentrations under various operational scenarios. The results underscore the importance of incorporating both the fluid dynamics and chemical interactions in the modeling process to ensure accurate predictions of species transport and reactor behavior.

Advancement Beyond the State of the Art: This work significantly advances MSR modeling by introducing a robust, three-dimensional multiphase flow and species tracking framework. By enabling more accurate simulations of multiphase phenomena occurring within MSRs, this framework enhances safety assessments and optimizes reactor design, thereby pushing the boundaries of current modeling capabilities.

1.2.4. Improvements in Domain-Overlapping Coupling

Problematic: Coupling different physical domains, such as neutronics and thermal-hydraulics, is essential for accurate MSR simulations. Traditional coupling methods often rely on separate domain approaches, which can lead to inconsistencies and inaccuracies, particularly in regions with strong interactions between physical phenomena.

Importance for MSR Modeling: The ability to accurately couple different physical domains is crucial for capturing the full complexity of MSR behavior. Inconsistent coupling can lead to errors in predicting key reactor parameters, such as power distribution, temperature gradients, and fluid flow patterns, which are critical for both performance and safety.

Key Developments: This article introduces an improved domain-overlapping coupling method that ensures consistent data transfer between different simulation domains. The method is specifically designed to handle the complex interactions between neutronics and thermal-hydraulics in MSRs, providing more

accurate and robust simulations.

Highlights: The article demonstrates the effectiveness of the improved coupling method through its application to a range of MSR scenarios. The results show significant improvements in the accuracy and consistency of coupled simulations, particularly in regions with strong inter-domain interactions.

Advancement Beyond the State of the Art: By improving the accuracy and robustness of domain-overlapping coupling, this work enhances the ability to simulate complex MSR behaviors. This advancement is particularly important for ensuring that simulation results are reliable and consistent across different physical domains, contributing to more accurate reactor design and safety analysis.

1.2.5. Workflow Improvements for MSR Simulations

Problematic: Setting up simulations for coupled MSR problems is a complex and error-prone process, particularly for new users. The need to configure multiple physical domains and ensure consistency between them presents a significant barrier to effective modeling and analysis.

Importance for MSR Modeling: Streamlining the workflow for MSR simulations is crucial for enabling broader adoption of advanced modeling tools and ensuring consistent, high-quality simulation results. Simplified workflows reduce the potential for errors, increase user efficiency, and make advanced MSR modeling accessible to a wider audience.

Key Developments: This section introduces a simplified input syntax for coupled neutronics and thermal-hydraulics simulations in MSRs. The new syntax significantly reduces the complexity of the setup process, replacing over 100 lines of input with just 14, while maintaining the flexibility and power of the underlying simulation tools.

Highlights: The simplified workflow is demonstrated through its application to a Molten Salt Fast Reactor (MSFR) example, where it successfully streamlines the setup process without compromising simulation accuracy or detail. The new syntax is shown to be less error-prone and more user-friendly, making it easier for users to set up and run complex coupled simulations.

Advancement Beyond the State of the Art: By reducing the complexity of the simulation setup process, this work lowers the barrier to entry for advanced MSR modeling and increases the accessibility of MOOSE-based tools. This advancement supports the broader adoption of these tools in the MSR research community and facilitates more efficient and accurate simulation workflows.

The articles presented in this compendium collectively enhance the capabilities of the Nuclear Energy Advanced Modeling and Simulation (NEAMS) tools for thermal-hydraulics modeling of MSRs. Each article addresses a specific aspect of the MSR modeling problematic, whether it be improving turbulence models, enhancing species tracking, refining domain coupling methodologies, or simplifying simulation workflows. Together, these contributions push the boundaries of what is possible in MSR simulation and analysis, enabling more accurate, reliable, and user-friendly tools.

The advancements presented in these articles not only improve the accuracy and reliability of MSR models but also make these tools more accessible and usable for a broader range of applications. By addressing the key challenges associated with MSR design and operation, these works collectively contribute to the development of safer, more efficient, and more advanced MSR technologies. As a result, the NEAMS toolkit is better equipped to support the design, safety analysis, and optimization of next-generation MSR technologies, advancing the state of the art in nuclear reactor modeling and simulation.

2. DEVELOPMENT AND VALIDATION OF RANS TURBULENCE MODELS IN MOOSE FOR SUPPORTING MSR MODEL DEVELOPMENT

This section reproduces a journal article that, as a part of this milestone, has been submitted to Nuclear Engineering and Design in August 2024.

2.1. Introduction

MSRs are liquid-fueled reactors in which the molten salt serves as both fuel and coolant. Therefore, accurate thermohydraulic modeling in MSRs is important, as it significantly affects not only power generation in the core, but also the transport of neutron precursors and chemical species in the liquid fuel, temperature gradients adjacent to the reactor structures, and mixing profiles in the reactor plume and core, among others. In this context, validated computational tools are needed for the design and engineering analysis of MSRs.

The Nuclear Energy Advanced Modeling and Simulation (NEAMS) program, sponsored by the United States Department of Energy (DOE), is charged with developing advanced modeling and simulation tools and capabilities to accelerate the deployment of advanced nuclear energy technologies, including MSRs. In terms of thermal-hydraulic modeling, the program supports three computational tools for MSR modeling. First, Nek-5000/NekRS, a computational tool that uses low numerical overhead spectral element methods and is adapted for high-fidelity numerical studies of fluid flow. Then the Systems Analysis Module (SAM), which is designed to perform system-level simulations of MSRs. Finally, Pronghorn, which targets the engineering scale in MSR modeling. This targeted engineering scale may vary depending on the reactors being studied. For example, for pebble cores, a porous media approximation may be sufficient for most required studies. However, for MSRs, especially for fast-spectrum design, where little to no internal structures are present in the reactor core, the engineering scale typically relies on CFD using RANS turbulence models that can typically run on a personal computer or small computer clusters. This work focuses on these turbulence models developed in Pronghorn and their validation for supporting engineering-scale analyses of MSRs.

Traditionally, thermohydraulic analyses of reactor cores have relied on system and subchannel codes, which use geometry-specific empirical correlations and cannot fully capture multidimensional effects in flow physics. In contrast, first-principles CFD codes can handle complex geometries and integrate different physics in stand-alone or coupled simulations. CFD is well suited to modeling 3D flows and heat transfer processes, making it increasingly valuable in the detailed study of 3D TH phenomena, especially in single-phase flow applications. This is particularly relevant for many MSR concepts that involve 3D recirculation and complex mixing profiles.

CFD modeling of MSR designs has been studied previously in the literature. For example, Gen-Foam has been applied to RANS CFD studies of the Molten Salt Reactor Experiment [10] and the Molten Salt Fast Reactor [11]. In addition, commercial CFD software such as STAR-CCM+ [12] and ANSYS Fluent [13] have also been used to model the fluid flow in MSRs. In general, without comparison with experimental data, RANS solutions have been found to provide reasonable results. However, some limitations of RANS models have been observed, such as the treatment of flow recirculation, detachment and reattachment of flow boundary layers, and flow phenomena associated with the large temperature gradients in the core. This has led to different approaches to correct standard RANS models. For example, nonlinear models have been developed to improve the accuracy of RANS models in pool-type MSRs [14]. However, the development of these models must be tailored to the specific reactor, making them inappropriate for general MSR modeling. In addition, higher fidelity models have also been applied to CFD modeling of MSRs. For example, Large Eddy Simulations (LES) of the Molten Salt Fast Reactor have been performed separately using NekRS [15]

and TrioCFD [16]. Although these higher fidelity models can provide relevant benchmark data for MSRs, their high computational cost makes them inappropriate for routine engineering applications.

A limitation of the literature studies on the use of RANS models is the lack of a structured approach to the implementation of these models on MSRs. To the best of the authors' knowledge, the turbulence models available in CFD codes, such as OpenFOAM, STAR-CCM+, or ANSYS Fluent, are applied to MSR modeling without prior evaluation of the performance of these models on experiments representative of the flow phenomena in MSRs. Although the turbulence models available in these codes have been tested to varying degrees, they often rely on approximations that make them usable for general flow configurations but may degrade their performance for MSR modeling. In particular, published work on MSRs generally omits key details that are important for evaluating the performance of RANS models, such as the formulation and mixing approach used for near-wall flow modeling and more detailed analyses of the evolution of the surrogate variables in the reactor, among others. Therefore, this work proposes a more systematic approach for the evaluation of RANS modeling in MSRs, using the L-MCR as an application.

The remainder of this article is organized as follows. In section 2.2., the detailed bulk and wall formulations of the $k-\epsilon$ and $k-\omega$ SST models recently implemented in the MOOSE at Idaho National Laboratory are presented. Then, in section 2.3., the validation of these models against concerted high-fidelity simulation data and experimental data is performed. This section examines the validation of these models for a channel, a backward step, and a swirling pipe flow, which are representative of the phenomena expected for the L-MCR. In the following section 2.4., the performance of the RANS models is compared to LES studies of the L-MCR analyzing both hydraulic and thermal data. Finally, general recommendations for MSR RANS modeling based on this study are provided in section 2.5..

2.2. Modeling approach

This section is organized as follows. First, the Reynolds-averaged Navier-Stokes and energy conservation equations describing the fluid flow phenomena in MSRs are reviewed. Then, the two new RANS model implementations in MOOSE are reviewed. First, the standard $k-\epsilon$ model with the near-wall modeling implemented for momentum and energy conservation. Then, the $k-\omega$ SST model with corrections introduced for free shear, vortex stretching, and low Reynolds number effects.

2.2.1. Thermal-hydraulics modeling

The fluid flow and heat transfer in molten salt reactors (MSRs) are governed by the weakly-compressible RANS equations, which describe the conservation of mass, momentum, and energy for a turbulent flow. The RANS equations are obtained by decomposing the instantaneous flow quantities into mean and fluctuating components and then averaging the resulting equations. The weakly compressible formulations assumes that density is implicitly a function of temperature but not of pressure.

The conservation of mass (continuity equation) is given by:

$$\frac{\partial \overline{\rho}}{\partial t} + \frac{\partial \overline{\rho}\,\overline{u}_i}{\partial x_i} = 0 \tag{1}$$

where $\overline{\rho}$ is the mean density, $\overline{u}_i$ is the mean velocity component in the i-th direction, and x_i represents the spatial coordinates.

The conservation of momentum is described by the RANS equation:

$$\frac{\partial \overline{\rho} \overline{u}_i}{\partial t} + \frac{\partial \overline{\rho} \overline{u}_i \overline{u}_j}{\partial x_j} = -\frac{\partial \overline{p}}{\partial x_i} + \frac{\partial}{\partial x_j} \left(\overline{\tau}_{ij} - \overline{\rho u_i' u_j'} \right) \tag{2}$$

where $\overline{p}$ is the mean pressure, $\overline{\tau}_{ij} = \mu \left(\frac{\partial \overline{u}_i}{\partial x_j} + \frac{\partial \overline{u}_j}{\partial x_i} \right)$ is the mean viscous stress tensor, and $\overline{u_i' u_j'}$ is the Reynolds stress tensor, representing the effects of turbulence. In turbulent flows, the Reynolds stress tensor $\overline{\rho u_i' u_j'}$ is modeled using the Boussinesq approximation, which relates the Reynolds stresses to the mean velocity gradients through the turbulent dynamic viscosity μ_t:

$$\overline{\rho u_i' u_j'} = \mu_t \left(\frac{\partial \overline{u}_i}{\partial x_j} + \frac{\partial \overline{u}_j}{\partial x_i} \right) - \frac{2}{3} \overline{\rho} k \delta_{ij} \tag{3}$$

where k is the turbulent kinetic energy, and δ_{ij} is the Kronecker delta. The turbulent dynamic viscosity μ_t is a key parameter in turbulence modeling and is calculated using turbulence models such as the $k-\epsilon$ or $k-\omega$-SST models.

The energy conservation equation, which accounts for the heat transfer in the fluid, is given by:

$$\frac{\partial \overline{\rho} \overline{h}}{\partial t} + \frac{\partial \overline{\rho} \overline{u}_i \overline{h}}{\partial x_i} = \frac{\partial}{\partial x_i} \left(\frac{\lambda}{c_p} \frac{\partial \overline{T}}{\partial x_i} + \frac{\lambda_t}{c_p} \frac{\partial \overline{T}}{\partial x_i} \right) \tag{4}$$

where $\overline{h}$ is the mean enthalpy, $\overline{T}$ is the mean temperature, λ is the thermal conductivity, c_p is the specific heat at constant pressure, and λ_t is the turbulent thermal conductivity. The turbulent thermal conductivity λ_t is related to the turbulent dynamic viscosity μ_t through the turbulent Prandtl number Pr_t:

$$\lambda_t = \frac{\mu_t c_p}{Pr_t} \tag{5}$$

The turbulent Prandtl number Pr_t is treated as a constant and we take $Pr_t = 0.9$ in these simulations.

These equations are integrated numerically in MOOSE using the finite volumes method. The closure equations for the turbulence models are introduced in the next sub-sections.

2.2.2. The $k-\epsilon$ turbulence model in MOOSE

The first model described is the $k-\epsilon$ turbulence model. This model introduces transport equations for the turbulent kinetic energy k and its dissipation rate ϵ, which are crucial for modeling the turbulent viscosity μ_t.

The transport equations for k and ϵ are given by:

$$\frac{\partial \overline{\rho} k}{\partial t} + \frac{\partial \overline{\rho} \overline{u}_i k}{\partial x_i} = \frac{\partial}{\partial x_j} \left(\left(\overline{\mu} + \frac{\overline{\mu_t}}{\sigma_k} \right) \frac{\partial k}{\partial x_j} \right) + P_k - \overline{\rho} \epsilon \tag{6}$$

$$\frac{\partial \overline{\rho} \epsilon}{\partial t} + \frac{\partial \overline{\rho} \overline{u}_i \epsilon}{\partial x_i} = \frac{\partial}{\partial x_j} \left(\left(\overline{\mu} + \frac{\overline{\mu_t}}{\sigma_\epsilon} \right) \frac{\partial \epsilon}{\partial x_j} \right) + C_{\epsilon 1} \frac{\epsilon}{k} P_k - C_{\epsilon 2} \overline{\rho} \frac{\epsilon^2}{k} \tag{7}$$

where P_k is the production term of turbulent kinetic energy, $\overline{\mu}$ is the dynamic viscosity, $\overline{\mu_t}$ is the turbulent viscosity, and σ_k, σ_ϵ, $C_{\epsilon 1}$, and $C_{\epsilon 2}$ are empirical constants.

The turbulent viscosity $\overline{\mu_t}$ is calculated as:

$$\overline{\mu_t} = \overline{\rho} C_\mu \frac{k^2}{\epsilon} \tag{8}$$

where C_μ is an empirical constant.

2.2.2.1. Bulk Treatment

In the bulk flow, the $k-\epsilon$ model assumes isotropic turbulence, where turbulent properties are uniform in all directions. The model calculates the turbulent viscosity and modifies the effective viscosity in the momentum equation accordingly. The transport of turbulent kinetic energy k and its dissipation rate ϵ is solved using the equations above, with source terms accounting for the production, dissipation, and diffusion of turbulence.

2.2.2.2. Near-Wall Treatment

The near-wall treatment is critical in the $k-\epsilon$ model, where the flow behavior near solid boundaries significantly affects the overall turbulence characteristics. This treatment is typically split into two regions: the sublaminar region ($y^+ < 11.25$) and the logarithmic region ($y^+ > 11.25$), where y^+ is the dimensionless wall distance.

In the **sublaminar region** ($y^+ < 11.25$), the viscous effects dominate, and the velocity profile is approximately linear. The velocity near the wall is expressed as:

$$u^+ = y^+ \tag{9}$$

where $u^+ = \overline{u}/u_\tau$, u_τ is the friction velocity, and ν is the kinematic viscosity. In this region, the production of turbulent kinetic energy P_k is typically small due to the dominance of viscous forces, and the dissipation ϵ is reduced by a damping function to account for the lower levels of turbulence.

In the **logarithmic region** ($y^+ > 11.25$), the flow transitions from viscous-dominated to turbulence-dominated, and the velocity profile follows the logarithmic law of the wall:

$$u^+ = \frac{1}{\kappa} \ln(y^+) + B \tag{10}$$

where κ is the von Kármán constant, and B is an empirical constant. In this region, the production term P_k increases, reflecting the enhanced turbulent activity. The dissipation rate ϵ is adjusted accordingly to balance the production and maintain a steady turbulent state.

For **temperature** in the near-wall region, the Jayatilleke treatment is applied to account for the effects of turbulence on thermal transport. The temperature profile is given by:

$$T^+ = \frac{T - T_w}{q_w/\rho c_p u_\tau} = \begin{cases} y^+ & \text{for } y^+ < 11.25 \\ \frac{1}{\kappa_t} \ln(y^+) + B_t + C_t & \text{for } y^+ > 11.25 \end{cases} \tag{11}$$

where T is the temperature, T_w is the wall temperature, q_w is the wall heat flux, c_p is the specific heat at constant pressure, κ_t is the thermal von Kármán constant, B_t is an empirical constant, and C_t is the Jayatilleke additive constant.

This near-wall treatment allows the $k-\epsilon$ model to accurately predict the velocity and temperature profiles within the boundary layer, which are essential for capturing the heat transfer and flow characteristics in MSRs.

2.2.3. The $k-\omega$ SST turbulence model in MOOSE

The $k-\omega$ SST (Shear Stress Transport) turbulence model is another widely used RANS model that combines the advantages of the $k-\epsilon$ and $k-\omega$ models. It solves two transport equations: one for the turbulent kinetic energy k and another for the specific dissipation rate ω, which is the ratio of ϵ to k.

The transport equations for k and ω are given by:

$$\frac{\partial \overline{\rho} k}{\partial t} + \frac{\partial \overline{\rho u}_i k}{\partial x_i} = \frac{\partial}{\partial x_j}\left(\left(\overline{\mu} + \frac{\overline{\mu_t}}{\sigma_k}\right)\frac{\partial k}{\partial x_j}\right) + P_k - \overline{\rho}\beta^* k\omega \tag{12}$$

$$\frac{\partial \overline{\rho} \omega}{\partial t} + \frac{\partial \overline{\rho u}_i \omega}{\partial x_i} = \frac{\partial}{\partial x_j}\left(\left(\overline{\mu} + \frac{\overline{\mu_t}}{\sigma_\omega}\right)\frac{\partial \omega}{\partial x_j}\right) + \alpha\frac{\omega}{k}P_k - \overline{\rho}\beta\omega^2 \tag{13}$$

where σ_k, σ_ω, α, β, and β^* are model constants.

The turbulent viscosity $\overline{\mu_t}$ is given by:

$$\overline{\mu_t} = \frac{\overline{\rho} k}{\omega} \tag{14}$$

2.2.3.1. Bulk Treatment

In the bulk region, the $k-\omega$ SST model uses a blending function to smoothly transition between the $k-\epsilon$ model, which is better suited for free shear flows, and the $k-\omega$ model, which is more accurate near walls. The model accounts for both turbulent production and dissipation and is particularly effective at capturing the effects of adverse pressure gradients and separating flows.

2.2.3.2. Near-Wall Treatment

For the near-wall treatment, the $k-\omega$ SST model directly resolves the flow all the way to the wall without the need for wall functions. This is one of the key advantages of the $k-\omega$ model over the $k-\epsilon$ model. The model automatically adjusts for low Reynolds numbers near the wall, ensuring that the turbulence is accurately captured in the viscous sublayer.

The near-wall thermal modeling follows the approach used in the $k-\epsilon$ model, as described in the previous section, but benefits from the increased accuracy of the $k-\omega$ SST model in capturing near-wall flows.

2.2.3.3. Free-Shear Corrections

The $k-\omega$ SST model includes corrections for free shear flows, where the blending function ensures that the model behaves like the $k-\epsilon$ model in regions of free shear, such as wakes and jets. This improves the model's accuracy in predicting the spreading rates of free shear layers.

2.2.3.4. Vortex-Stretching Corrections

Vortex-stretching corrections are implemented to enhance the model's ability to predict the intensification of turbulence due to vortex stretching, which is a key mechanism in the production of turbulence in shear flows. This correction improves the prediction of turbulent kinetic energy in regions with strong rotational effects.

2.2.3.5. Low Reynolds-Number Corrections

The $k-\omega$ SST model incorporates low Reynolds-number corrections that modify the turbulence equations near the wall to ensure accurate predictions in the viscous sublayer. These corrections are particularly important in MSRs, where the flow can experience significant variations in Reynolds number due to changes in operating conditions and coolant properties.

2.3. Model validation

2.3.1. Channel flow

The first validation case consists of a channel flow. The data used for this channel flow validation is coming from direct numerical simulations [1]. Several works have afterwards validated and checked this data. In particular, two cases are used for this validation with friction Reynolds numbers of $Re_\tau = 395$ and $Re_\tau = 590$. These cases are chosen since they are the ones in which the flow follows higher resemblance with the hydraulics conditions expected for the Lotus MSR.

A 2D model is employed in the RANS simulations. The computational meshes used in the simulations are depicted in Figure 1 and key parameters of computational meshes are detailed in Table 1. The mesh domain consists of a channel that is 120 units long and 2 units high. A half channel is modeled by applying symmetric boundary conditions on the bottom boundary. The boundary conditions are completed with velocity-inlet boundary conditions for the left boundary, no-slip boundary conditions for the top boundary, and pressure-outlet boundary conditions for the right one. The size of the first computational cell used for the high-y^+ cases has been optimized for the central point to lie in the logarithmic layer. This allows complications related to the modeling of turbulence in the buffer layer. In the vertical direction meshes consists of a fixed-distance first computational cell with uniform spaced cells at the bulk of the channel. The same computational mesh is used for the low-y^+ modeling of both Reynolds numbers. This mesh has been optimized to provide an appropriate resolution of the boundary layer with the $k-\omega$-SST model.

For the high-y^+ case, both the $k-\epsilon$ and $k-\omega$-SST model are validated. For the low-y^+ case, only wall-resolved $k-\omega$-SST simulations are performed. Steady-state simulations were performed until absolute residuals for each of the solved quantities were less than 10^{-12}.

Case	Axial Length	Nx	Half Height	Ny	Bulk Reynolds	First Cell y^+
Re_τ - High y^+ = 395	120	400	1	36	14,000	$\sim$ 48.5
Re_τ - High y^+ = 590	120	400	1	36	22,500	$\sim$ 46.6
Re_τ - Low y^+ = 395	120	2,000	1	80	14,000	$\sim$ 0.3
Re_τ - Low y^+ = 590	120	2,000	1	80	22,500	$\sim$ 0.5

Table 1. Parameters of the computational meshes for the channel validation studies.

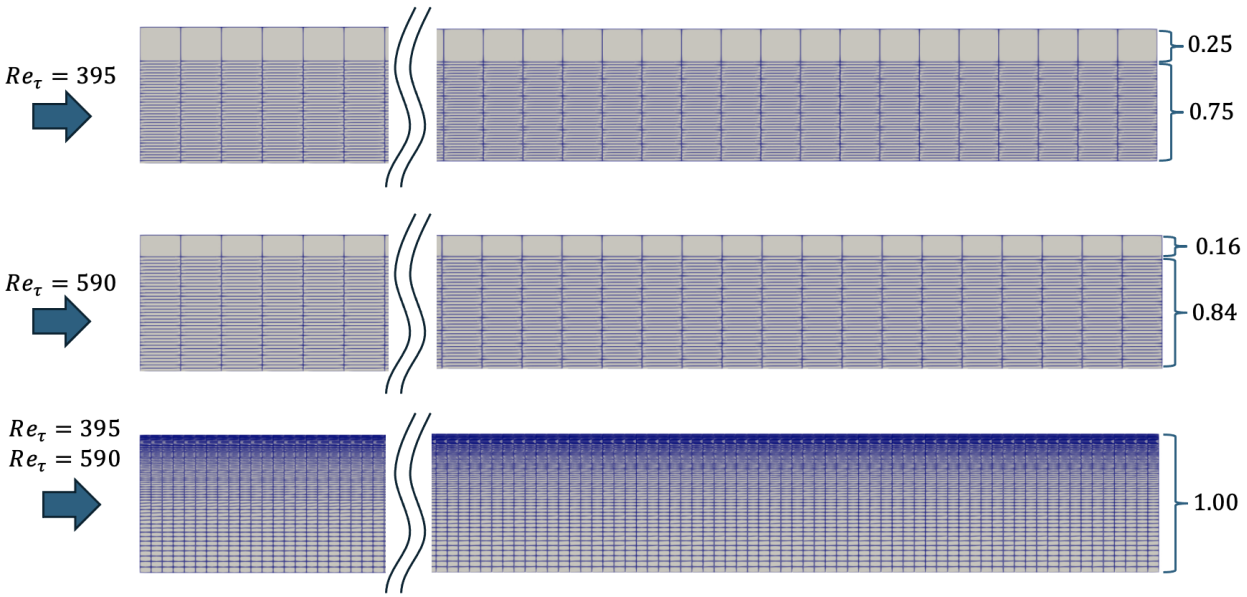

Figure 1. Computational meshes uses for the channel validation studies. Top: computational mesh for $\mathrm{Re}_\tau = 395$ with high y^+. Center: computational mesh for $\mathrm{Re}_\tau = 590$ with high y^+. Bottom: computational mesh used for the low y^+ studies.

For the $\mathrm{Re}_\tau = 395$ case, the velocity profiles at the outlet of the pipe, where the flow is fully developed, are shown in Figure 2. The left panel of this figure shows the comparison of the axal velocity direct numerical simulation with the high-y^+ $k-\epsilon$ and $k-\omega$-SST models and the low-y^+ $k-\omega$-SST model using a linear scale for the vertical distance. The right panel of this figure shows a more detailed comparison between he direct numerical simulation low-y^+ $k-\omega$-SST model using a logarithmic scale for the wall distance. We see a very good agreement with all models and the direct numerical simulation. Moreover, we see that all models are able to resolve the velocity profile near the wall, which is be related to the pressure drop. Additionally, we see that the wall-resolved $k-\omega$-SST model can accurately capture the boundary layer near the wall.

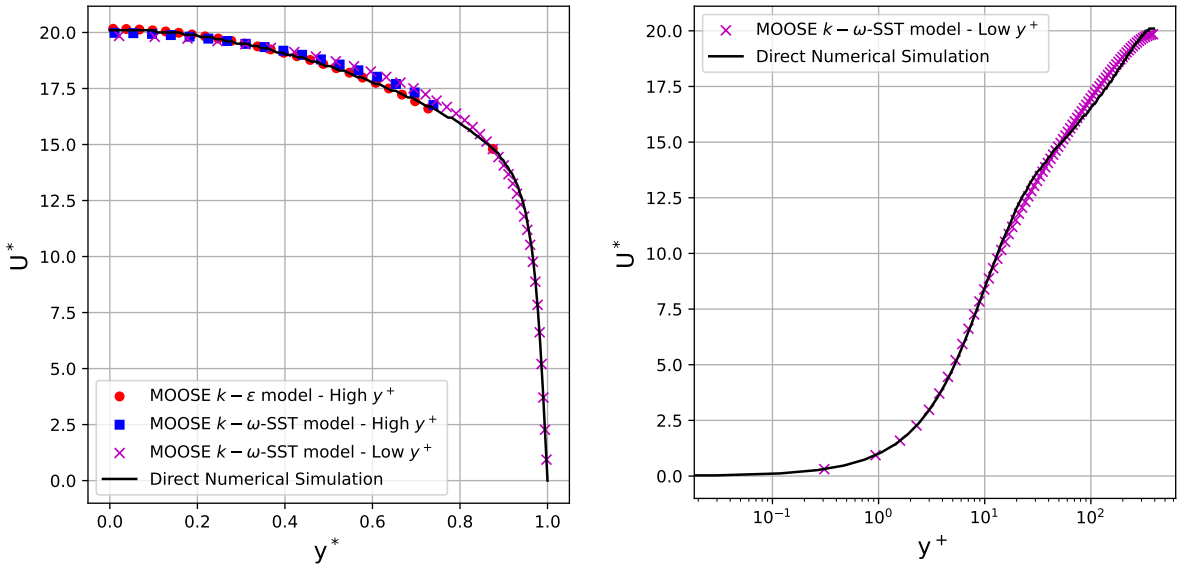

Figure 2. Comparison of the axial velocity profile between the $k-\epsilon$ and $k-\omega$-SST model in MOOSE with high and low y^+ treatment for a turbulent channel against Direct Numerical Simulation [1] for a channel at $Re_\tau = 395$.

The equivalent results for the case with $\mathrm{Re}_\tau = 590$ are presented in Figure 3. Again, a similarly good agreement is obtained for the axial velocity profiles between the RANS turbulence models and the direct numerical simulation. This good agreement is still observed at the bulk and near the wall of the channel.

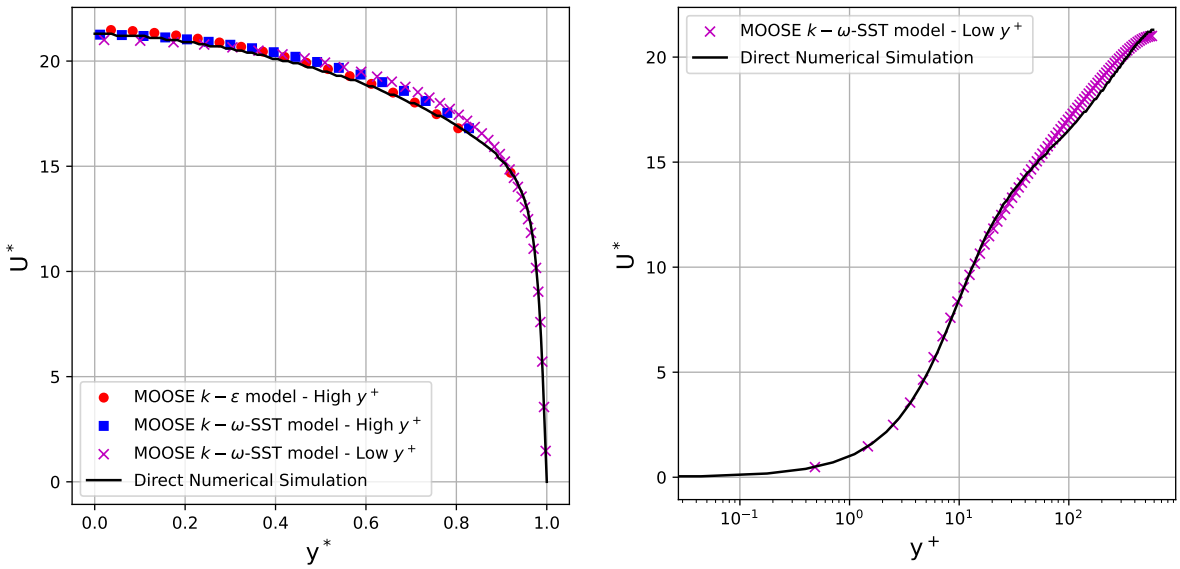

Figure 3. Comparison of the axial velocity profile between the $k-\epsilon$ and $k-\omega$-SST model in MOOSE with high and low y^+ treatment for a turbulent channel against Direct Numerical Simulation [1] for a channel at $Re_\tau = 590$.

The percent L^2-error in the axial velocity profiles in the cases analyzed are detailed in Table 2. In general,

we see a better performance of the $k-\omega$-SST models and, in particular, better results are obtained for the low-y^+ version of this model. Nonetheless, as previously observed graphically, a very good agreement is obtained between all models and the direct numerical simulation data.

Case	**Error k-ϵ [%]**	**Error k-ω-SST with high y^+ [%]**	**Error k-ω-SST with low y^+ [%]**
Re_τ = 395	-1.19	0.32	0.45
Re_τ = 590	-1.55	-1.51	-0.87

Table 2. Comparison of wall shear stress between the Direct Numerical Simulations and each of the models analyzed in this work.

This section has validated the performance of the developed RANS models for a channel. This allows us to use the model with confidence for straight pipes, while knowing that small errors can be expected for the velocity profile and pressure drop. However, this is not fully inclusive of the more complex geometries expected in MSRs. Hence, in the next section, we present the validation of the models for a backward facing step, which tests the attachment and re-attachment of the flow boundary layer.

2.3.2. Backward facing step

The experiment used for this validation case is a backward facing step [2]. The backward-facing step (BFS) flow experiment is a classic benchmark case used for validating CFD models, particularly turbulence modeling. The experiment involves a two-dimensional, incompressible flow over a step, creating a separated flow region characterized by flow recirculation and boundary layer reattachment. The geometry consists of a rectangular channel with a sudden step in the lower wall, inducing a flow separation downstream of the step. Key parameters of the experiment, including the step height (h), the Reynolds number based on the step height, and the inflow velocity profile, are presented in Table 3.

Table 3. Key Parameters of the Backward-Facing Step Flow Experiment

Parameter	**Value**
Step Height (h)	0.0127 m
Reynolds Number (Re_h)	36,000
Inflow Velocity Profile	Fully developed turbulent flow
Channel Height (H)	$8h$
Expansion Ratio	9 : 8
Flow Separation Point	Downstream of the step
Reattachment Length (L_r)	$6.26h$

The geometry and computational mesh used for the validation in the backward facing step is depicted in Figure 4. A surrogate model of a channel is used to determine the fully develop inlet boundary conditions for each turbulent model. No-slip wall boundary conditions are used for the bottom and expansion boundaries, while slip boundary conditions are used for the top one. Outlet-pressure boundary conditions with gauge pressure of $P = 0$ are used at the outlet boundary. The mesh is designed to support high-y^+ wall treatment. At the inlet of the channel, the non-dimensional distance to the wall is $y^+ \sim 59$ and, after the step, it varies from $y^+ \sim 20$ after the expansion to $y^+ \sim 36$ towards the outlet of the channel.

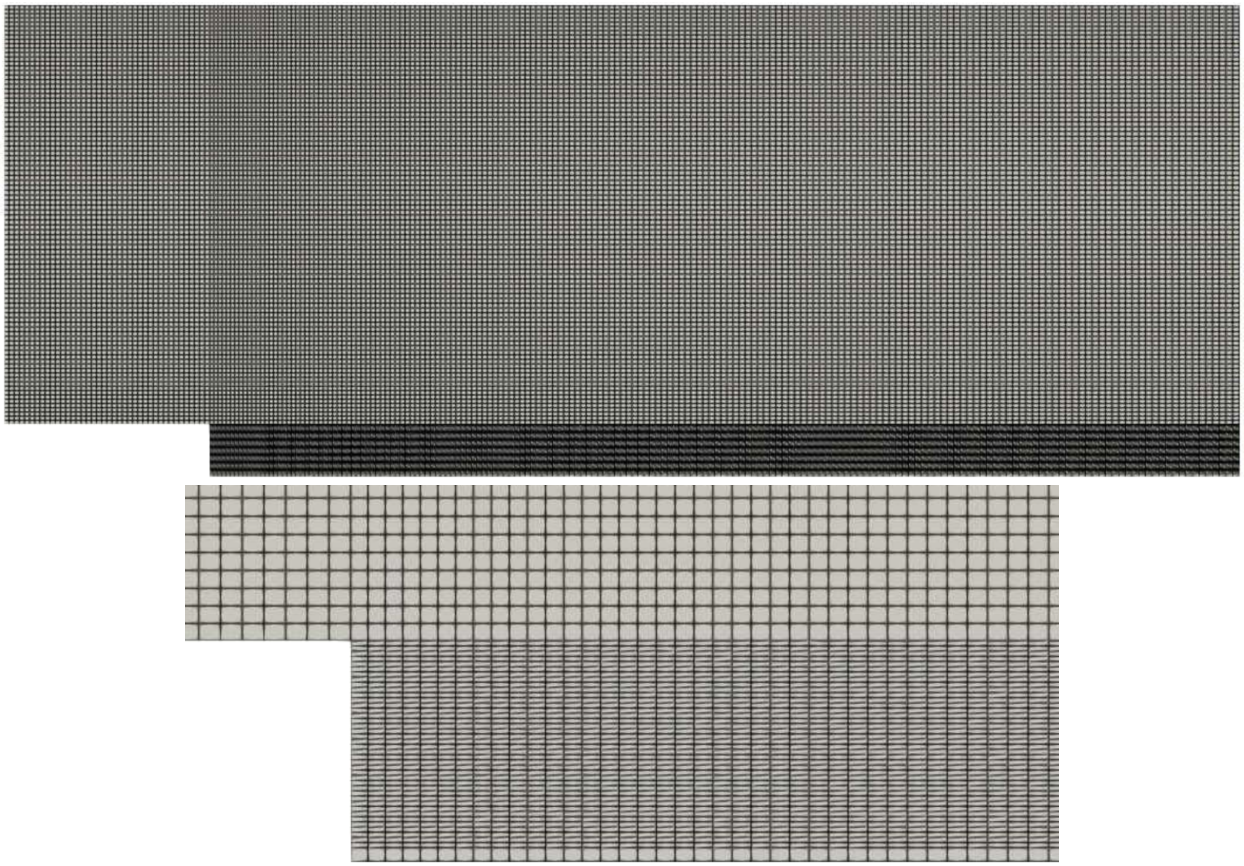

Figure 4. Computational mesh used for the BFS studies. Top: full computational mesh. Bottom: detail of the mesh at the flow expansion point.

The comparison of the results obtained for the pressure and skin friction coefficient next to the bottom wall are shown in Figure 5. The following definitions are adopted for these two coefficients:

$$C_p = \frac{P}{\frac{1}{2}\rho U_{ref}^2} \tag{15}$$

$$C_f = \frac{\tau_w}{\frac{1}{2}\rho U_{ref}^2}, \tag{16}$$

where P is the pressure near the bottom wall, τ_w is the wall shear stress, and U_{ref} is the reference velocity that is taken as the maximum inlet velocity at the entrance of the backward facing step. A good agreement with the experimental results is observed between the models and the experimental measurements in Figure 5. Both models, the $k-\epsilon$ and $k-\omega$-SST, are able to predict the shape of the pressure drop and recovery produced due to the detachment and re-attachment of the boundary layer. Additionally, for the pressure coefficients, the prediction of both models is approximately equivalents. For the skin friction coefficient, the $k-\omega$-SST model, is able to better predict the accumulation of turbulent kinetic energy before the detachment of the boundary layer, which leads to a better prediction of the wall shear stress. Downstream the detachment, the $k-\epsilon$ model can better predict the pressure recovery during the development of the downstream boundary layer. This is mainly due to the limiters in the $k-\omega$-SST model, which under-predict the buildup of turbulence viscosity

at the re-attachment region. While the epxeriment predicts a re-attachment length of $r = 6.26h \pm 0.1h$, the re-attachement length of the $k-\epsilon$ model is $r = 4.92h$ and the one of the $k-\omega$-SST model is $r = 5.60h$. This better performance of the $k-\omega$-SST model is expected due to the limiters implemented in the model for improving boundary layer detachment and re-attachment. However, within the modeling limitations, a good performance is observed for both models when comparing against the experimental measurements.

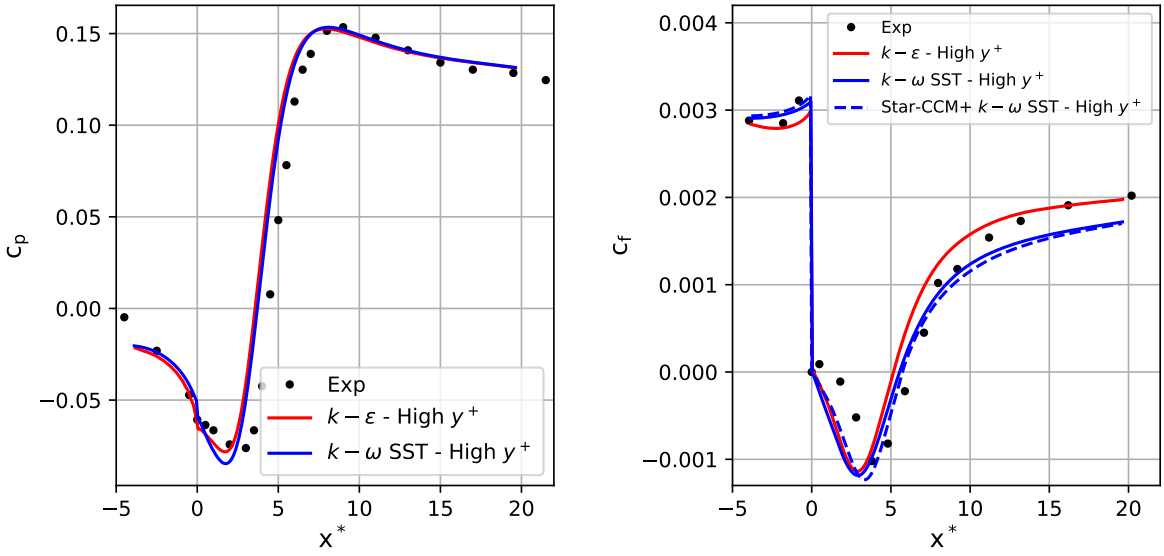

Figure 5. Comparison of the pressure and friction coefficients of the $k-\epsilon$ and $k-\omega$-SST model in MOOSE with high y^+ treatment for a backward facing step against experiments [2].

The comparisons for the vertical velocity profiles for selected axial locations are presented in Figure 6. The coordinate $x* = 0h$ corresponds to the step expansion, while the y^* coordinate goes in the vertical direction from the bottom wall upwards. Both models, the $k-\epsilon$ and $k-\omega$-SST models are able to predict the recirculation at the bottom of the step after the expansion with good accuracy. Additionally, both models are able to predict the profiles after the boundary layer re-attachment near the wall and at the bulk of the flow. This comparison confirms the previous observation of the good performance of the model observed for the pressure and skin friction coefficients.

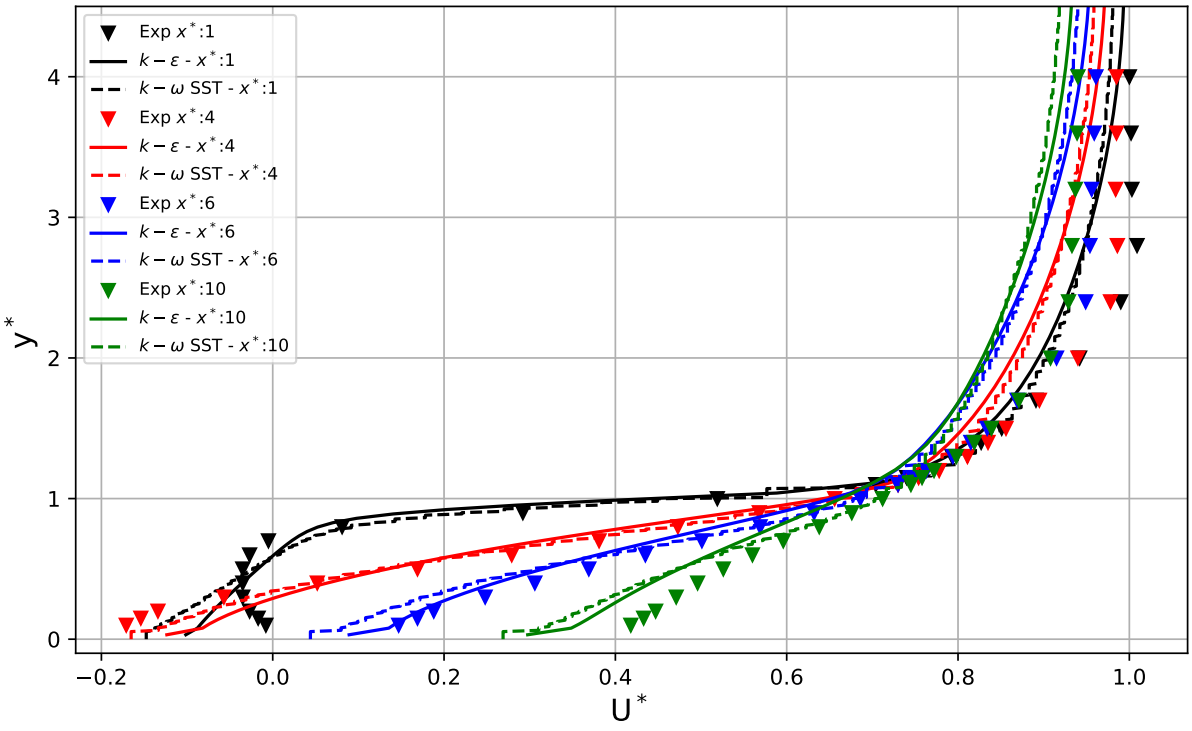

Figure 6. Comparison of vertical profiles of the horizontal velocity of $k-\epsilon$ and $k-\omega$-SST model in MOOSE with high y^+ treatment for a backward facing step against experiments [2]

2.3.3. Swirling flow in curved pipe

The experiment used in this validation section is the internal turbulent flow in a swirling pipe [3]. This experiment tests the turbulence models ability to capture the near wall behavior in both recirculation and flow impingement zones. In addition, this experiment tests the accuracy during the recovery zone of the flow after the pipe's bend curvature. A sketch of the experimental configuration is shown in Figure 7. Table 4 presents the geometrical dimensions and the experimental conditions.

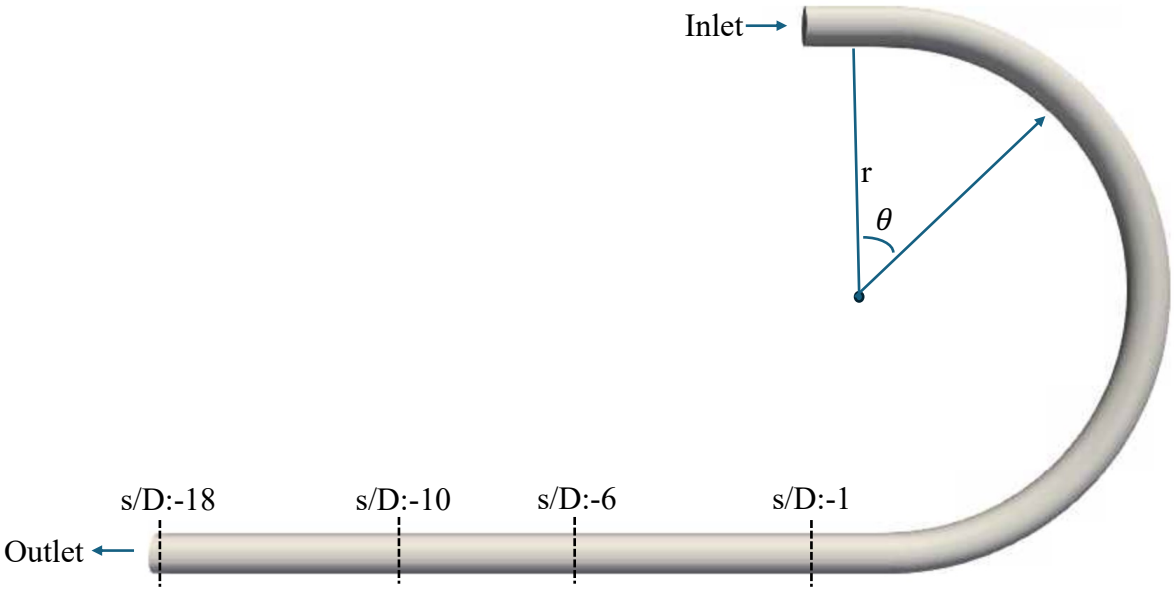

Figure 7. Configuration of the Swirling Pipe Flow Experiment.

Table 4. Key Parameters of the Swirling Pipe Flow Experiment

Parameter	**Value**
Diameter (D)	0.0762 m
Curvature radius (r)	0.457 m
Bulk Velocity	10.4 m/s
Reynolds number (Re)	50000

The computational mesh used in this exercise is exhibited in Figure 8. The outlet velocity profile is used as the convergence metric for several mesh refinements. In these meshes the first wall cell is kept at a y^+ above 30 to ensure that the high y^+ velocity wall functions remain in the logarithmic boundary layer. The final converged mesh is shown in Figure 8, with 520K total elements and a wall aspect ratio of 10.

A fully developed flow condition is imposed at the inlet of the domain and the pressure is fixed at the outlet of the bent pipe. At the wall, no-slip conditions for velocity are set and we implement non-equilibrium wall functions due to the presence of stagnation and recirculation zones expected in the flow.

Figure 8. Computational domain of the swirling pipe model. The figure shows the inlet of the domain and half of the pipe's bent extension.

The comparison of the results of the validation case against experiments for the $k-\epsilon$ and $k-\omega$ SST models are presented in Figure 9. The plots compare the dimensionless velocity profile parallel to the pipe's axis along a vertical plane as it is depicted in Figure 7. The velocity and the radial coordinate is non-dimensionalized using the bulk velocity value and the pipe's radius, respectively. The first four plots correspond to velocity profile at different locations after the bent pipe. The location of these profiles are specified in Figure 7, and correspond to 1,6,10 and 18 diameters from the end of the bent towards the horizontal return pipe outlet. Furthermore, the last four plots show the axial velocities at different θ theta angles along the bend, where the angle theta is defined in Figure 7.

Both RANS models provide similar predictions for the axial velocity profiles along the pipe's vertical plane. Throughout the recovery zone between s/D:-1 until s/D:-18, the models successfully follow the behavior of the flow and its recovery towards a fully developed flow. The presence of a stagnation zone can be observed after the bent, between r^* 0 and 1. The use of non-equilibrium wall functions, where the velocity scale is computed using the turbulent kinetic energy is an important consideration to provide good accuracy and not overpredict the turbulent viscosity in stagnation zones. The use of equilibrium wall functions, where the velocity scale is proportional to the square root of the wall shear stress leads to overprediction of turbulent viscosity. In addition, the use of Durbin's turbulent kinetic energy production limiter prevents the overproduction of turbulent kinetic energy in this stagnation zone. Along the bent pipe region, both models are able to perform well in the impingement region of the flow (values of r^* between -1 and 0) and in the dettachment region (values of r^* between 0 and 1).

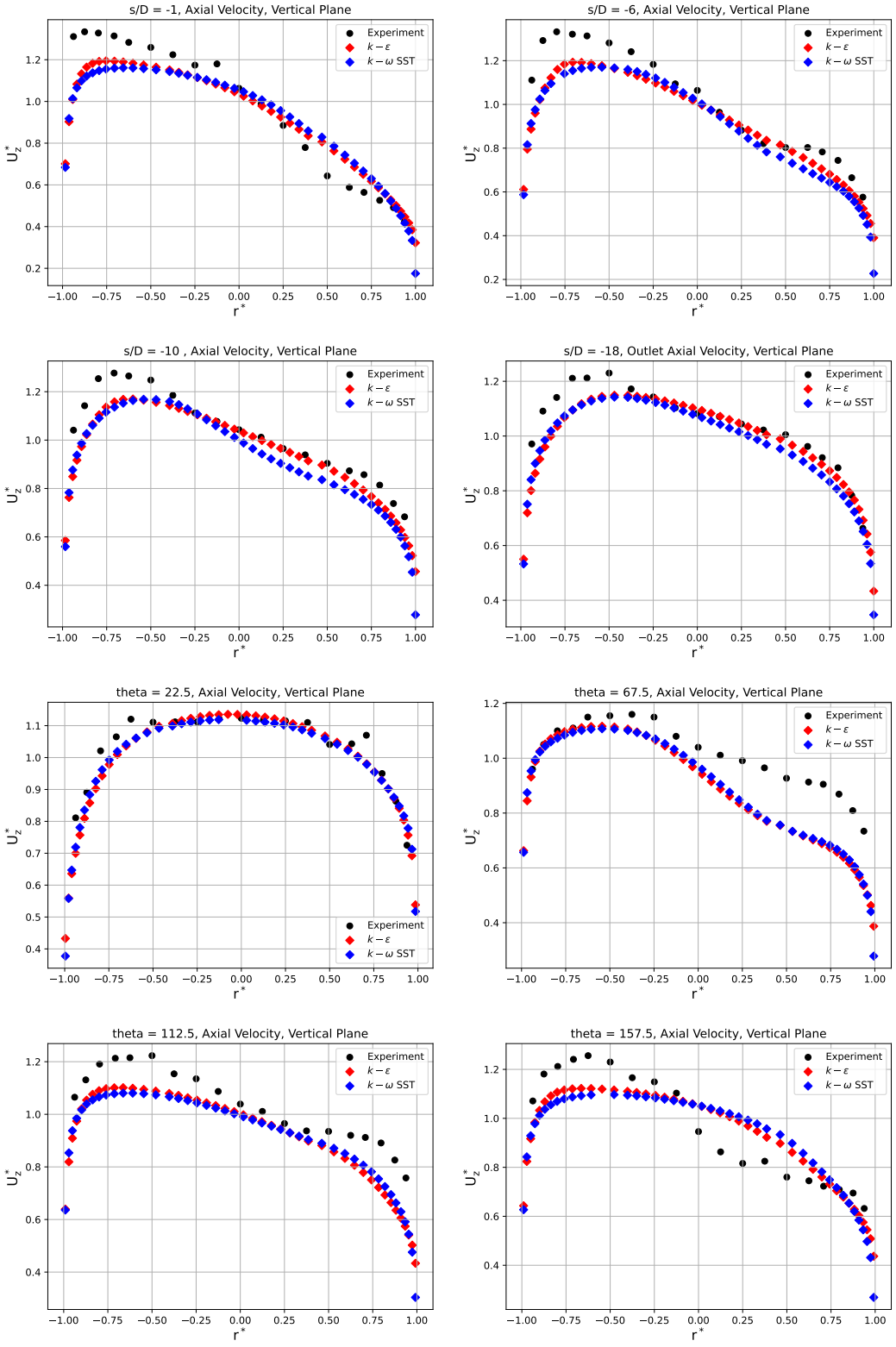

Figure 9. Axial Velocity profiles of MOOSE $k-\epsilon$ and $k-\omega$ SST at different locations of the swirled pipe compared to the experimental data of Anwer et al.[3].

Both models, the $k-\epsilon$ and $k-\omega$-SST models are able to predict an accurate dettachment and impingement of the flow in the bent region and the flow recovery towards fully developed conditions after the bent.

This comparison confirms the previous observations of the good performance of the model observed for the pressure and skin friction coefficients and highlights the importance of using non-equilibrium wall functions along with turbulent kinetic energy production limiters in RANS two-equation models $k-\epsilon$ and $k-\omega$ SST.

2.4. Model benchmark for Molten Chloride Reactor Experiment

2.4.1. Reactor geometry and operating conditions

The proposed conceptual model is inspired by the open source specifications of the Molten Chloride Reactor Experiment (MCRE) provided by TerraPower [17] and is illustrated in Figure 10. We will refer to this reactor as the L-MCR. The dimensions shown for the reactor in this figure are in meters. This is a fast spectrum reactor whose main features are a core cavity with no internal elements, a pump, and the connecting piping between the reactor and the pump. The main core cavity is surrounded by a neutron reflector. The liquid nuclear fuel flows from the bottom piping into the reactor cavity and into the pump. Then, driven by the pump, the liquid fuel circulates in the return pipe back to the reactor cavity. Control rods are not explicitly included in the model, and the power distribution is computed by solving an eigenvalue problem.

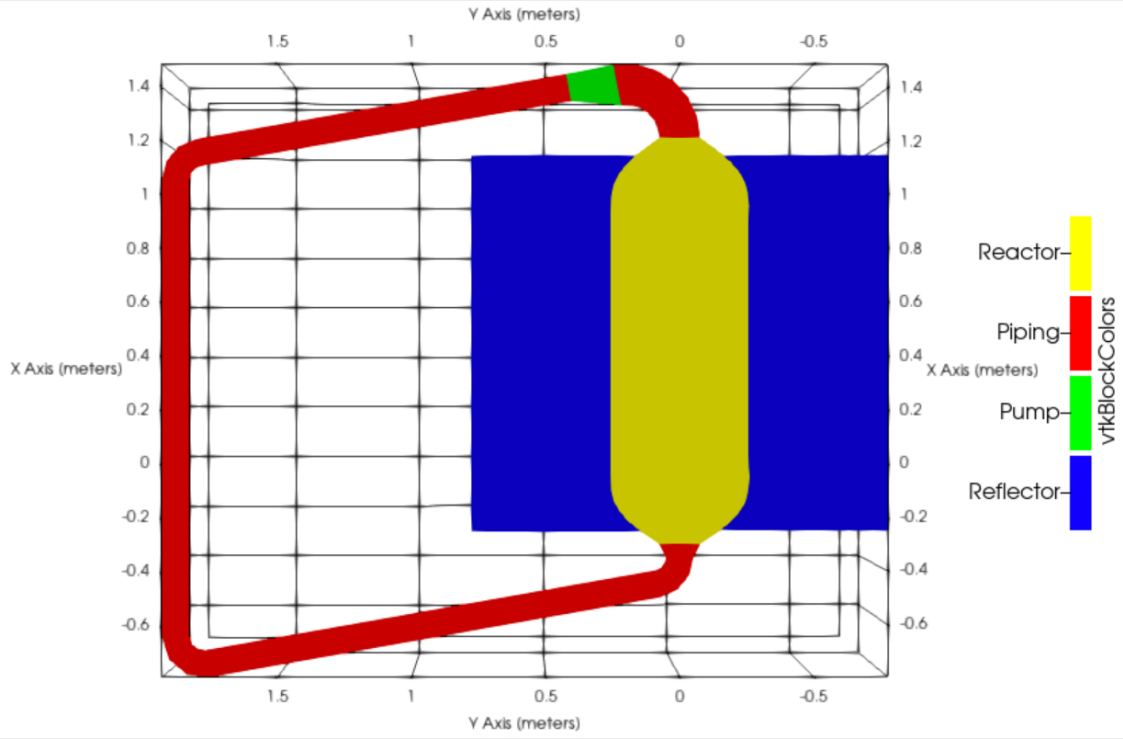

Figure 10. Schematic design of the Lotus Molten Chloride Reactor.

The key design parameters of the reactor are outlined in Table 5. The fuel salt composition is based on the eutectic point of the UCl_3-NaCl system. The thermophysical properties for the nuclear salt and the reflector are based on best-estimate open literature values [18–22]. The model developed assumes that the reactor has a power of 1 MW_{th} and a rated mass flow rate of 25 kg/s.

Table 5. Specifications of LOTUS Molten Chloride Reactor.

Parameter	Value
Core Power [MW_{th}]	1.0
Operation Temperature [K]	900
Rated Mass Flow Rate [kg/s]	25
Fuel Salt [mol %]	UCl_3 [33.3%] - NaCl [66.7%]
Fuel Enrichment ^{235}U [wt %]	93.2
Fuel Salt Density [kg/m^3]	$4212.6 - 1.0686T$
Fuel Salt Specific Heat [$\frac{J}{kg.K}$]	8900.439 - 13.77936 T
Fuel Salt Thermal Conductivity [$\frac{W}{m.K}$]	$5.6820 - 8.7832 \times 10^{-3}T$
Fuel Salt Dynamic Viscosity [$Pa.s$]	$1.505 \times 10^{-4} e^{\frac{2.666 \times 10^4}{8.314T}}$

2.4.2. Description of the Large Eddy Simulation

Large Eddy Simulations have been performed for obtaining a reference solution for the L-MCR against which to compare the RANS models developed. The LES simulations were performed using the STAR-CCM+ v2021.1 commercial software [23]. Two different subgrid-scale models are tested to test model independence to turbulence model. On the one hand, a wall-adapting local eddy-viscosity (WALE) model, which is designed for accurately capturing local strain rate near walls. On the other hand, a dynamic Smogorisnky-Lilly model (DSM), which provides a better resolution of turbulent production and dissipation in all regions via dynamically adapting the turbulent closure coefficients to the flow field characteristics.

The mesh used for the LES studies of the L-MCR has $\sim$15.72M computational cells. A detail of this mesh at the entrance of the reactor core is depicted in Figure 11. The average y^+ in the mesh is 0.2, while the maximum one is 3.1. The appropriateness of the mesh developed for LES simulations is quantified via the M-resolution criterion, which computes the ratio of modeled (k_{sgs}) against total, i.e.., resolved (k_{res}) and modeled, turbulent kinetic energy. For the WALE and the DSM models, this criterion reads as follows:

$$M^{WALE} = \frac{k_{sgs}^{WALE}}{k_{sgs}^{WALE} + k_{res}} = 3.6 \pm 1.2\% \tag{17}$$

$$M^{DSM} = \frac{k_{sgs}^{DSM}}{k_{sgs}^{DSM} + k_{res}} = 3.5 \pm 1.4\% \,. \tag{18}$$

In both cases most of the turbulent kinetic is resolved by the mesh, while less than 5% of the turbulent kinetic energy is actually modeled by the sub-grid scale model. This is above of the usual recommendation for of having $M < 10\%$ for the LES models.

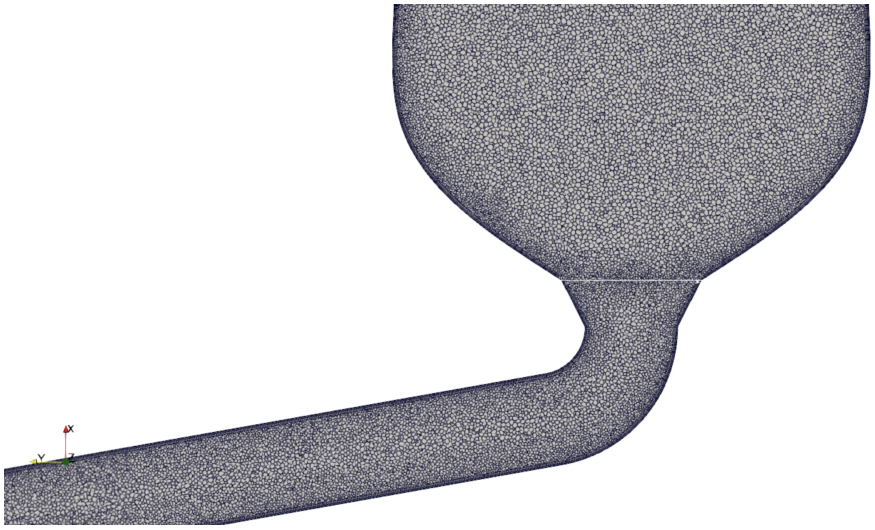

Figure 11. Detail of the LES mesh used at the L-MCR reactor inlet.

Snapshots of the instantaneous velocity and temperatures predicted by the WALE LES model are shown in Figure 12. As the flow enters the reactor core, it deflects towards the right of the core cavity due to the centrifugal acceleration produced by the curvature of the inlet pipe. Note that this effect is produced because no mixing plate is present at the inlet of the reactor core. Then, the flow rises by the right side of the core cavity. During this process, a significant amount of turbulent kinetic energy is produced by the flow injection into the core cavity. This results in a highly turbulent field in the reactor core, where eddies are transported towards the outlet of the core. Additionally, a recirculation is produced inside the reactor core due flow constriction in the outlet pipe. This recirculation results in the heating of the central part of the core cavity. The instantaneous velocity field showcases the complications of RANS modeling capturing the thermal hydraulics phenomena expected for the L-MCR reactor studied.

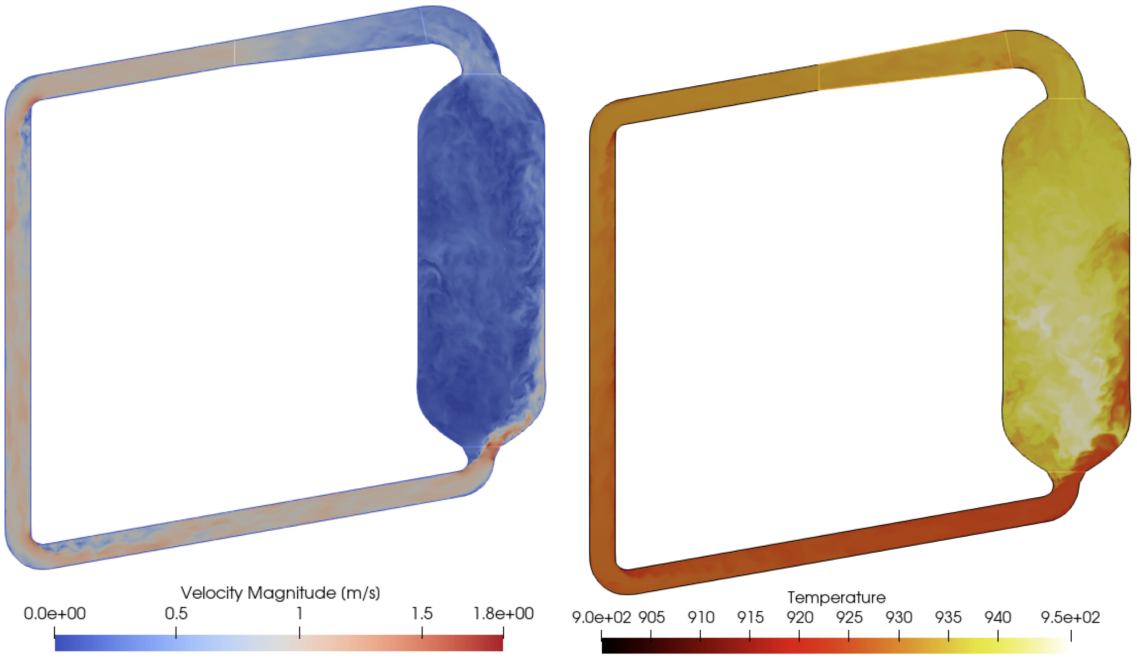

Figure 12. Illustration of instantaneous velocity (left) and temperature (right) by the WALE LES model.

LES simulations are started from a converged RANS simulation using the $k-\omega$-SST model. Then, the LES simulations are run for $\sim$ 100s, around 20 flow through, until turbulence develops in the reactor core. Then, the results of the LES simulations are time-averaged for 450s, for over 100 flow through, until convergence of the first-order statistics is obtained. Then, the results of the WALE and DSM models are then compared. This comparison is graphically presented for contour plots of an axial mid-section of the core in Figure 13 for the vertical and horizontal velocities and for the pressure. Visual inspection shows similar fields for the time-averaged velocity and pressure.

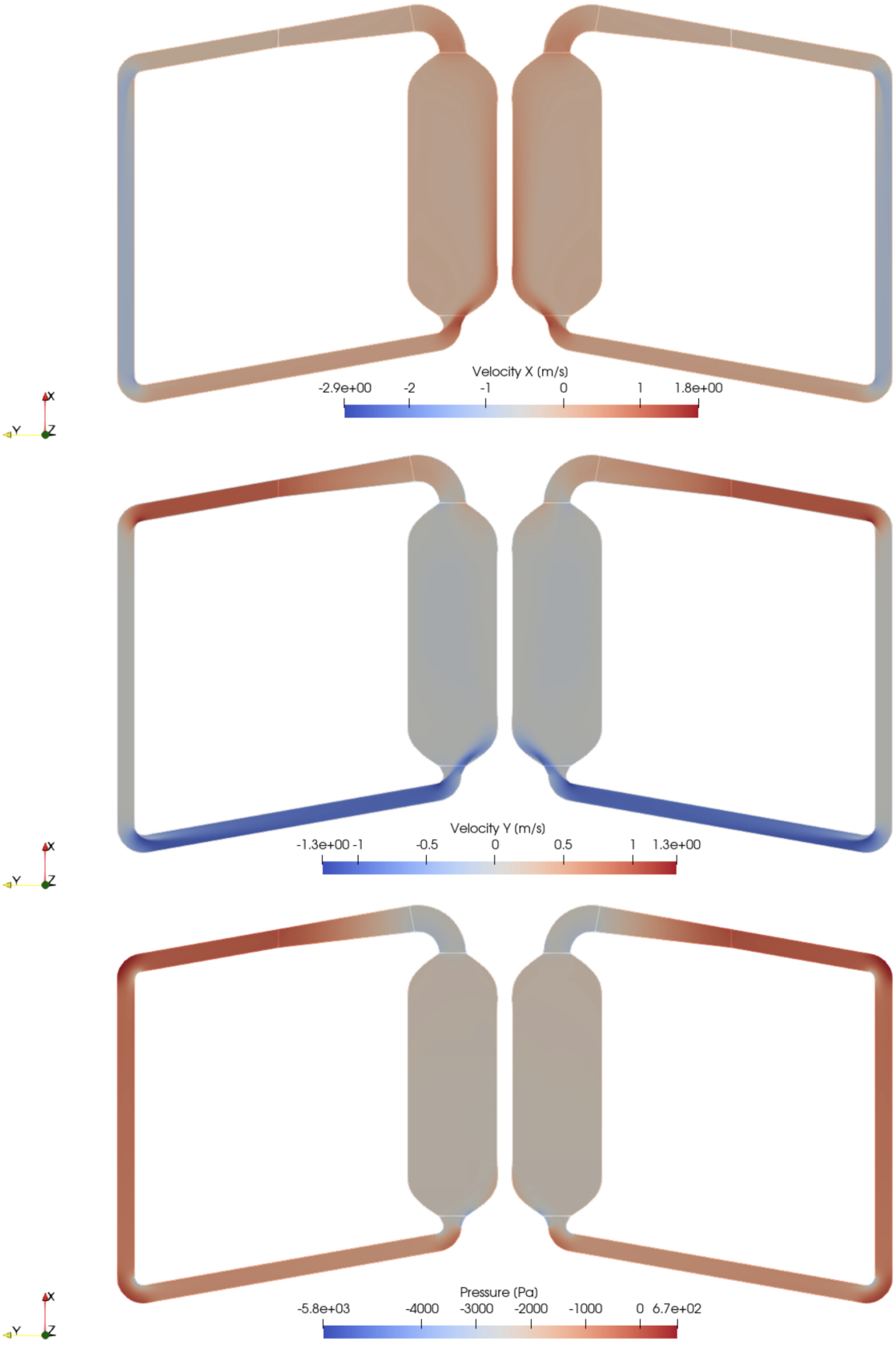

Figure 13. Comparison of the velocity field in the x-direction (top), y-direction (center), and pressure (bottom) for the WALE (left) and dynamic Smagorinsky (right) subgrid scale models.

The axial velocity across the central line of the reactor core for WALE and DSM in Figure 14. Qualitative, a good agreement is observed between both solutions. In fact, the L^2 difference between the WALE and DSM solutions are 0.22% and 0.31% for the axial and horizontal velocity and 0.06% for the pressure field.

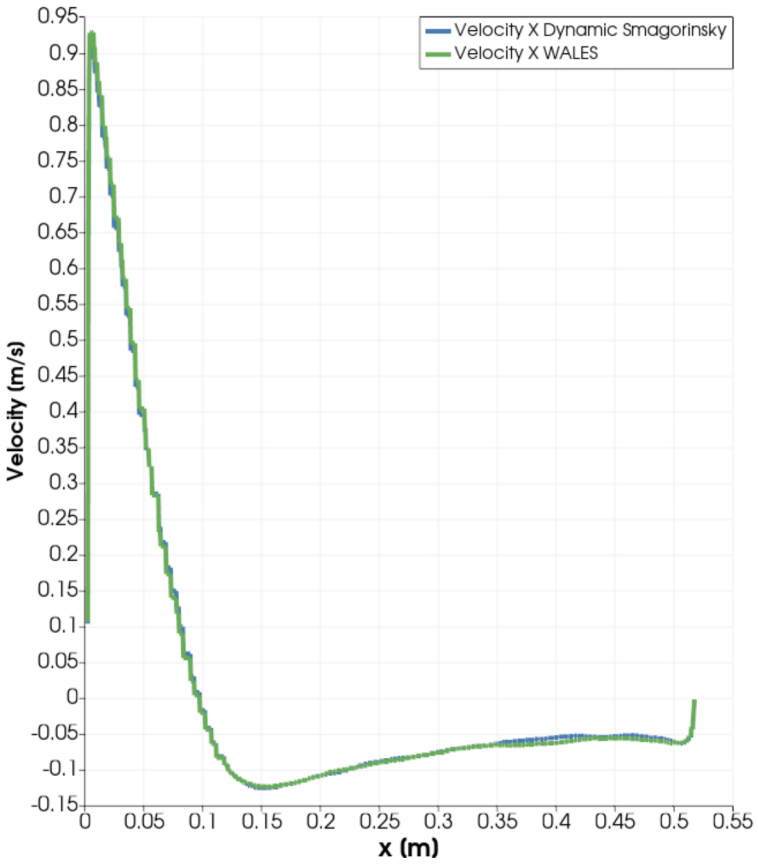

Figure 14. Comparison of the axial velocity fields between the WALE and dynamic Smagorinsky subgrid scale models for a horizontal centerline in the reactor core.

Due to the good agreement between the two sub-grid scale models, one concludes that the comparison with any of these models against RANS would be similar. Hence, the WALE model is used for comparison in the next section.

2.4.3. Description of the Reynolds Average Navier Stokes models

The two-equation RANS models $k-\epsilon$ and $k-\omega$ SST, implemented in MOOSE Finite Volume module and validated in Section 2.3., are employed to obtain the flow behavior under nominal operation conditions. The steady-state flow behavior is then compared against LES simulations, which were described in Section **??**.

A constant volumetric momentum source is added to the pump region of the reactor model to impose a 25kg/s mass flow. No-slip boundary conditions are set on the reactor smooth walls to impose a zero-velocity value. Non-equilibrium turbulent wall functions, or high y^+ wall functions, are imposed at the walls to impose the value of the turbulent viscosity value at the wall faces and allow the code to correctly compute the wall shear stress at the wall. Due to the lack of open boundary conditions where the pressure is imposed, the value of the pressure is pinned at the center of the reactor to a value of 0 Pa.

The Rhie-Chow interpolation is used to compute the velocity values at the faces using the pressure gradient, and in doing so avoid checkerboarding.

A grid convergence study is performed to define the computational domain used for this study. The mesh is composed by hexahedron elements, and produced using the Cubit meshing software. We construct meshing boundary layers, i.e. higher refinement in the near wall region, such that the size of the first cell exceeds the y^+ value of 30 and ensure that the flow is in the logarithmic region for every mesh tested. The reason why we do not fully resolve the velocity boundary layers throughout the reactor is to avoid having a large amount of elements and avoid incurring in a high computational cost when running potential long transients.

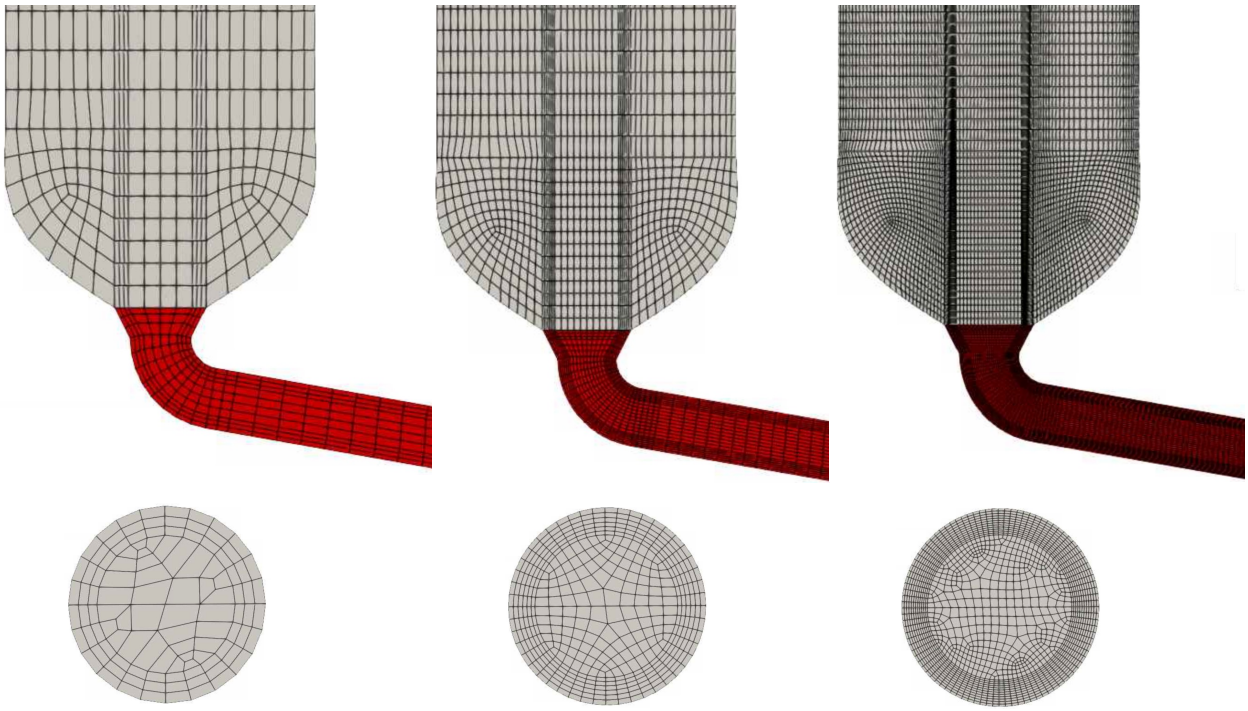

Figure 15. The three successively refined meshes tested in the grid convergence study.

We test three successively refined meshes, which are exhibited in Figure 15. The refinement ratio between two successive meshes is set to two. The pressure drop of the whole system is used as the grid convergence metric for the tested meshes and the values for both RANS models are reported in Table **??**.

	Number of elements	Pressure Drop [Pa]	
		$k-\epsilon$	$k-\omega$ SST
Coarse	∼26K	3850	3950
Medium	∼208K	3050	3100
Fine	∼1664K	2815	2840

The GCI (Grid Convergence index) technique employed by Roache [**?**] is applied to evaluate the spatial grid convergence. The order of convergence p can be obtained from the slope of the curve of the error in pressure drop as a function of the refinement ratio. The order of convergence is computed as follows:

$$p = ln\left(\frac{\Delta p_c - \Delta p_m}{\Delta p_m - \Delta p_f}\right)/ln(2), \tag{19}$$

where Δp_c, Δp_m and Δp_f are the pressure drops corresponding to the coarse, medium and fine meshes, respectively. The order of convergence of the $k-\epsilon$ and $k-\omega$ SST is 1.767 and 1.748, respectively. Applying the Richardson extrapolation technique between the medium and fine mesh, while ensuring that the grids are in the asymptotic range of convergence, we can obtain the expected grid error we incur in using the following equation

$$GCI_{\Delta p_f} = 1.25|\frac{(\Delta p_f - \Delta p_m)}{\Delta p_f}|/(2^p - 1)100\%. \tag{20}$$

The resulting error is around 4.8% for both RANS turbulence models.

2.4.4. Comparison of LES and RANS models: Fluid Dynamics

The total reactor pressure drop predictions for a 25 kg/s mass flow from both RANS models implemented in the MOOSE Finite Volume module are compared with those from the LES model, as shown in Table 6. The pressure drop predictions of both RANS models is within the expected accuracy with respect to the values of the LES model.

Table 6. Comparison between the total reactor pressure drop predictions between the RANS models and the LES model.

	LES	$k-\epsilon$	$k-\omega$ SST
Pressure Drop [Pa]	2780	2815 ± 135	2840 ± 136

Next, we evaluate the performance of the $k-\epsilon$ and $k-\omega$ SST models on the flow velocity distribution accuracy when compared to higher fidelity models such as the WALE-LES model. Capturing the flow behavior in the reactor region of liquid fuels, such as the molten salt in this study, is crucial because it directly affects precursor distribution and reactivity, reactor cooling, and corrosion behavior, among other factors. The distribution of flow circulation streamlines is shown in Figure 16. The $k-\omega$ SST model predictions are shown on the left, and the LES model predictions are shown on the right. The $k-\epsilon$ predictions are not shown as the results are similar to those of the $k-\omega$ SST. Figure 16 provides key details of the predictions from the two different models with varying fidelities. The RANS models, on the left of Figure 16, predict a single recirculation pattern in the reactor region, where flow ascends through the right wall and descends through the left wall. In contrast, the LES model predicts two recirculation patterns. The first recirculation pattern involves flow ascending along the left wall, spreading across the front and back walls, and then turning from the top-right region toward the lower-left region, passing through the center of the reactor. The second recirculation pattern is located in the lower-right region of the reactor. Flow rises through the right wall (opposite to the direction of the first recirculation pattern) and then shifts direction from the middle-right region toward the lower-left region of the reactor.

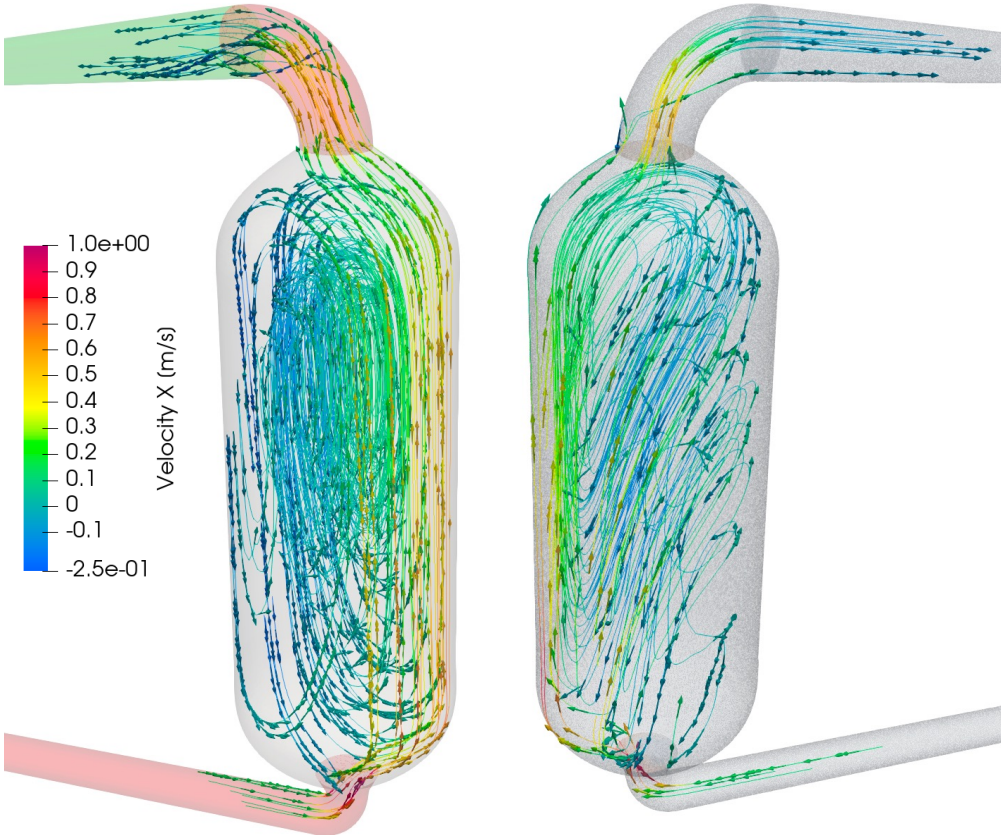

Figure 16. Velocity streamlines at the reactor core region, colored with the vertical velocity magnitude, obtained with RANS models (left) and the LES model (right).

Figure 17 shows the vertical velocities in a slice through the center of the reactor. Figure 18 presents vertical velocities in slices taken at three different vertical locations within the reactor core. Additionally, Figure 19 displays line plots of vertical velocities across the radius of the reactor at these three vertical locations.

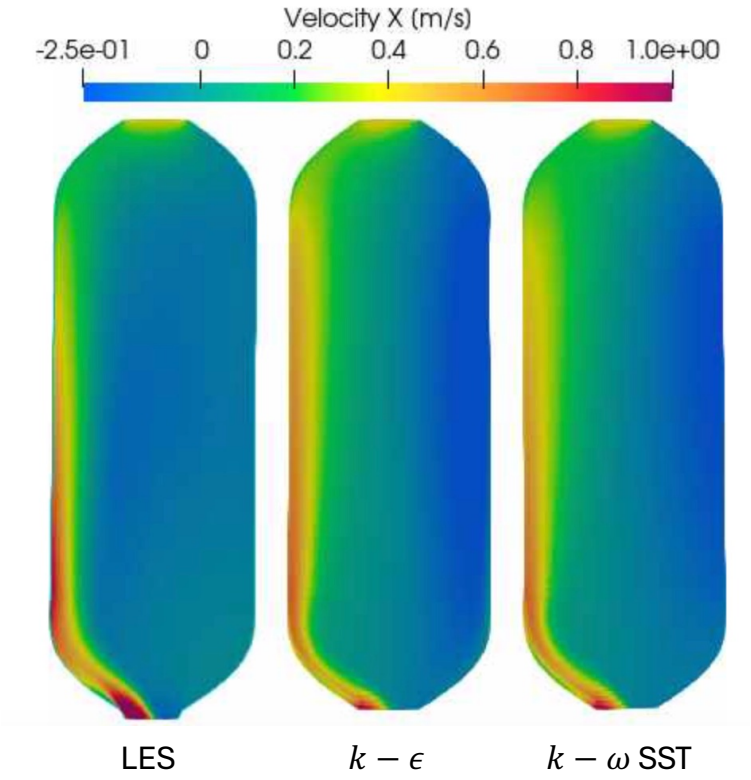

Figure 17. Vertical velocity contours for the LES model and the MOOSE RANS models at a vertical slice through the center of the core.

The flow enters the core in a left-upward direction, impacts the left wall, and then ascends toward the top. The results indicate good agreement between the general predictions of the $k-\epsilon$ and $k-\omega$ SST models and the LES model in the left region of the core, where the salt ascends toward the top. At the center of the core, RANS models predict a higher vertical velocity than LES. This is caused by the misprediction of the first flow recirculation pattern obtained by LES, which is described in detail in Figure 16. Furthermore, RANS overpredicts the negative vertical velocity at the right wall because it only captures a single recirculation pattern. This model does not account for the two competing recirculation vortices observed in the LES. In the LES, the second pattern generates a higher pressure force that slows the downward flow from the first recirculation pattern. Overall, the results from the two RANS models are similar, with no clear advantage of one model over the other.

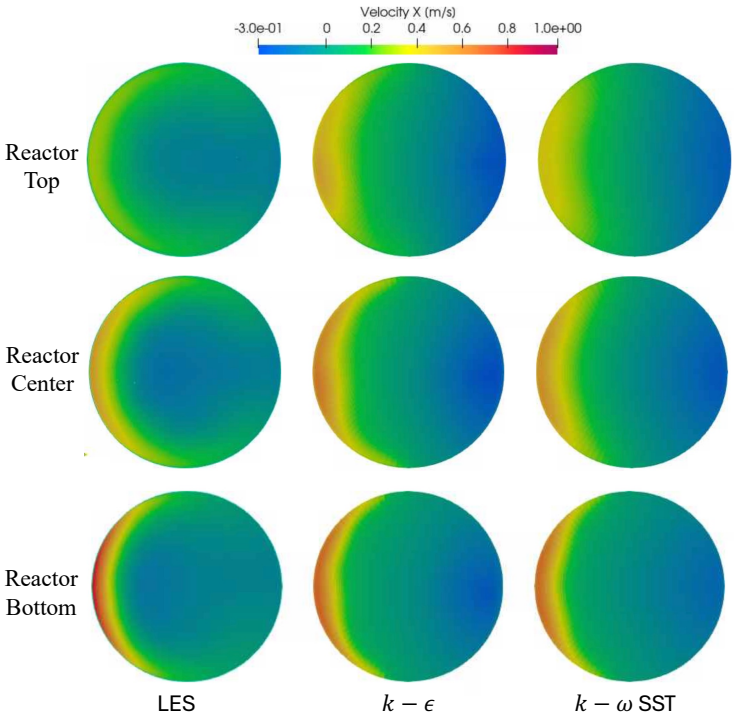

Figure 18. Vertical velocity contours at the bottom, center and top of the reactor core region obtained with $k-\epsilon$, $k-\omega$ SST and LES models.

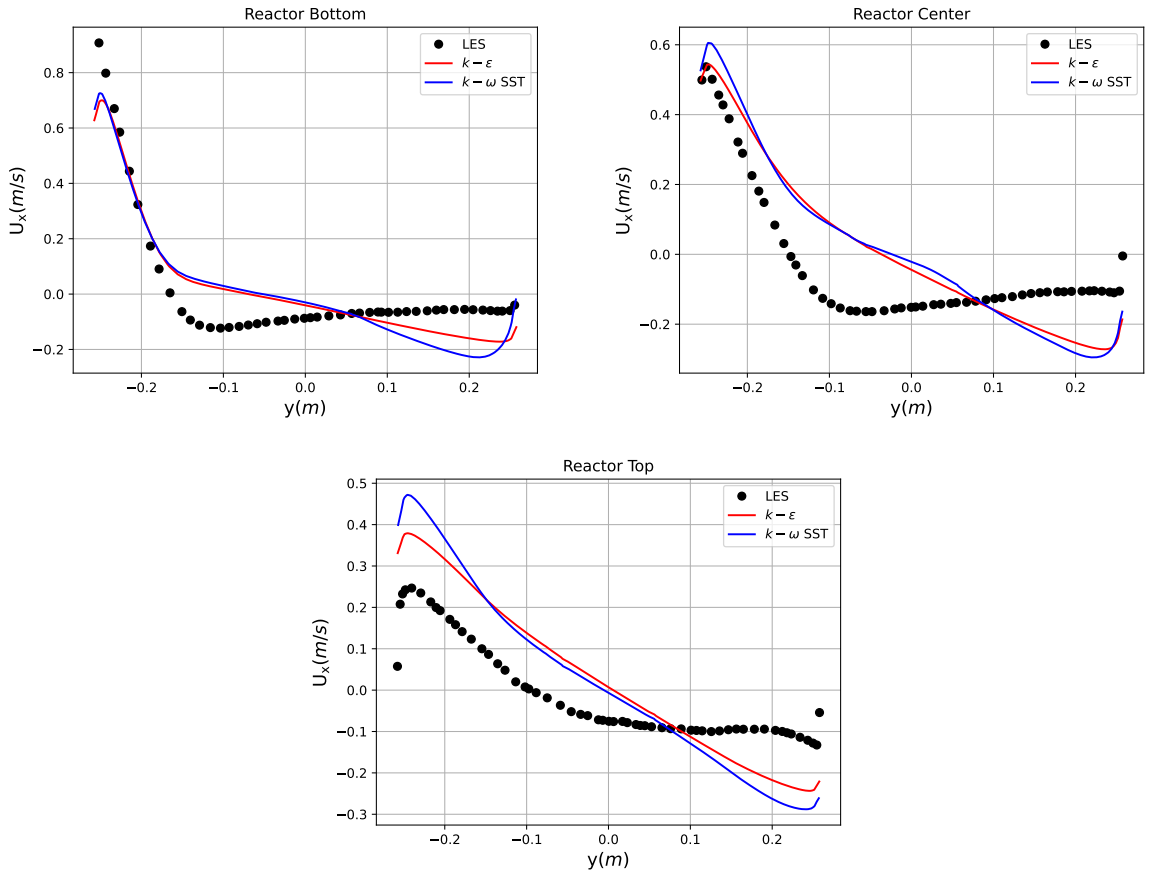

Figure 19. Vertical velocity plots at the bottom, center and top region of the reactor core obtained with $k-\epsilon$, $k-\omega$ SST and LES models.

2.4.5. Comparison of LES and RANS models: Thermal-Hydraulics

In this section we contrast the predictions in temperature fields at steady state in the reactor system between the RANS $k-\epsilon$ and $k-\omega$ SST models in MOOSE and the WALE-LES model. The main goal of this section is to assess the impact of the difference in flow predictions observed in Section **??** between the high-fidelity LES and the two-equation RANS models on the temperature field in the molten salt reactor.

The rated thermal power is set to 100 kW and its distribution is computed by solving a k-eigenvalue problem. Constant thermophysical properties of the salt at the operating reactor temperature are considered. A mass flow of 25 kg/s is imposed. For the LES and RANS models, the turbulent thermal diffusivity is considered proportional to the turbulent momentum diffusivity via a turbulent Prandtl number of 0.9. The walls of the reactor and piping systems are set to 900K. To adequately compute the heat flux at the first cell near the wall at high y^+ values, we employ the Jayatilleke temperature wall functions described in Eq. (**??**).

Figure 20 presents the predicted operational temperature contours at a vertical slice through the reactor core region for MOOSE $k-\epsilon$, MOOSE $k-\omega$ SST and WALE-LES. The three models predict a similar temperature distribution in the core. The colder salt enters through the lower inlet pipe and rises along the left wall. The lower middle region of the reactor has the highest temperature due to maximum power distribution there combined with the flow recirculation zone. On the right side of the reactor, where power is lower, there

is a medium-temperature region with flow recirculating from the top to the bottom along the cooled wall. The average core temperatures are presented in Table 7. A good agreement is observed in the steady state temperature of the molten salt reactor at the core region.

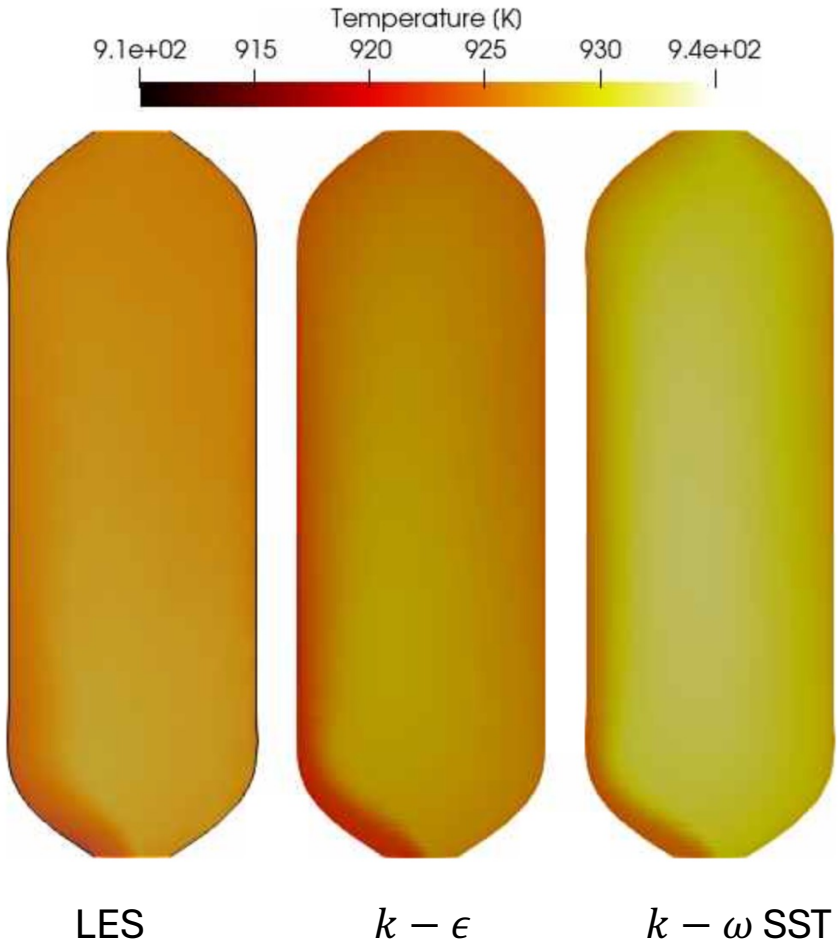

Figure 20. Temperature contours for the LES model and the MOOSE RANS models at a vertical slice through the center of the core.

Table 7. Comparison between the average reactor temperature predictions between the RANS models and the LES model.

	LES	$k-\epsilon$	$k-\omega$ SST
Temperature [K]	925	927	930

2.5. Recommendations for RANS turbulence modeling of pool-type MSRs

The application of RANS turbulence models in the thermal-hydraulic analysis of pool-type MSRs requires careful consideration of model selection, validation, and integration with other physical domains. Given the unique challenges posed by the liquid-fueled configuration of MSRs, particularly in fast-spectrum designs

with open-core geometries, it is imperative that the selected RANS models can accurately capture the complex flow phenomena inherent in these systems.

One of the most significant recommendations from this study is the adoption of the $k-\omega$ Shear Stress Transport (SST) model for MSR simulations. This model's ability to accurately predict boundary layer behavior, particularly in regions with adverse pressure gradients, makes it an ideal choice for the complex geometries and flow conditions encountered in MSRs. The $k-\omega$ SST model's blending function, which transitions smoothly between the $k-\epsilon$ model in the free shear flow regions and the $k-\omega$ model near walls, ensures that the model can handle the diverse flow environments within the reactor. However, it is critical to recognize that while the $k-\omega$ SST model offers superior accuracy in near-wall treatments, it does so at a higher computational cost, which may limit its applicability in routine engineering analyses where computational resources are constrained.

The near-wall treatment is particularly critical in MSR applications due to the presence of steep thermal and momentum gradients near reactor structures. Accurate modeling of these regions is essential for predicting heat transfer, wall shear stress, and, ultimately, the structural integrity of reactor components. The study highlights the importance of using a low-y^+ mesh resolution when applying the $k-\omega$ SST model, as this approach allows for the direct resolution of the viscous sublayer without relying on wall functions, which can introduce significant inaccuracies in critical regions. The Jayatilleke treatment for temperature profiles in the near-wall region should be employed to ensure that thermal transport is accurately captured, especially given the low thermal diffusivity of molten salts.

In addition to near-wall treatments, the study recommends incorporating corrections for vortex stretching and low Reynolds number effects within the $k-\omega$ SST model. These corrections are essential for accurately capturing turbulence production mechanisms, particularly in regions with strong rotational flows and transitional flow regimes. Vortex stretching, a key mechanism in turbulence production, is especially prevalent in the swirling and recirculating flows characteristic of MSRs. The failure to account for these effects can lead to significant underpredictions of turbulent kinetic energy and, consequently, inaccuracies in the simulation of reactor dynamics.

While the $k-\omega$ SST model demonstrates superior performance in many aspects, it is also essential to acknowledge the scenarios where the $k-\epsilon$ model may be more appropriate. The $k-\epsilon$ model, despite its limitations in near-wall accuracy, remains a viable option for bulk flow predictions where the flow is less influenced by boundary layer effects. Its lower computational requirements make it an attractive option for preliminary design studies, parametric analyses, or regions of the reactor where the flow is fully developed and the impact of boundary conditions is minimal. However, critical assessments must be made to ensure that the use of the $k-\epsilon$ model does not compromise the overall accuracy of the simulation, particularly in safety-critical applications.

The integration of RANS turbulence models with other physical domains, such as neutronics and thermo-mechanics, presents another layer of complexity that must be carefully managed. The coupled nature of these domains in MSRs means that inaccuracies in thermal-hydraulic modeling can have cascading effects on other aspects of reactor behavior, such as reactivity control, structural integrity, and species transport. This study recommends the use of domain-overlapping techniques and consistent data exchange protocols to ensure that coupled simulations accurately reflect the interactions between different physical domains. For instance, feedback mechanisms between the thermal-hydraulic model and the neutronics solver must be tightly coupled to capture the dynamic behavior of the reactor under varying operational conditions.

Validation against experimental data and higher-fidelity models, such as LES, is indispensable for establishing the credibility of RANS models in MSR applications. The study underscores the importance of continuous validation efforts, given the scarcity of experimental data specific to MSRs. While LES provides

a valuable benchmark for RANS models, the computational expense associated with LES limits its use to validation and benchmarking purposes rather than routine engineering analyses. Therefore, the development of a comprehensive experimental database, alongside continued LES studies, is crucial for refining and validating RANS models, ensuring that they remain robust across the diverse operational scenarios encountered in MSRs.

In conclusion, while RANS turbulence models, particularly the $k-\omega$ SST model, offer a promising approach for the thermal-hydraulic analysis of pool-type MSRs, their application requires careful consideration of model selection, validation, and integration with other physical domains. The recommendations provided in this study aim to guide the application of these models in a way that balances accuracy with computational efficiency, ensuring that MSR simulations are both reliable and practical for engineering purposes. As the development of MSRs progresses, ongoing refinement of these models, informed by experimental validation and higher-fidelity simulations, will be essential to address the evolving challenges associated with these advanced reactor designs.

2.6. Conclusions

This study evaluated the implementation and performance of the $k-\epsilon$ and $k-\omega$-SST RANS turbulence models within the MOOSE for the analysis of MSRs. The focus was on evaluating the applicability of these models for the thermohydraulic analysis of open-core pool-type MSRs, specifically using the L-MCR as a representative case.

The validation of both turbulence models against canonical experimental data for channel flow, backward step, and vortex flow in a curved pipe validated the performance of these RANS models developed in MOOOSE against direct numerical simulation data and experiments. It was observed that the $k-\omega$-SST model with resolved wall treatment provides superior accuracy. However, when dealing with wall modeling, i.e., high-y^+, both the $k-\epsilon$ and $k-\omega$ SST models perform similarly. Within the limitations of the RANS models, a reasonable agreement between both models and the validation data is observed, confirming the implementation of these turbulent models in MOOSE.

Comparison with high-fidelity LES for the L-MCR highlighted the limitations of RANS models in capturing the complex turbulent flow structures within the reactor core. Although the $k-\epsilon$ and $k-\omega$ SST models perform approximately equally well for this reactor core, they have limitations in capturing the flow field phenomena in the reactor core. However, both models were accurate in capturing integral quantities for reactor operation, such as the pressure drop across the core and return lines.

The study also investigated the effect of turbulence modeling on the thermal field during operation of the L-MCR. It was observed that the choice of turbulence model can slightly influence the temperature distribution in the reactor core, which could eventually lead to different reactor operation metrics. Therefore, the integration of RANS models with other physical domains requires careful calibration and validation to ensure that the coupled simulations accurately capture the metrics required for reactor physics operation.

Future work should focus on further validation against experimental data and the development of hybrid modeling approaches that combine the strengths of RANS and LES for more accurate and computationally efficient MSR simulations. In addition, coupled multiphysics models of L-MCR involving neutronics, thermohydraulics and thermomechanics will be developed to perform an integral evaluation of the impact of RANS turbulence models on the reactor steady state and postulated transients.

3. NEAR-WALL FUNCTION CORRECTIONS IN MOOSE AND VALIDATION DUE TO ROUGHNESS AND STREAM-WISE AND TRANSVERSAL CURVATURE FOR MSR MODELING

This section presents a copy of the article that was submitted to Annals of Nuclear Energy as part of this M2 in August 2024.

3.1. Introduction

MSR are a category of reactors based on the concept of using a molten salt as both fuel and heat carrier. Mainly designed during the 50s and the 60s, the concept has been proven to work with the MSRE before being shelved. MSR concepts have reappeared in the 21st century with the idea of Generation IV reactors and has since been the subject of extensive research.

In MSR, fuel salts are materials that have low thermal diffusivity and an internal heat source due to fission power generation. This leads to three major problems. First, the fluid behaves as a heat source and thus changes the temperature distribution in the near wall region. Second, the temperature gradient in the fluid, which is large in molten salts due to their low thermal diffusivity, induces gradients in the thermomechanical properties of the molten salt. Finally, the molten salts are very corrosive, creating near-wall roughness that alters the near-wall velocity and temperature profiles. The first two issues have already been addressed by Tano et al. [24], where it was shown that corrections to the wall functions due to the internal heat source and temperature gradients are mostly second order corrections. Therefore, this study focuses mainly on wall roughness when dealing with the issues related to molten salts.

MSRs are typically designed with closed salt loops in the primary and intermediate circuits. In this loop, the flow deflects and swirls at the sharp or rounded elbows and corners when the flow circulates through this one. In addition, in the MSR design with internal core moderators, as the flow circulates into or out of the plenums and into the reactor core, one observes converging or expanding flows, respectively, resulting in a significant impact on the near wall velocity and temperature profiles. Therefore, this work also investigates the impact of wall function corrections due to transverse curvature in the wall function corrections used for MSRs.

Fluid flow modeling in MSRs for engineering analysis and design typically relies on RANS approaches for turbulence modeling because high-fidelity models would consume an enormous amount of computational time due to the mesh resolution needed for higher-fidelity models and the size of the reactor. RANS models have recently been added to the INL's MOOSE. These models previously relied on standard wall function formulations, i.e., the wall functions are not corrected for roughness and curvature. This paper discusses the implementation and validation of roughness and transverse curvature corrections in the Navier-Stokes module of MOOSE. This validated implementation is then used to study the effect of roughness and curvature corrections in the multiphysics modeling of the steady-state operation of MSRs.

The rest of this article is organized as follows. In section 3.2., the standard wall function formulation used in MOOSE is reviewed. Then, in section 3.3., the modifications in the wall function formulations due to roughness and transversal curvature are discussed. Next, in section 3.4., the validation of the roughness and transversal curvature wall function implementations are validated against selected experiments. Finally, section 3.5. utilizes multiphysics models of the MSRE and the MSFR to analyze the impact that roughness and curvature corrections have on the steady-state fields during the operation of MSRs.

3.2. Review of the standard formulations to the wall function

The current work utilizes an incompressible fluid dynamics formulation and the standard $k-\epsilon$ model for turbulence modeling. The fluid-part near-wall treatment relies on computed near-wall profiles for the velocity, turbulence kinetic energy (k), and its dissipation rate (ϵ), which, in the $k-\epsilon$ model, are ultimately translated as fixed conditions for the first cell near the wall in the domain. This model is complemented for additional measured profiles for the turbulent temperature field near the wall, which is translated in the model as an equivalent heat flux at the wall boundaries. These near-wall profiles change due to curvature and roughness present in the flow domain.

The modifications to the wall functions are introduced in the next section. However, the objective of this section is to provide a quick overview of the functions that are used usually to describe this near-wall treatment, under the assumptions that the fluid has constant thermophysical properties, no internal heat source, and is stationary flowing next to a smooth flat wall.

Close to the wall, the flow can be divided in 3 different layers : (i) the viscous sublayer, where the flow is dominated by viscous interactions; (ii) the log layer, where the stress in the flow is mainly produced by turbulent effects; and (iii) the buffer layer, which is the transition layer between those two. As regards the area of validity of these laws, it is widely assumed that the viscous sublayer extends from the wall to $y^+ = 5$. The values given by Tano et al. [24], and typically used in the scientific literature, will be used here, with a buffer layer going from $y^+ = 5$ to $y^+ = 30$ and a log layer that extends for $y^+ \geq 30$.

In this article, y^+ denotes the dimensionless value for the distance to the wall $y^+ = \frac{y u_\tau}{\nu}$, where y is the distance to the centroid of the nearest wall cell, u_τ is the friction velocity, and ν is the kinematic viscosity. More generally every quantity with a $+$ exponent will be normalized using u_τ and ν, with $u_\tau = \sqrt{\frac{\tau_w}{\rho}}$, where τ_w is the shear stress, the w index meaning this is the quantity at the wall and ρ is the density.

3.2.1. Velocity profile

In the viscous sublayer, the fluid is governed by the viscous forces, and so the incompressible momentum conservation equation reads as follows:

$$\frac{\partial}{\partial y}\left(\rho\nu\frac{\partial \overline{u}}{\partial y}\right) = 0\,. \tag{21}$$

With the definition $\tau_w = \rho\nu\frac{\partial \overline{u}}{\partial y}|_w$, and integrating over the direction perpendicular to the wall y, one obtains the following profile of the velocity for the viscous sublayer:

$$\overline{u}(y) = \frac{\tau_w}{\rho\nu} y\,, \tag{22}$$

or by using the dimensionless quantities defined previously, the following non-dimensional profiles are obtained:

$$u^+ = y^+\,. \tag{23}$$

To deal with the log-layer, the most common approach is to use the Prandtl mixing length model, as it is done by Hutchinson et al. [25]. This model defines a length scale ℓ, called the mixing length, which

represents the average distance a particle of fluid can travel before mixing with the ambient fluid and changing its properties. The following relationship then comes at first order for the stream-wise velocity:

$$u = \overline{u} + u' \approx \overline{u} + \ell \frac{\partial \overline{u}}{\partial y} \tag{24}$$

where $\overline{u}$ is the Reynolds average of the stream-wise velocity and u' is its fluctuating component. Then, by assuming the fluctuations of the velocity perpendicular to the wall, v', of the same order than fluctuations of u' one obtains:

$$\tau = \rho \overline{u'v'} \approx \rho \ell^2 \left(\frac{\partial \overline{u}}{\partial y} \right)^2 . \tag{25}$$

By defining ℓ with the value mentioned by Kind et al. [26] of $\ell = \sqrt{\frac{\tau}{\tau_w}} \kappa y$ with $\kappa \approx 0.41$ the Von Karman constant comes the following expression:

$$\frac{\partial \overline{u}}{\partial y} = \sqrt{\frac{\tau_w}{\rho}} \frac{1}{\kappa y} , \tag{26}$$

which, by integrating and rescaling, yields the law of the wall for the outer logarithmic layer:

$$u^+ = \frac{1}{\kappa} ln(E y^+) , \tag{27}$$

with $E \approx 9.8$ an experimental constant.

In the computational implementation, a split domain is used with a sharp transition between the viscous and logarithmic layers. In this one, the viscous law is used for $y^+ \leq y_v^+$, then the log law is used. The zero eddy viscosity height $y_v^+ \approx 11.4$ is defined as the value of y^+ where the log law is crosses the linear law of the viscous sublayer as follows:

$$y_v^+ = \frac{1}{\kappa} ln(E y_v^+) . \tag{28}$$

3.2.2. Temperature profile

In the viscous sublayer, the heat flux is governed by molecular diffusion. So, the energy conservation equation can be written as follows:

$$\frac{\partial}{\partial y} \left(\lambda \frac{\partial \overline{T}}{\partial y} \right) = 0 , \tag{29}$$

and then, by introducing the expression for the near-wall heat flux $q_w = -\lambda \frac{\partial \overline{T}}{\partial y}|_w$, one reaches the following expresssion:

$$\overline{T} = -\frac{q_w}{\lambda} y + T_w . \tag{30}$$

By defining the dimensionless quantity $T^+ = \frac{\rho c_p (T_w - \overline{T}) u_\tau}{q_w}$ and using the Prandtl number $Pr = \frac{\mu c_p}{\lambda}$, the following expression for the non-dimensional wall temperature T^+ can be obtained:

$$T^+ = Pr\, y^+ . \tag{31}$$

To deal with the log layer, the model of Jayatilleke [27] has been chosen. This model is based on the idea that temperature and speed profile have similar profiles in the log layer, which yields :

$$T^+ = \frac{1}{\kappa_{th}} ln(E_{th} y^+) . \tag{32}$$

This equation can be rewritten using the fraction $\frac{\kappa}{\kappa_{th}}$ that represents the ratio between the eddies diffusivity for momentum and heat transfer, and $P_w = \frac{1}{\kappa} ln(\frac{E_{th}}{E})$ that represents the resistance of the laminar sub-layer to heat transfer over its resistance to momentum transfer:

$$T^+ = \frac{\kappa}{\kappa_{th}} (u^+ + P_w) . \tag{33}$$

For smooth pipe flow data, Jayatilleke got the following experimental value for P:

$$P_w = 9.24 \left(\left(\frac{\kappa_{th} Pr}{\kappa} \right)^{\frac{3}{4}} - 1 \right) \left(1 + 0.28 exp \left(-0.007 \frac{\kappa_{th} Pr}{\kappa} \right) \right) , \tag{34}$$

with $\kappa_{th} \approx 0.38$ being a fitting constant.

3.3. Proposed modifications to the near-wall treatment

The law of the wall studied previously is based on some hypothesis that aren't always verified, especially in the case of Molten Salt Reactors:

1. there is a significant corrosion expected in these reactors, and as a result the hypothesis of smooth walls becomes no longer valid,
2. most of the flows in these reactors are in contact with walls that aren't flat and hence, the ideal mixing length hypothesis in the wall function formulation is looses validity.

Corrections are therefore necessary, so this section will try to propose some.

3.3.1. Roughness corrections

The corrections proposed are conceived for k type roughness, i.e., for surfaces where the distance between two elements is large compared to the height of these elements ($d/h > 3$ to give an order of magnitude).

According to King [28], Orych [29], Jimenez [30], and Kadivar [31], having a rough wall increase the skin friction coefficient and so the wall shear stress because of the drag created by the roughness elements. Jimenez

[30] and Kadivar [31] also underline that roughness induces some changes in the structure of turbulence, by shaping the eddies next to the wall. Moreover, having roughness elements create a part of the domain where the flow is not well defined, because some places are occupied by these roughness elements.

The changes in the shear stress introduced by wall roughness induce a change in the mean velocity profile near the wall; the first studies to determine changes in relation to the standard law of the wall were conducted by Nikuradse [32]. The author pointed out that the logarithmic law is preserved, but shifted by a constant value depending on a parameter k_s called the equivalent sand grain roughness. The previously mentioned article found the following law for the velocity:

$$u^+ = \frac{1}{\kappa} ln\left(\frac{y^+}{k_s^+}\right) + B \tag{35}$$

with the shifting constant provided as a function of the k_s^+ as follows:

$$B = \begin{cases} 5.5 + \frac{1}{\kappa} ln(k_s^+) & \text{for } 1 \leq k_s^+ \leq 3.5 \\ 6.59 + 1.52 ln(k_s^+) & \text{for } 3.5 \leq k_s^+ \leq 7 \\ 9.58 & \text{for } 7 \leq k_s^+ \leq 14 \\ 11.5 - 0.7 ln(k_s^+) & \text{for } 14 \leq k_s^+ \leq 68 \\ 8.48 & \text{for } 68 \leq k_s^+ \end{cases} \tag{36}$$

A few years later, a study led by Colebrook led to another correction for the mean velocity near the wall, which uses the same idea to preserve the logarithmic profile, but changing the value of B :

$$u^+ = \frac{1}{\kappa} ln(y^+) + 5.5 - ln(1 + C_{rough} k_s^+) \tag{37}$$

Both Nikuradse and Colebrook models converge to the same values of correction, proportional to $-ln(k_s^+)$ for a totally rough regime ($k_s^+ \geq 70$). These corrections are depicted in Figure 21. This could also lead to think of a type of correction which is a simpler intermediate between the two mentioned above, the asymptotic correction. This correction is proposed as follows:

$$u^+ = \begin{cases} \frac{1}{\kappa} ln(E y^+) & \text{for } k_s^+ \leq 2.7 \\ \frac{1}{\kappa} ln\left(\frac{E_{rough} y^+}{k_s^+}\right) & \text{for } k_s^+ \geq 2.7 \end{cases} \tag{38}$$

with E being the same constant used in the standard law of the wall and E_{rough} a constant that will be determined later for fitting the expected pressure drops from rough walls in the Moody chart. The proposed asymptotic correction is also depicted in Figure 21.

This study will mainly be focused on Colebrook's correction and asymptotic correction. Colebrook's correction is evaluated since it is the one generally used for industrial applications dealing with flow over rough walls and it is the one typically implemented in production CFD codes. The asymptotic correction is also evaluated since it has the advantage of being faster to compute.

One more point that should be specified when dealing with roughness is the way the roughness equivalent sand height should be calculated. The the roughness equivalent sand height should take into account both the

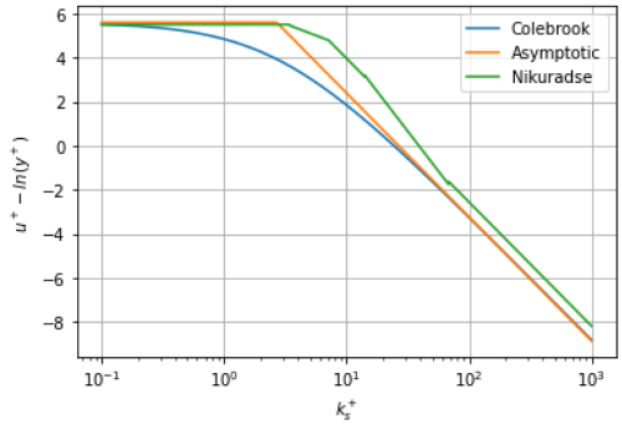

Figure 21. Comparison between the 3 corrections for roughness

height of the roughness elements and their shape. Danberg and Sigal [33] proposed the following formula to calculate k_s that meets requirements:

$$\frac{k_s}{h} = \begin{cases} 0.003215\Lambda_s^{4.925} & \text{for } 1.4 \leq \Lambda_s \leq 4.89 \\ 8.0 & \text{for } 4.89 \leq \Lambda_s \leq 13.25 \\ 151.71\Lambda_s^{-1.1379} & \text{for } 13.25 \leq \Lambda_s \leq 100 \end{cases} \tag{39}$$

where Λ_s is a shape parameter defined by :

$$\Lambda_s = \frac{S}{S_f}\left(\frac{A_f}{A_s}\right)^{-1.6}, \tag{40}$$

with $\frac{S}{S_f}$ the ratio of the reference area before adding the roughness to the frontal area of the roughness, and $\frac{A_f}{A_s}$ the ratio of the frontal area of a roughness element over the wet surface of this element.

To implement this correction computationally in MOOSE, the only thing needed was a change in the way used to calculate the friction velocity u_τ. This method used normally a Newton-Raphson method to solve the equation:

$$\frac{u}{u_\tau} = \frac{1}{\kappa} ln\left(\frac{Eyu_\tau}{\nu}\right). \tag{41}$$

However, on the one hand, for Colebrook's correction the equation to solve becomes:

$$\frac{u}{u_\tau} = \frac{1}{\kappa} ln\left(\frac{Ey}{\frac{\nu}{u_\tau} + k_s}\right). \tag{42}$$

On the other hand, the interest of the asymptotic correction becomes evident here, because Newton method is not necessary, since the equation to solve becomes directly :

$$u_\tau = \frac{\kappa u}{ln\left(\frac{Ey}{k_s}\right)} \tag{43}$$

3.3.2. Transverse curvature correction

This section will only study the effects of transverse curvature, in other words, the curvature perpendicular to the main direction of the flow. This kind of curvature corrections are typically needed for swirling or recirculating flows. The main source used in this section will be an article by Kind et al. [26].

The curvature corrections do not introduce any change in the viscous sublayer, because equation (21) is still valid for curved walls. This is because the fact that the wall is curved do not change the integration result in the direction perpendicular to the wall from equation (23). However, changes happen in the log layer when dealing with swirling flows in curved pipes. In this case, the curvature creates a dissymmetry in the problem which prevents to use a flow with just one speed coordinate as done in section 3.2.1..

For convenience, the problem will now be studied in cylindrical coordinates, with the axis being the one normal to and going through the center of the osculating circle to the curved wall surface (this surface could be convex or concave). The radius of curvature will be noted R.

The definition of mixing length used in section 3.2.1. will be used, but this time two mixing length will be used, one for the swirling part of the flow and the other for the non-swirling part as follows:

$$\ell_x = \sqrt{\frac{\tau_x}{\tau_{xw}}}\kappa y, \qquad \ell_\theta = \sqrt{\frac{\tau_\theta}{\tau_{\theta w}}}\kappa y. \tag{44}$$

By rewriting the equation (25) in vectorial form and projecting it along axial $\overrightarrow{e_x}$ and swirling $\overrightarrow{e_\theta}$ directions, it becomes:

$$\tau_{xw} \approx \rho \ell_x^2 \frac{\partial \overline{u}}{\partial r} || \overrightarrow{V} ||, \tag{45}$$

$$\tau_{\theta w} \approx \rho \ell_\theta^2 \left(r \frac{\partial}{\partial r} \left(\frac{\overline{w}}{r} \right) \right) || \overrightarrow{V} ||, \tag{46}$$

where τ_{xw} is the shear in the axial direction, $\tau_{\theta w}$ the one in the swirling direction, and $\overrightarrow{V}|$ denotes the velocity vector and $|| \overrightarrow{V} ||$ its norm. Then by using $\tau_w = \rho(\kappa y)^2 || \overrightarrow{V} ||^2$ the equations can be re-written as follows:

$$\frac{\tau_{xw}}{\rho} \approx \sqrt{\frac{\tau_w}{\rho}} \kappa y \frac{\partial \overline{u}}{\partial r} \tag{47}$$

$$\frac{\tau_{\theta w}}{\rho} \approx \sqrt{\frac{\tau_w}{\rho}} \kappa y \left(r \frac{\partial}{\partial r} \left(\frac{\overline{w}}{r} \right) \right) \tag{48}$$

Then the reasoning continues by defining the axial shear velocity $u_\tau = \sqrt{\frac{\tau_{xw}}{\rho} \frac{\tau_{xw}}{\tau_w}}$ and the tangential shear velocity $w_\tau = \sqrt{\frac{\tau_{\theta w}}{\rho} \frac{\tau_{\theta w}}{\tau_w}}$. Here both these equations can be integrated by keeping in mind that $dr = dy$ if the surface is convex and $dr = -dy$ if it is concave. That gives us the following result, where the plus sign is used for a convex surface and the minus for the concave one.

$$\frac{u}{u_\tau} \approx \frac{1}{\kappa} ln \left(E \frac{y u_\tau}{\nu} \right) \tag{49}$$

$$\frac{w}{w_\tau} \approx \frac{1}{\kappa} \left(1 \pm \frac{y}{R} \right) ln \left(E \frac{y w_\tau}{\left(1 \pm \frac{y}{R}\right) \nu} \right) \tag{50}$$

Note that only the swirling component of the flow is modified in these equations.

Finally, the shear velocities need to be compounded to an effective turbulent viscosity for the near-wall region.

A simple choice is to perform a direct vector composition for the wall shear stress given by $\tau_w = \rho\left(u_\tau^2 + w_\tau^2\right)$. This allows us to determine the modified value of μ_t as follows:

$$\mu_t = \frac{\tau_w y}{\sqrt{(u^2 + w^2)}} - \mu = \frac{\rho\left(u_\tau^2 + w_\tau^2\right) y}{\sqrt{(u^2 + w^2)}} - \mu \tag{51}$$

However, in practice, these modifications give only a change of less than 2 percent in the the value of τ_w. Hence, the turbulent viscosity and the speed profile only change really slightly, which is far from the increase of 20 % mentioned by Kim and Rhode [34] for example. This under-prediction is because both productions of stress in the axial and swirling directions are not independent. To overcome this difficulty, the authors propose to add a coupling term between u_τ and w_τ, with α a parameter whose value will be further discussed in the validation section:

$$\mu_t = \frac{\rho\left(u_\tau^2 + w_\tau^2 + \alpha u_\tau w_\tau\right) y}{\sqrt{(u^2 + w^2)}} - \mu \tag{52}$$

Note that the α parameter should be a function of the radius of curvature. This is because the extent to which the axial and swirling friction velocities blend will be a function of the ratio between the perpendicular distance to the wall and the circumference in the swirling direction. Further studies should be conducted to determine a precise profile for α, however a few elements come to mind when developing this function:

- α should go to 0 if the radius of curvature goes to infinity, because $\alpha = 0$ for a flat wall,
- $|\alpha|$ should decrease when $|R^+|$ increases,
- α should be positive for concave surfaces to increase the wall shear stress and negative for convex surfaces to decrease it,
- $\alpha \geq -2$ because the shear stress at the wall is always positive.

Since the scope of this work is to assess the need for curvature corrections in a MSR concept, this work limits to the selection of a value of α that will be validated against an experiment and used for MSR concept evaluated. However, the development of a profile for curvature correction will be developed as future work and will integrate more experiments to develop this profile and avoid potential systematic biases.

In MOOSE, the curvature modifications were implemented by defining a method to calculate the decomposition of the velocity into its swirling and main component using the main axis of the flow, then defining a function to calculate w_τ by solving the equation (50) with a Newton method, and finally replacing the calculation of μ_t by its new value.

The validation of the proposed modifications for roughness and curvature are detailed in the next section.

3.4. Model validation

This section is divided into two parts. First, the validation of the roughness correction for the wall function is evaluated. Then the validation of the curvature correction is analyzed. For each case, the meshes add a

boundary layer adjacent to the wall and aim for $y^+ > 30$ for the first cell to be in the turbulent boundary layer, where the near-wall corrections are active. The bulk of each mesh was refined until the results varied less than 1% with successive refinements for the velocity fields studied in each case, which was considered a reasonable value for evaluating the impact of the implemented corrections against the experiments selected.

3.4.1. Validation of the wall function correction for roughness

The first part of the validation process for the rough speed profile was to get the friction coefficient to match the values given on the Moody chart, which were calculated using the Colebrook equation (53) as follows:

$$\frac{1}{\sqrt{f}} = -2log_{10}\left(\frac{k_s}{3.7D_h} + \frac{2.51}{Re\sqrt{f}}\right) \tag{53}$$

The simulations were performed in a 2D axi-symmetric model of pipe long enough for the flow to fully develop and the pressure drop was computed once the pipe reaches the fully developed flow condition. In other words, the simulated value of the friction coefficient was determined by getting the value of pressure drop, Δp, at an outlet segment of the pipe, and then using the following expression:

$$f = \frac{2D_h}{\rho\overline{U}^2}\frac{\Delta p}{l}, \tag{54}$$

where $D_h = D$ is the hydraulic diameter of the pipe, $\overline{U}$ is the average velocity, and l was the length of the outlet segment chosen for computing the pressure drop. The results obtained for the asymptotic correction with a value of $E_{rough} = 26.6$, and for the Colebrook correction with a value of $C_{rough} = 0.366$ are presented in Table 8 and Table 9, respectively, for different Reynolds numbers and relative roughness.

	Re = 65300		Re = 145000		Re =653000	
k_s/D	Moody	Computed	Moody	Computed	Moody	Computed
0.001	0.0232	0.0201	0.0215	0.0201	0.0201	0.0201
0.003	0.0281	0.0267	0.0271	0.0267	0.0264	0.0266
0.01	0.0388	0.0384	0.0383	0.0383	0.0380	0.0382
0.03	0.0576	0.0572	0.0574	0.0572	0.0572	0.0571

Table 8. Comparison of the Darcy–Weisbach friction factors predicted by the asymptotic correction against the ones predicted by the Moody chart.

	Re = 65300		Re = 145000		Re =653000	
k_s/D	Moody	Computed	Moody	Computed	Moody	Computed
0.001	0.0232	0.0232	0.0215	0.0216	0.0201	0.0204
0.003	0.0281	0.0282	0.0271	0.0273	0.0264	0.0268
0.01	0.0388	0.0390	0.0383	0.0386	0.0380	0.0383
0.03	0.0576	0.0575	0.0574	0.0572	0.0572	0.0570

Table 9. Comparison of the Darcy–Weisbach friction factors predicted by the Colebrook correction against the ones predicted by the Moody chart.

The comparison against the Moody chart shows that the friction coefficient for the asymptotic correction doesn't depend on the Reynolds number, so it matches the Moody chart quite well only when the wall is completely rough. On the other hand, the Colebrook correction matches the Moody diagram well everywhere. As a result, the focus will afterwards be on the Colebrook correction because of its higher accuracy, even if the asymptotic correction could be used in case of full roughness to save computational time.

The second part of the validation was to compare the results of the experiment using the square duct of the case 52 of the ERCOFTAC database [35]. The tests consists of a square pipe with 50 mm $\times$ 50 mm side lengths and with two smooth and two rough walls. The experimental setup for this test is detailed in Table 10.

This pipe was modeled made on MOOSE and the computational mesh used in these simulations is depicted in Figure 22. This experimental setup was also long enough for the turbulent flow to fully develop. To reproduce this experiment, a choice was made to use a 2D model of the fluid for $z = 0$, $0 \leq y \leq 25$ mm and $0 \leq x \leq 4.5$ m. The wall at $y = 25$ mm is rough and the boundary at y = 0 is symmetrical.

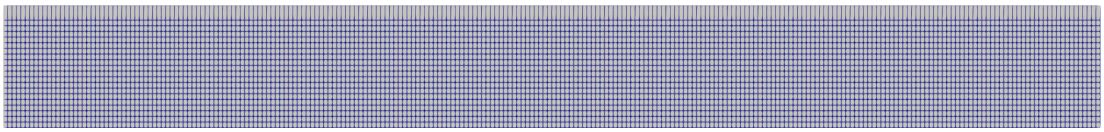

Figure 22. Mesh for the validation of the roughness speed profile

Parameter	Value
Dimensions	$4.5\ m \times 50\ mm$
Inlet Axial Velocity	$21.4\ m/s$
Inlet Radial Velocity	$0\ m/s$
Viscosity	$1.8 \cdot 10^{-5}\ kg/m/s$
Density	$1.225\ kg/m^3$
Reynolds number	$6.5 \cdot 10^4$
Roughness	$3.2\ mm$
Validation Criteria	Renormalized velocity profile

Table 10. Parameters of the roughness validation case for ERCOFTAC case 52

For validation purposes, the first step was to determine the equivalent sand roughness. That was done using the formula proposed by Danberg and Sigal described in section 3.3.1.. Here the roughness elements are square rods that extend on the whole width of the pipe, with a 1 mm side length and 10 mm spacing. This allows to write $\frac{S}{S_f} = 10$ and $\frac{A_f}{A_s} = \frac{1}{2}$ so $\Lambda_s \approx 30$, and so $k_s = 3.2mm$.

To validate the correction, the quantity studied was the speed profile along the axis perpendicular to the wall, and since the simulation was in 2 dimensions and the experiment in 3 dimensions, the value was renormalized by the mean value of the velocity.

Figures 23 and 24 show that the speed profile with the correction for roughness is always much closer to the experimental data than the one without, and also that the relative difference between the experimental data and the simulation with the correction does not exceed 5%. This allows us to conclude that the correction for the roughness speed profile is validated for internal flows with rough walls.

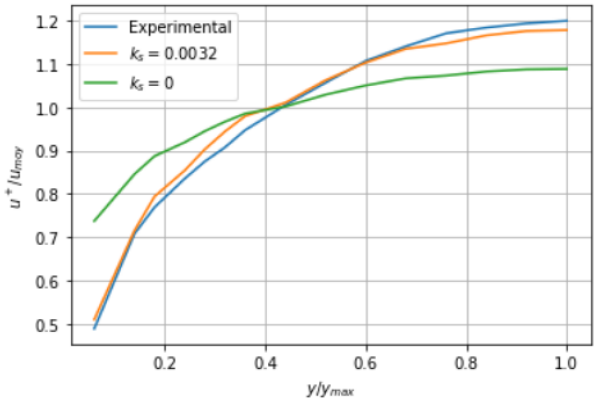

Figure 23. Experimental and simulated speed profiles as a function of y

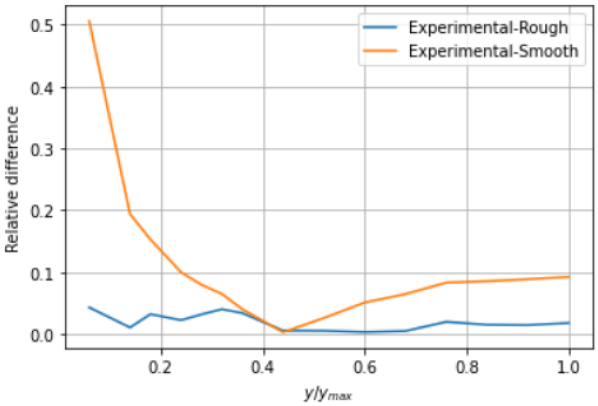

Figure 24. Relative difference between simulated and experimental profiles

3.4.2. Validation of the near-wall curvature correction

To validate the correction for curvature, the choice that was done was to use the case number 60 of the ERCOFTAC database [36]. In this experiment, a turbulent flow goes first through a swirl generator and then through a conic diffuser. The experiment is modeled in 3D. The reason for using a 3D domain is that curvature corrections will act in swirling flows and swirling flow cannot be modeled in less dimensions, i.e., 2D or 1D. The swirl generator is not resolved in our model and the flow swirl is imposed as an inlet boundary condition. The curvature radius varies from 130 mm to approximately 220 mm along the diffuser. The mesh and experiment domain are depicted in Figure 25, while the main parameters of this experiment are detailed in Table 11

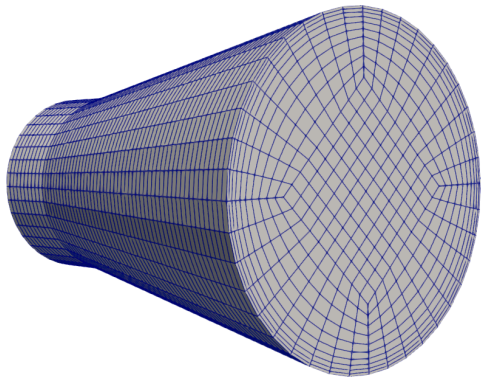

Figure 25. Mesh for validation of the curvature correction

Parameter	Value
Dimensions	610 mm $\times$ 130 to 220 mm for the radius
Inlet Axial Velocity	11.6 m/s
Inlet Maximum Swirling Velocity	6.7 m/s
Viscosity	$1.8 \cdot 10^{-5}$ $kg/m/s$
Density	1.225 kg/m^3
Reynolds number	$2.06 \cdot 10^5$
Validation Criteria	Profile for the axial velocity

Table 11. Parameters for ERCOFTAC case 60 for curvature validation.

The coordinates for selection of the measurement points is labeled x. In the experiment, the x coordinate is the distance from the beginning of the expansion of the diffuser along the wall. The model validation consists of comparing the speed profiles for the experimental data and the simulation with and without curvature correction for the non-swirling component of the velocity at two selected values of x, $x = 175$mm and $x = 405$mm. The results of this comparison are displayed in Figures 26 and 27. In both graphs y represents the distance from the wall into the bulk of the diffuser.

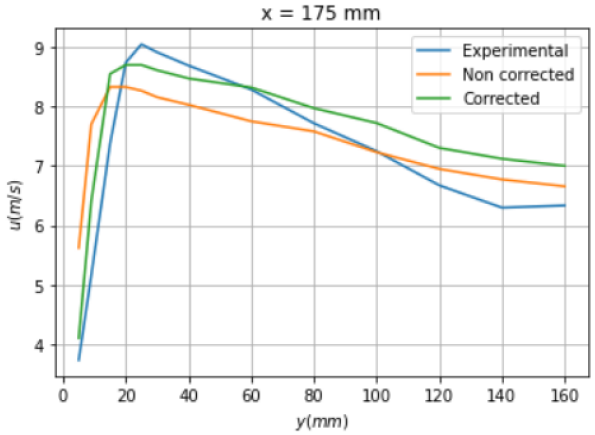

Figure 26. Comparison of the speed profiles for x = 175 mm

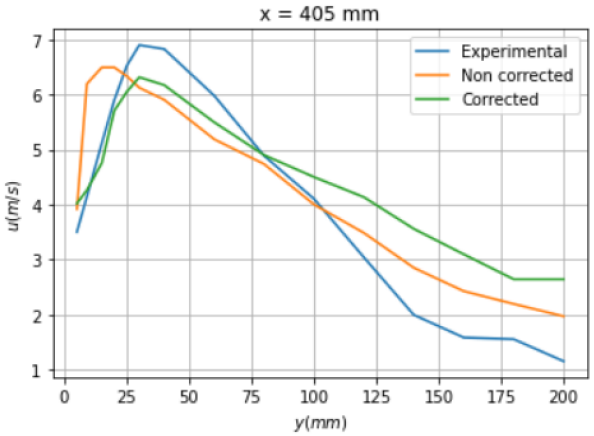

Figure 27. Comparison of the speed profiles for x = 405 mm

With and without the correction, the simulation is too diffusive compared to the experiment close to the centerline, i.e., both simulated profiles are flatter than the experiment and parallel after their maximum. This over-diffusion can be expected in RANS models such as the standard $k-\epsilon$ model used in this work. In this case, the over-diffusivity is caused by the turbulent dynamic viscosity, μ_t, is higher than the one in the experiment close to the centerline, which makes the model hard to correct at the bulk of the flow using wall corrections only. Previous work have suggested the realizable $k-\epsilon$ model as a solution to this problem. Additionally, Humphrey and Pourahmadi [37], have suggested to change the value of C_μ for the whole flow when dealing with swirling flows. This will not be dealt with here as it is outside the scope of the correction to the wall functions. This is, our validation will be primarily focused on the near-wall region. However, our conclusions seem to meet the observations from previous work that suggested that a deeper change than only a wall correction could be necessary when dealing with swirling flows.

Differently than the bulk of the experiment, close to the wall, the turbulent viscosity depends only slightly

on the value of C_μ, and significantly on the value of μ_t at the wall. Finding the appropriate value with the correction is therefore necessary and will be approximately independent of any change in the value of C_μ.

In both Figures 26 and 27, the value of α that has been chosen as $\alpha = 2$. One can notice that in both cases, next to the wall, the predicted velocity profile is closer to the experiments when introducing corrections in the wall functions. In fact, the L^2-error between $y = 0$mm to $y = 50$mm are respectively for $x = 175$mm and $x = 405$mm : 0.236m/s and 0.171m/s when using wall curvature corrections, while it is 0.510m/s and 0.407m/s when using a non-corrected wall profile.

Additionally, in this near-wall region, the model with corrected wall functions matches closely the experiments for $x = 405$mm, while the agreement is slightly worse for $x = 0.175$mm. This is because, the viscosity predicted by the $k - \epsilon$ model is not large enough for $x = 175$mm as the models overpredicts the production of turbulent kinetic energy after the expansion in the diffuser. Overall, this correction improves the model of the swirling flows.

In this section, the validation for the roughness and curvature correction to the wall functions have been addressed. The next section applies these corrections to evaluate the expected operational changes in a selected MSR concept.

3.5. Application to Molten Salt Reactors

In this section the curvature and roughness correction are applied to an MSR for quantifying the impact that the corrections of the wall functions for curvature correction and roughness may have on the operational fields of MSRs. This section is structured as follows. First, the reactor to which the corrections are applied is described. Then, the flow structure through the reactor core is analyzed. Finally, the impact of roughness and temperature corrections is assessed.

3.5.1. Description of the application case

The application model chosen was the L-MCR, which is an open-source generic chloride fuel salt reactor loosely based on TerraPower's open-source specifications of the Molten Chloride Reactor Experiment [17]. This reactor uses a UCl_3-NaCl fuel salt. A multiphysics model of this reactor is publicly available at INL's Virtual Test Bed [38].

Only the primary loop of the reactor, where the molten salt circulates, is modeled. The calculations to determine the power density generated by the nuclear reactions were also performed by MOOSE, but will not be detailed here. In this model, the power source computed by neutronics is applied to the thermal-hydraulics calculations. We refer the interested reader to the documentation of the multiphyiscs model of MCRE [38] for further details on the neutronics calculations for this reactor. For completeness, the operational parameters of the L-MCR are provided in Table 12.

The layout of the L-MCR system is depicted in Figure 28. This reactor involve a reactor core, pump, piping, heat exchanger, and reactor reflector. However, in this simplified model, the reflector is omitted and assumed to have a small convective transfer coefficient, thus considering that the heat losses in the reactor core occur mainly at a postulated heat exchange section. The modeled system consists of the core (in light grey on figure 28) where the power density is non-zero, the pump (in green on figure 28) that generates the force which allows the fluid to circulate, the piping system (in red on figure 28) that is well thermally insulated, and the primary section of a heat exchanger (in blue on figure 28). The system is modeled at thermal equilibrium. This means that the power generated by nuclear reactions is compensated by the extraction of heat at the heat

Parameter	Value
Core Power [kW_{th}]	100
Operation Temperature [K]	900
Rated Mass Flow Rate [kg/s]	21.0
Fuel Salt [mol %]	UCl_3 [33.3%] - NaCl [66.7%]
Fuel Enrichment ^{235}U [wt %]	93.2
Density [kg/m^3]	$4212.6 - 1.0686T$
Specific Heat [$\frac{J}{kg.K}$]	8900.439 - 13.77936 T
Thermal Conductivity [$\frac{W}{m.K}$]	$5.6820 - 8.7832 \times 10^{-3}T$
Dynamic Viscosity [$Pa.s$]	$1.505 \times 10^{-4} e^{\frac{2.666 \times 10^4}{8.314T}}$
Reflector Material	MgO

Table 12. L-MCR specifications

exchanger and by the thermal loss in the piping system.

Once the power density applied in the fuel salt, the thermal-hydraulics calculations for steady-state operation are performed. The steady-state thermal-hydraulics solutions obtained are detailed in the next section.

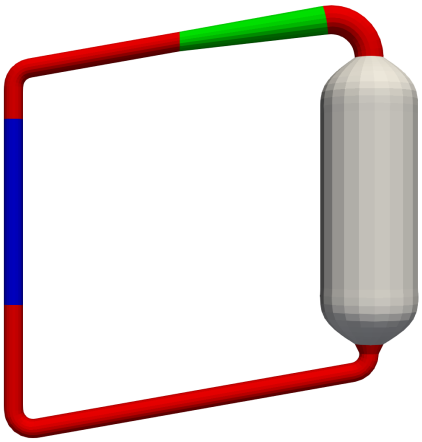

Figure 28. Model of the L-MCR.

3.5.2. Structure of the flow

The results presented in this section are those of the reactor modeling without curvature or roughness correction. These results serve as the reference when comparing against curvature and roughness corrections. The presentation will be divided into two parts, the flow in the return piping system and the core.

3.5.2.1. Description of the flow in the piping system

In Figure 29, a sectional cut of the reactor colored with the speed profile is presented. The flow exits the core of reactor by the top, passes through the pump and the piping system, and finally reenters the core by its

bottom. The flow entering the reactor is pushed to the side due to the geometry of the piping system.

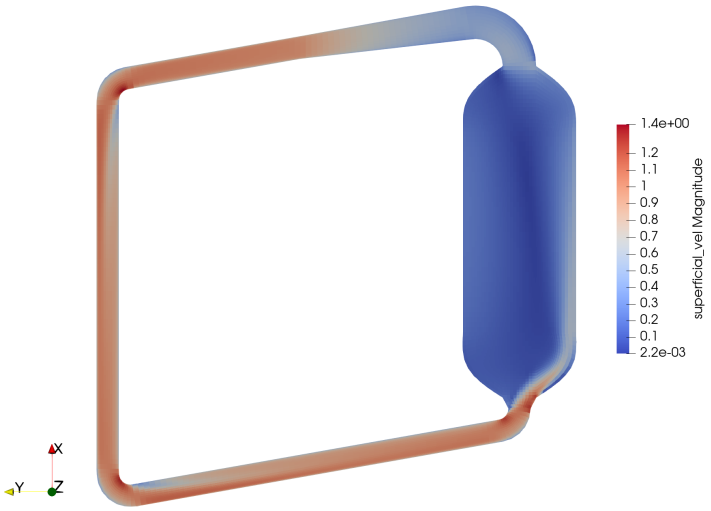

Figure 29. Sectional cut colored with the magnitude of the velocity without correction. The units of the speed are in m/s.

Figures 30 and 31 depict the temperature profile in the system, respectively on a section and at the wall. In terms of temperature the fluid is heated in the core due to the deposited power density. Then, it goes through the piping system and is cooled in the heat exchanger due to interaction with the walls. Next, the flow that has been cooled mixes giving a more homogeneous fluid in term of temperature. Finally, the salt flow reenters the core. The difference for mean temperature between the inlet and the outlet of the core are approximately $7K$, which is the expected order of magnitude as the mass flow rate is approximately $21kg/s$, the thermal capacity of the fluid is $620J/kg/K$, and the power is of $100kW_{th}$.

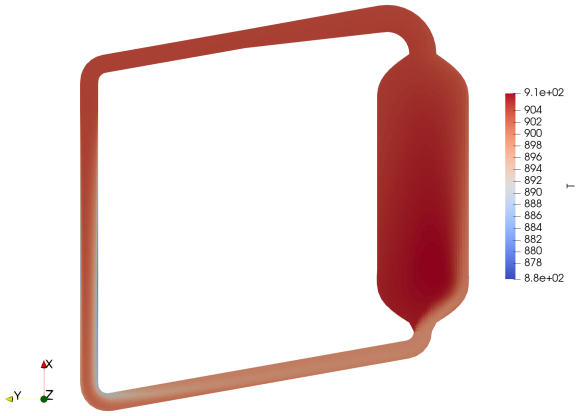

Figure 30. Sectional drawing of the temperature (in K) of the fluid without correction

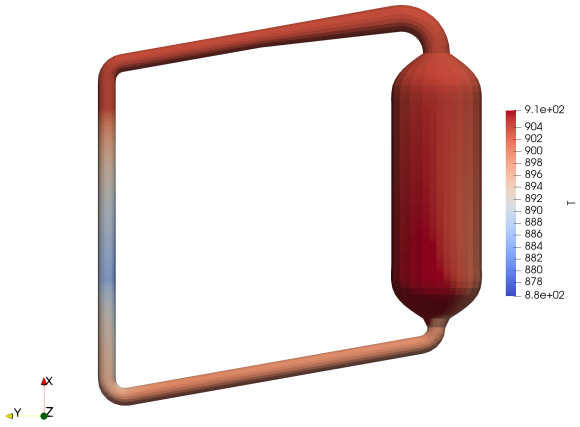

Figure 31. Temperature profile (in K) at the walls without correction

3.5.2.2. *Description of the flow in the reactor core*

The fact that the flow entering the core is pushed to the side, due to the centrifugal acceleration from the piping system, has two consequences on the speed profile in the core. Firstly, as can be seen on Figure 32, it creates a recirculation whose normal axis is the z-axis, with a velocity along the x-axis that varies between $-2.3 \cdot 10^{-1}$m/s and $5.2 \cdot 10^{-1}$m/s. Secondly, it creates two symmetrical swirls whose normal axis is the x-axis as can be seen on figure 33. The velocity along the z axis has been rescaled on figure 33, but its maximum is $5 \cdot 10^{-2}$m/s, so the swirl is not negligible and the curvature correction will therefore be used in the core in the following sections.

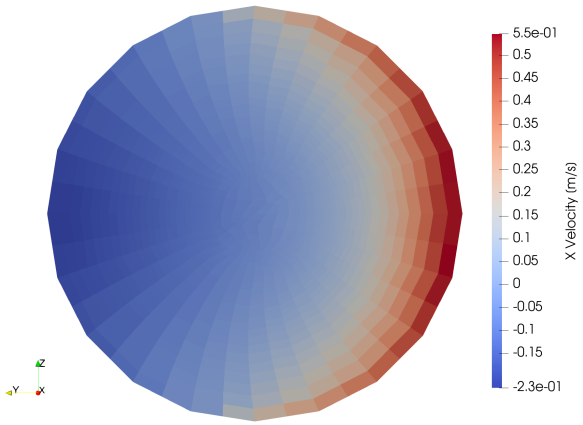

Figure 32. Sectional drawing of the velocity along the x-axis without correction

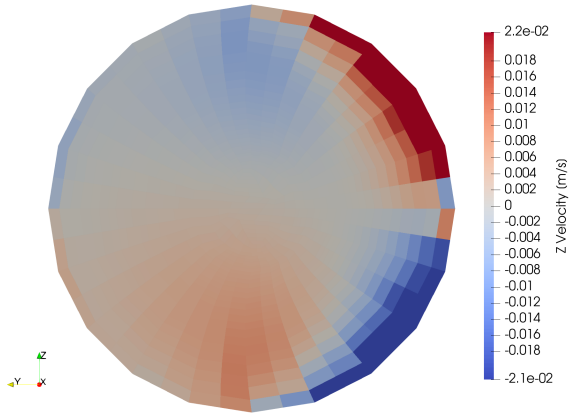

Figure 33. Sectional drawing of the velocity along the z-axis without correction

In terms of temperature profile, as shown in Figure 34, the existence of the swirl normal to the z-axis creates a profile that is not homogeneous for a section of the core normal to the x-axis. The temperature goes from 900 to 906 K, with the minimum where the x-velocity of the flow reaches its maximum, and the maximum where the x-velocity is close to zero.

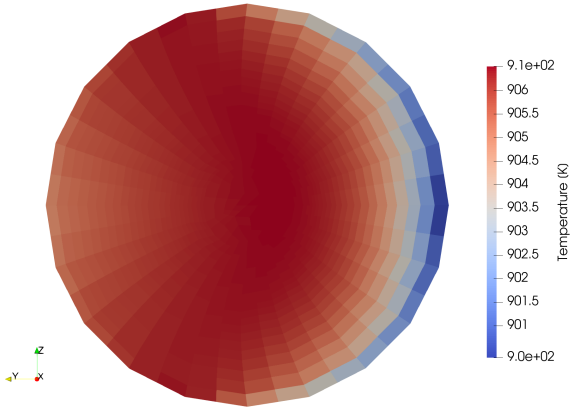

Figure 34. Sectional drawing of the temperature without any correction

Finally, the swirl normal to the z-axis has an effect on the profile of the turbulent viscosity as seen from in Figure 35a. This indeed creates a zone of the flow where the speed along the x axis is close to zero, and in

this zone the turbulent viscosity increases; this is inherent to the $k - \epsilon$ model and due to the way the turbulent viscosity is computed. Figure 35b have been rescaled to show the whole profile of the viscosity, but the maximum reached next to the wall for the turbulent viscosity is 33.

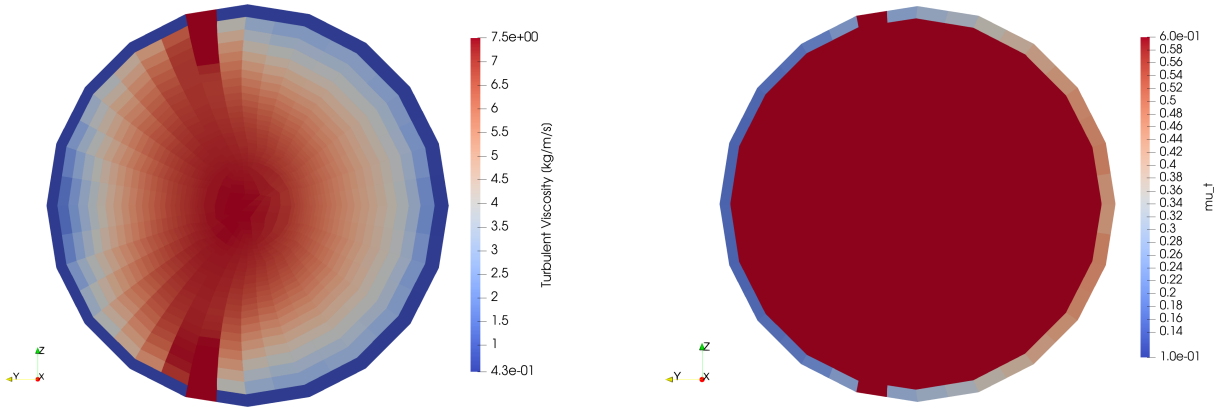

(a) Focus on the bulk values

(b) Focus on the wall values

Figure 35. Sectional drawing of the turbulent viscosity without any correction

3.5.3. Application of the corrections

In this section the changes induced by the corrections will be studied. The first subsection will focus on the corrections for curvature only. Then, the influence of the roughness in these corrections will be examined. As for the validation case in Section 3.4.2., the value of α chosen for the curvature correction was $\alpha = 2$. This section summarizes the main modifications observed by introducing the curvature and roughness correction. Detailed numerical values supporting the narrative in this section can be found in 3.7. and 3.8..

3.5.3.1. Influence of the curvature

All the comparisons displayed below will compare the different profiles with the curvature correction minus the profiles for the case without any correction. If nothing else is mentioned, these comparisons will be done on a slice through the mid axial height of the reactor core.

The comparison of the turbulent viscosity profiles with and without curvature correction are depicted in Figure 36. With the curvature correction, as can be seen on Table 14 in the appendices, the stress at the wall is increased by a few percent, because the swirling velocity is at its maximum 10 % of the axial velocity. This causes an increase in the turbulent viscosity at the wall that is at most 4 % where the swirl is maximal. The increased value of turbulent viscosity at the wall causes a decrease of the velocity at this point, and so a small decrease of approximately 2 % for the nearby values of turbulent viscosity. The changes of viscosity in the rest of the flow are less important.

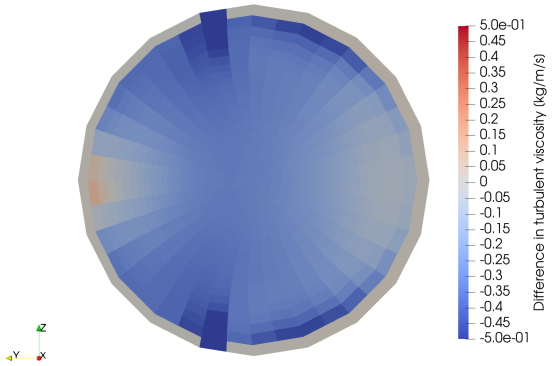

(a) Focus on the bulk values

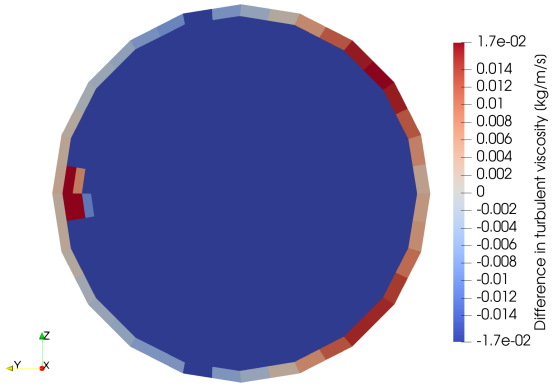

(b) Focus on the wall values

Figure 36. Comparison of the turbulent viscosity with curvature correction

The modifications of the velocity profiles due to the introduction of curvature corrections are shown in Figures 37 and 38. The increase in the turbulent viscosity at the wall causes a deceleration in every component of the velocity next to the wall. This deceleration can reach 10 % on certain points for the axial velocity, and 5 % for the swirling velocity.

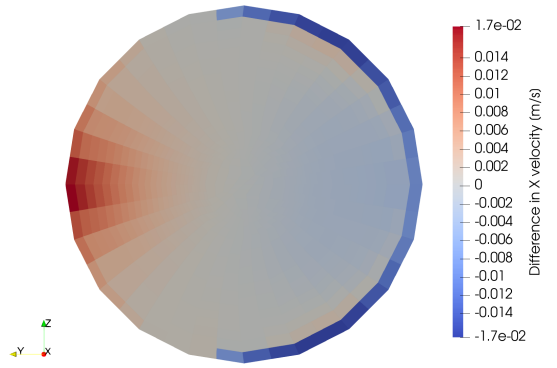

Figure 37. Comparison of the velocity along the x-axis with curvature correction

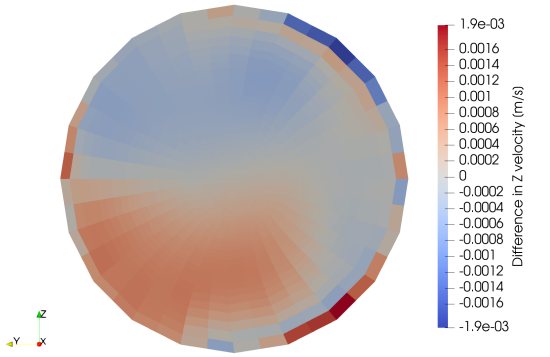

Figure 38. Comparison of the velocity along the z-axis with curvature correction

Changes in the temperature profile are correlated to changes in the velocity profile as shown in Figure 39. What this figure shows is that temperature increases where the flow decelerates, and decreases where the flow accelerates. Since the recirculation normal to the z axis is slower, the mean temperature increases, by approximately 0.05 K.

This section underlined that the interaction between swirling flows and curved walls could cause significant changes in the flow, even if the value of the swirling velocity is one order of magnitude below the one of the axial velocity, and so demonstrates the necessity to have a correction for transverse curvature.

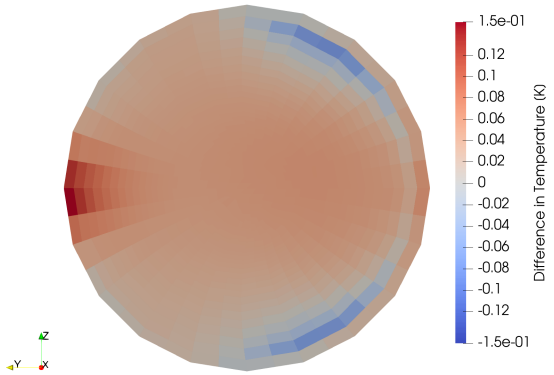

Figure 39. Comparison of the temperature profile with curvature correction

3.5.3.2. *Influence of the roughness*

For study the influence of roughness, three values for the equivalent sand grain roughness have been chosen: 10 μm, 100 μm and 1 mm. These values are of the order of magnitude that can be reached in MSRs. Note that the value of the equivalent sand grain roughness includes both the height and the shape of the roughness, e.g., an equivalent sand grain roughness of 1 mm can be done by a 125 μm height v-groove roughness according to the formulas presented in section 3.3.1.. All the comparisons displayed below will compare the different profiles for roughness corrections minus the profiles for the case with the curvature correction but without any roughness. These comparisons will either be done on a slice in the middle of the core, or on a slice located at 4/5 of the downstream length of the heat exchanger.

The first thing to observe are the changes in the value of the turbulent viscosity in the return piping system. The comparison for the turbulent viscosity profiles for different wquivalent sand grain roughness are depicted in Figures 40a, 40b and 40c. These changes observed have the same profile than the ones in the validation case: the values at the wall will be higher because of the increase in the shear stress, and the values in the middle of the pipe will be lower in order to allow the speed profile to have larger variations. These variations can be large, reaching for example 15 % at the wall and 40 % in the flow for a roughness of 1mm.

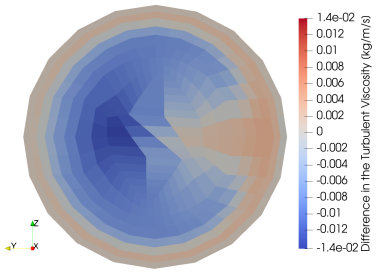

(a) $k_s = 10\ \mu m$

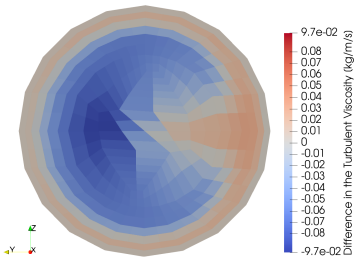

(b) $k_s = 100\ \mu m$

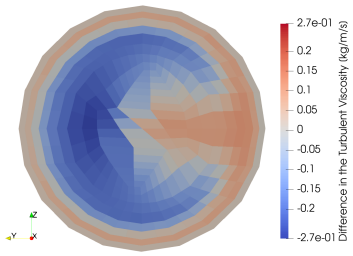

(c) $k_s = 1\ mm$

Figure 40. Comparison of the turbulent viscosity profile in the heat exchanger for different values of roughness. Note that the color scale of each plot is different.

In the heat exchanger, the velocity along the x-axis is negative, so it can be seen on figures 41a, 41b and

41c that the flow is slowed down due to the roughness. This deceleration is particularly important next to the wall, on the order of 33 % for a roughness of 1 mm, due to the increase of the turbulent viscosity, and less important in the center due to the decrease of the turbulent viscosity witnessed previously, which allows the slope of the velocity profile to be higher.

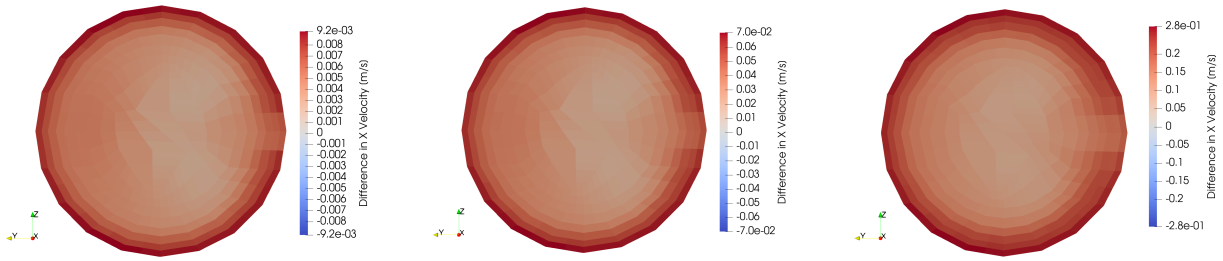

(a) $k_s = 10\ \mu m$ (b) $k_s = 100\ \mu m$ (c) $k_s = 1\ mm$

Figure 41. Comparison of the axial velocity profile in the heat exchanger for different values of roughness. Note that the color scale for each plot is different.

This decrease of the velocity in the piping system causes of the reduction of the mass flow rate. Indeed, as can be seen on table 13, the mass flow rate is a decreasing function of the equivalent sand grain roughness, with relative changes that can reach up to 15 % for a roughness of 1 mm. These changes will influence the behavior of the fluid in the core in terms of velocity and temperature. Note that this reduction in the mass flow rate is because the head of the pump is kept constant for each of the cases analyzed.

Value of k_s (μm)	Mass flow rate (kg/s)
0	20.85
10	20.74
100	20.01
1000	17.57

Table 13. Value of the mass flow rate as a function of the equivalent sand grain roughness

In the core, the effects of the roughness on both turbulent viscosity and velocity need to be studied simultaneously. Two effects are in competition:

1. the diminution of the mass flow rate will tend to decrease the mean velocity, what results in a diminution of the velocity and the stress next to the wall, which will tend to decrease the turbulent viscosity
2. the action of the roughness on the walls of the reactor will tend to increase the stress and the viscosity and decrease the velocity as what happened in the piping system

Figures 43a, 43b, and 43c show that the effect of the reduction of the mass flow rate on the viscosity is slightly more important than the direct action of the roughness. This is the reason why the turbulent viscosity decreases. The combined action of the reduction of the flow rate can be witnessed on Figures 44a to 45c, where the reduction of both axial and swirling velocities at the wall is more important than the case for which the reduction of the mass flow rate was the only change affecting the flow field. For a roughness of 1 mm, the turbulent viscosity at the wall drops by less than 10 %, while the changes in the velocity can reach 25 %.

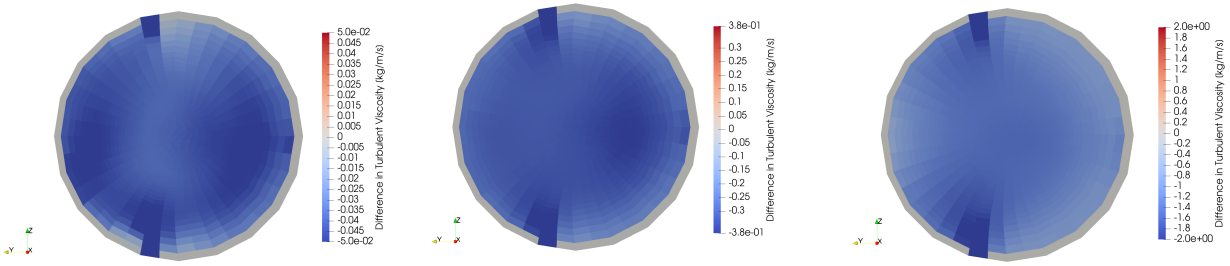

(a) $k_s = 10\ \mu m$ (b) $k_s = 100\ \mu m$ (c) $k_s = 1\ mm$

Figure 42. Comparison of the turbulent viscosity profile in the core for different values of roughness

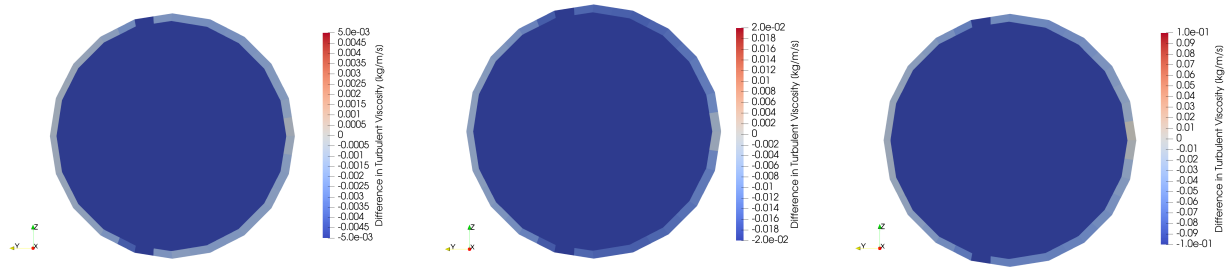

(a) $k_s = 10\ \mu m$ (b) $k_s = 100\ \mu m$ (c) $k_s = 1\ mm$

Figure 43. Comparison of the turbulent viscosity profile in the core for different values of roughness, focus on the wall

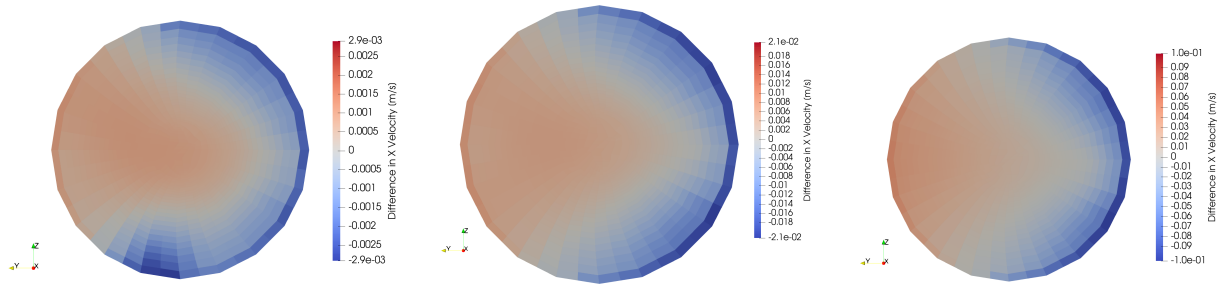

(a) $k_s = 10\ \mu m$ (b) $k_s = 100\ \mu m$ (c) $k_s = 1\ mm$

Figure 44. Comparison of the axial velocity profile in the core for different values of roughness

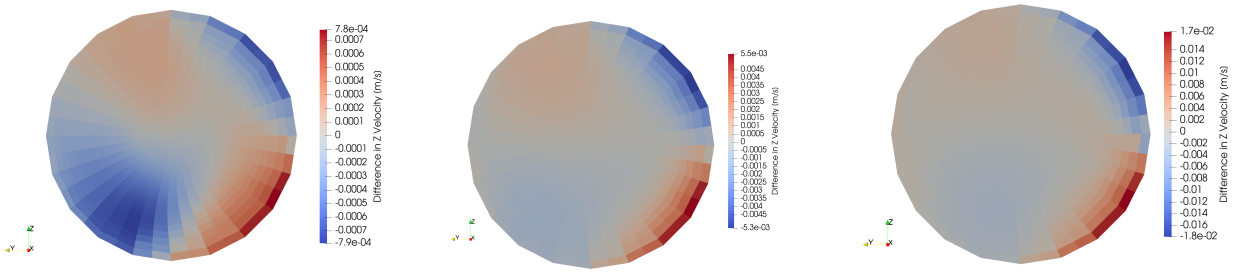

(a) $k_s = 10\ \mu m$ (b) $k_s = 100\ \mu m$ (c) $k_s = 1\ mm$

Figure 45. Comparison of one component of the swirling velocity profile in the core for different values of roughness

Finally, changes in the velocity and viscosity profiles and in the mass flow rate influence the temperature profile. Firstly, the decrease in the mass flow rate will cause an increase of the temperature in the core and a decrease in the temperature in the heat exchanger, because the fluid will need to evacuate the same amount of power with a lower mass flow rate. This can be seen especially observed on the points with a low velocity, which are those whose temperature increase the most on Figures 47a, 47b, and 47c. Secondly, the changes in the velocity profile in the heat exchanger cause the fluid close to the wall to cool even more than what is expected by only considering the changes in the mass flow rate, because the velocity close to the wall decreases more than the average, as can be seen by comparing figures 46a to 46c and figures 41a to 41c. Finally, changes in the profile of the turbulent conductivity k_t are proportional to changes in the turbulent viscosity, and so the associated reduction in this conductivity will decrease the heat transfer to the bulk of the flow.

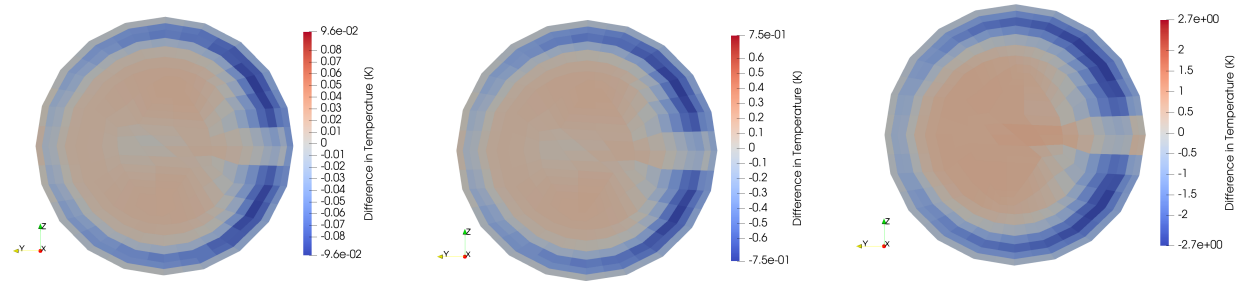

(a) $k_s = 10\ \mu m$ (b) $k_s = 100\ \mu m$ (c) $k_s = 1\ mm$

Figure 46. Comparison of the temperature profile in the heat exchanger for different values of roughness

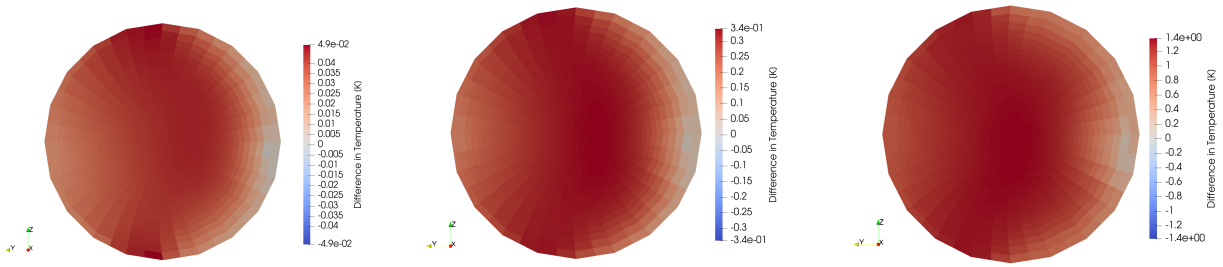

(a) $k_s = 10\ \mu$m (b) $k_s = 100\ \mu$m (c) $k_s = 1\ mm$

Figure 47. Comparison of the temperature profile in the core for different values of roughness

3.6. Conclusion

Molten Salt Reactors operate with a liquid nuclear fuel, where the power production is coupled to the thermal-hydraulics exchanges. Additionally, these reactors typically involve curved walls that aim at optimizing the flow profiles and, due to corrosive attack on structures, roughness is eventually expected to develop at these reactor walls. Using a computational thermal-hydraulics model with the standard $k-\epsilon$ model for turbulence, this article has proposed corrections to the near-wall functions due to transverse wall curvature and roughness.

The roughness correction has been validated against the Moody chart and a selected experimental case, giving close results in both situations. The curvature correction for swirling flows includes a function to calculate the wall shear stress that depends on the radius of curvature. This function has been validated for a selected experiment with swirling flows for the near wall region, using a constant blending factor for the axial and swirling velocities. Note that this function has not been calibrated, but the results show a good agreement for the velocity next to the wall according to a validation against an experimental case. A more accurate model than the standard $k-\epsilon$ model seems necessary to deal with the bulk flow far from the wall.

The developed corrections have been applied on the simulation of a Molten Salt Reactor, and underlined not only the non negligible impact that models of swirling flows could have on these reactors, but mostly the important impact that roughness could have on the mass flow rates and the heat distribution in these reactors. Close to the wall, due to curvature corrections, the amplitude of the velocity can change by approximately 2 %, even when the swirling velocity is one order of magnitude below the axial velocity. Roughness has a more significant effect, especially when it is large (1 mm for example), with changes in the mass flow rate ranging up to 15 %.

Future work will deal will deal with calibrating the curvature corrections on a larger range of swirling flows to extend their applicability beyond the presented reactor model. Additionally, the corrections will be applied to coupled multiphysics models of the L-MCR and other MSRs, to better quantify the impact that the corrections have on the reactor dynamics during transient operation.

3.7. Appendix 3A: Detail of the values in the core of the reactor for the different corrections

The profiles of the different quantities in the core are plotted here. These profiles were determined along the line described in figure 48, that was situated on the plane in the middle of the core. Table 14 references

the values at the wall on this line. The relative differences were estimated with the data at the cell marked by the cross on this figure, that is referenced in table 15. The different profiles and values obtained along this line and at the point are the following :

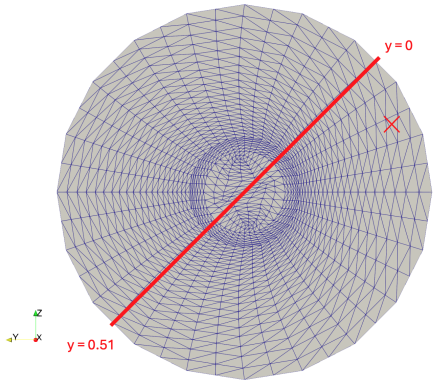

Figure 48. Line and point used for the analysis of the values in the core

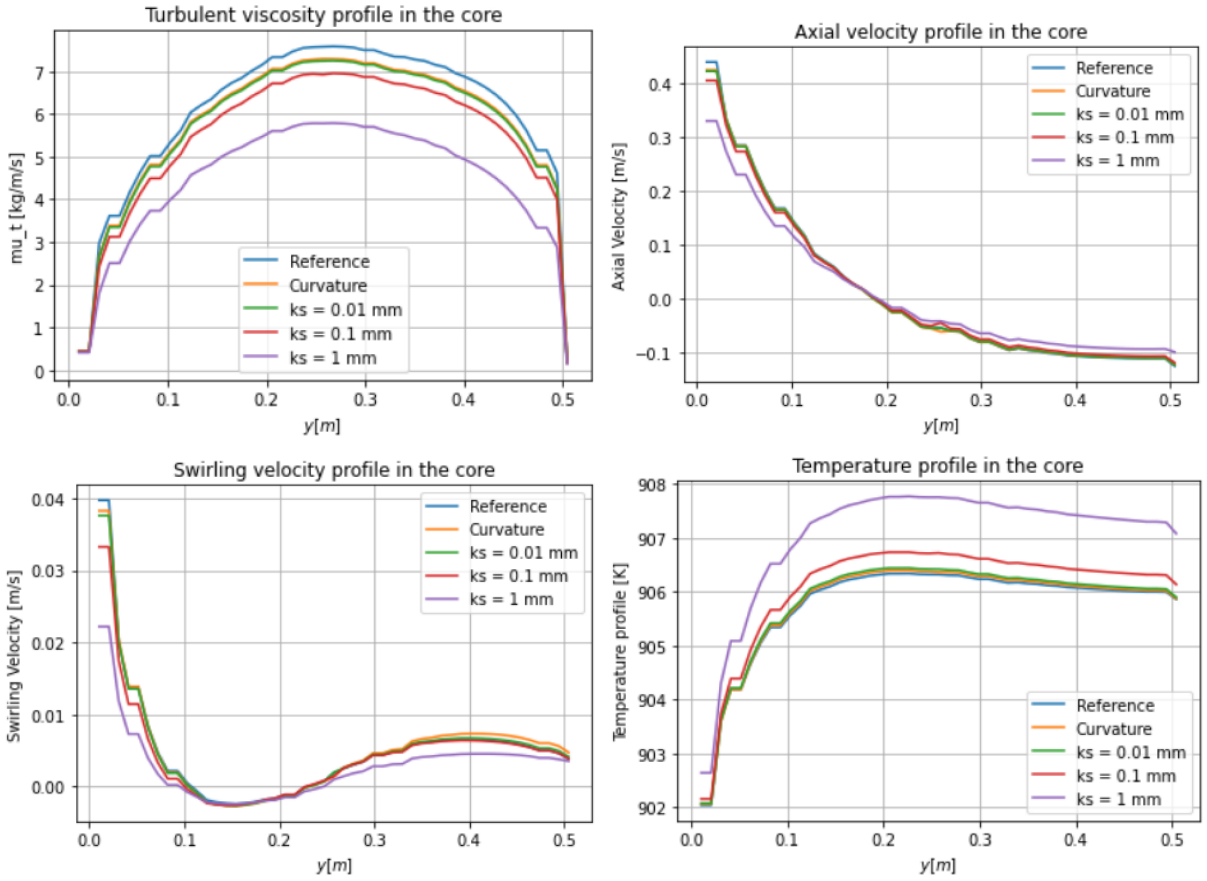

Figure 49. Profiles of the turbulent viscosity (top-left), axial velocity (top-right), swirling velocity (bottom-left), and temperature (bottom-right) in the core with the different corrections.

Quantity and wall	Reference	Curvature	ks 10 μm	ks 100 μm	ks 1 mm
μ_t for y = 0.51	0.185304	0.180869	0.17939	0.171933	0.142516
μ_t for y = 0	0.434365	0.451434	0.449529	0.438454	0.411551
V_x for y = 0.51	-0.126071	-0.12362	-0.123856	-0.119662	-0.0998047
V_x for y = 0	0.440251	0.425633	0.423202	0.405755	0.330463
V_z for y = 0.51	0.003798	0.004690	0.004110	0.003852	0.003502
V_z for y = 0	0.039761	0.0382947	0.037623	0.0332753	0.0222091
T for y = 0.51	905.865	905.874	905.9	906.139	907.083
T for y = 0	902.043	902.066	902.078	902.159	902.642

Table 14. Values at the wall for the different quantities in the core

Quantity	Reference	Curvature	ks 10 μm	ks 100 μm	ks 1 mm
μ_t	2.83	2.66	2.62	2.39	1.76
V_x	0.407	0.405	0.404	0.395	0.347
V_z	0.0183	0.0184	0.0181	0.0154	0.0082
T	902.89	902.90	902.91	903.00	903.42

Table 15. Values at the designated point for the different quantities in the core

3.8. Appendix 3B: Detail of the values in the heat exchanger of the reactor for the different corrections

The profiles of the different quantities in the heat exchanger are plotted here. These profiles were determined along the line described in figure 50, that was situated on the plane at 4/5 of the downstream length the heat exchanger. Table 16 references the values at the wall on this line. The relative differences were estimated with the data at the cell marked by the cross on this figure, that is referenced in table 17. The different profiles and values obtained along this line and at the point are the following:

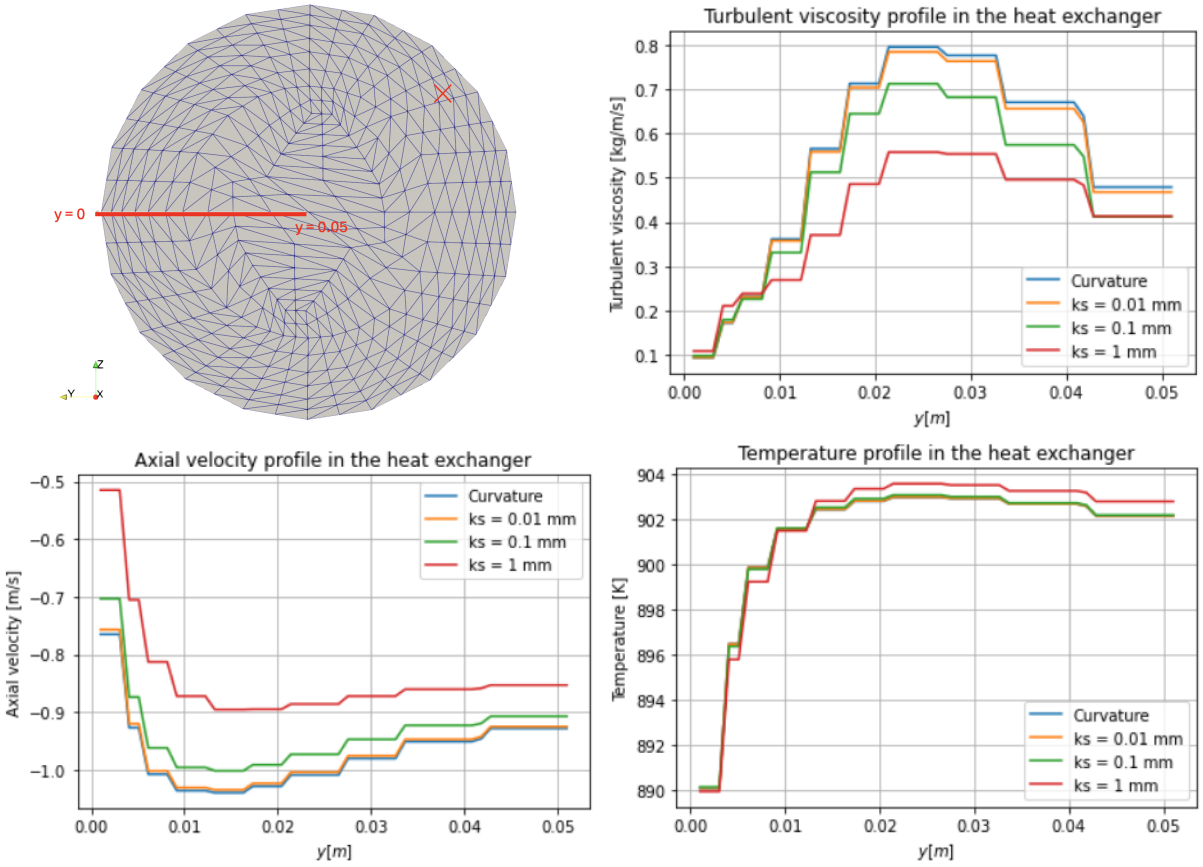

Figure 50. Top-left: line and point used for computing values at the heat exchanger. Profiles obtained for the turbulence viscosity (top-left), axial velocity (bottom-left), and temperature (bottom-right) in the heat exchanger with the different corrections.

Quantity	Curvature	ks 10 μm	ks 100 μm	ks 1 mm
μ_t	0.092783	0.093372	0.0971388	0.107818
V_x	-0.765282	-0.757277	-0.703514	-0.515065
T	890.093	890.102	890.145	889.952

Table 16. Values at the wall for the different quantities in the heat exchanger

Quantity	Curvature	ks 10 μm	ks 100 μm	ks 1 mm
μ_t	0.164	0.165	0.179	0.260
V_x	-0.957	-0.951	-0.908	-0.742
T	898.59	898.50	897.87	895.85

Table 17. Values at the designated point for the different quantities in the heat exchanger

4. DEVELOPMENT AND VALIDATION OF TWO-PHASE FLOW MODELS IN MOOSE FOR SUPPORTING TWO-PHASE FLOW STEADY AND TRANSIENT SIMULATIONS IN MOLTEN SALT REACTORS

This section reproduces a journal article that, as a part of this milestone, has been submitted to Nuclear Engineering and Design in August 2024.

4.1. Introduction

MSRs are a class of advanced nuclear reactors that use a liquid molten salts as both fuel and coolant. This unique configuration offers several advantages, including enhanced safety through inherent negative temperature coefficients due to mixed Doppler/density effects and possibility of long term cooling with natural convection of the fuel, high thermal efficiency due to elevated operating temperatures, and the ability to consume various nuclear fuels, including thorium. Additionally, MSRs offer significant benefits in fuel cycle efficiency and waste reduction, positioning them as suitable candidates for future sustainable nuclear energy production [39–43].

In MSRs, the formation of gaseous phases can occur due to multiple reasons. The reason addressed in this work is the production a gaseous phase, such as xenon and krypton, through the volatilization of fission gases during the nuclear fission process [44, 45]. Other sources of gas in the reactor can include gas sparging techniques used for removing fission products and the potential entrainment of cover gas [39, 46–48].

The accumulation of these gases can significantly affect the operation of MSRs. The presence of gas bubbles leads to a reduction in the liquid fuel density, which in turn can impact the reactor's reactivity, leading to power fluctuations and uncertainties in critical configuration of the reactor during its design and engineering [49–51]. Furthermore, the localized accumulation of gases can alter the temperature fields within the reactor, potentially creating hot spots or influencing the overall heat transfer efficiency [52–54]. Additionally, the buildup of void in the reactor head poses a risk of pressure fluctuations that could affect the flow through the core and the mixing profiles in the fuel salt [55, 56]. Therefore, accurately modeling the transport and distribution of void fractions within the MSRis crucial for ensuring stable and safe reactor operation.

Previous research on the impact of void formation in MSRs has predominantly focused on simplified models and specific case studies [57–59]. Early studies often employed one-dimensional models to analyze the basic effects of void accumulation on reactivity and temperature profiles [60, 61]. More recent work has introduced two-dimensional and three-dimensional models, which offer better spatial resolution and can capture more complex flow dynamics [8, 62, 63]. Notably, the work by Cervi et al. [44] laid the groundwork for understanding the behavior of fission gas bubbles in molten salts, while similar studies [64, 65] also worked in exploring the interaction between gas voids and reactor thermal-hydraulics. Despite these advancements, there remains a need for a more integrated approach that couples void fraction transport with multiphysics simulations, including neutronics and thermal-hydraulics [66–68].

This work improves upon previous studies by introducing a comprehensive two-phase flow model within the MOOSE [66]. Unlike earlier models, this approach integrates a multidimensional drift-flux formulation with an interface area concentration model, providing a more detailed and accurate representation of gas transport in MSRs. The model is validated against experimental data and applied to a real-world scenario using the MSRE as a case study. This study offers novel insights into the impact of void fraction on reactor behavior, emphasizing the importance of three-dimensional modeling in capturing the operation of MSRs [8, 69].

The rest of this article is organized as follows: Section 4.2. introduces the fundamental equations and modeling approach used in this study. Section 4.3.2. discusses the verification and validation of the model against experimental data. In Section 4.4., the model is applied to the MSRE to study the impact of void fraction on reactor operation. Finally, Sections 4.5. and 4.6. provide recommendations for two-phase modeling in MSRs and conclude the findings of this study.

4.2. Modeling approach

This section is organized as follows. First, the two-phase Naiver Stokes and energy conservation equations describing the fluid flow phenomena in MSRs are reviewed. Then, the two-phase flow model with drift-flux is introduced. Finally, the closure model for interface area concentration is reviewed.

4.2.1. Single-phase porous media thermal-hydraulics modeling

The equations solved for thermal-hydraulics modeling in MOOSE are the two-phase mixture Navier Stokes and energy conservation equations in porous media. However, for ease of introduction, in this section we review the porous media equations in for a single phase flow, while in the next section we address the modifications in these equations for dealing with two-phase flow.

The porous media formulation assumes that the liquid fuel and the internal reactor structures occupy the same homogenized volume. The fluid volume fraction is referred to as the porosity of the shared volume. In mathematical terms, the porosity of an assembly is defined as follows:

$$\gamma = \frac{V_f}{V_T}, \tag{55}$$

where V_f is the flow volume and V_T is the total volume. This porous formulation is typically used for the reactor core and plena, while the rest of the domain is typically modeled as free flow. Note that the porosity, γ, which is used to define the fluid volume of the porous structure which is different than the void fraction, α, which will be used to denote the dispersed phase in the multiphase fluid.

Balance equations for fluid mass, momentum, energy, and solid energy are coupled via momentum and energy exchanges described by correlations. One advantage of this approach is the ability to seamlessly couple porous flow regions to free-flow regions outside of the immediate core regions without changing the modeling paradigm. The porous flow equations for weakly-compressible flow are given by:

$$\begin{aligned}
\frac{\partial \gamma\rho}{\partial t} + \nabla\cdot(\rho\mathbf{u}) &= 0 \quad \text{on } \Omega_f, \\
\frac{\partial \rho\mathbf{u}}{\partial t} + \nabla\cdot\left(\gamma^{-1}\rho\mathbf{u}\otimes\mathbf{u}\right) - \nabla\cdot\left[(\mu+\rho\nu_t)(\nabla\mathbf{u}+\nabla\mathbf{u}^T)\right] &= \\
-\gamma\nabla p + \gamma\rho\mathbf{g} - W\rho\mathbf{u}_I + \mathbf{S} \quad \text{on } \Omega_f, & \\
\frac{\partial \gamma\rho e}{\partial t} + \nabla\cdot(\rho e\mathbf{u}) - \nabla\cdot\left(\kappa_f\nabla T\right) - \nabla\cdot(\rho\alpha_t\nabla e) + h_V(T-T_s) &= \dot{q}_l''' \quad \text{on } \Omega_f, \\
(1-\gamma)\rho_s c_{p,s}\frac{\partial T_s}{\partial t} - \nabla\cdot(\kappa_s\nabla T_s) - h_V(T-T_s) &= \dot{q}_s''' \quad \text{on } \Omega_s,
\end{aligned} \tag{56}$$

where $\mathbf{u}$ is the superficial velocity defined as $\mathbf{u} = \gamma\mathbf{u}_I$, with γ as the porosity and $\mathbf{u}_I$ as the interstitial or physical velocity, ρ is the density, p is the pressure, e is the internal energy, T is the fluid temperature, T_s is the solid temperature, ρ_s is the solid density, $c_{p,s}$ is the specific heat of the solid phase, $\mathbf{g}$ is the gravity vector,

W is the pressure drop coefficient, $\mathbf{S}$ is the momentum source that is usually used to model the pump, κ_f is the effective thermal conductivity of the fluid, α_t is the turbulent heat diffusivity, κ_s is the effective solid thermal conductivity, h_V is the volumetric heat exchange coefficient between the liquid and solid phases, $\dot{q}_l'''$ is the heat source being deposited directly in liquid fuel (e.g., fission heat source), and $\dot{q}_s'''$ is the heat source in the solid (e.g., residual power production in structures). For an assembly modeled as a porous medium, the fission source is defined as the total power of the assembly divided by its total volume. The effective thermal conductivities κ_f and κ_s are in general diagonal tensors.

The fluid domain Ω_f comprises porous regions with $0 < \gamma < 1$ and free flow regions with $\gamma = 1$; in the free-flow region, T_s is not solved, $\alpha = 0$, $W = 0$, and $\kappa_f = k_f$ (where k_f is the thermal conductivity of the fluid). Similarly, T_f is not solved in solid-only regions where $\gamma = 0$ and $\kappa_s = k_s$ with k_s as the solid conductivity.

To close the equation system, the turbulence quantities ν_t and α_t need to be modeled. This is done in this case via a capped mixing length model, where the turbulent viscosity is defined as:

$$\nu_t = \ell_m ||\nabla \mathbf{u}|| \,, \tag{57}$$

where ℓ_m is the mixing length. Additionally, the mixing length model is capped regarding the distance of the computational cell to the wall y as follows:

$$\ell_m = \begin{cases} \kappa y, & \text{if } \frac{y}{\delta} \leq \frac{\kappa_0}{\kappa} \,, \\ \kappa_0 \delta, & \text{if} \frac{y}{\delta} > \frac{\kappa_0}{\kappa} \,, \end{cases} \tag{58}$$

where $\kappa = 0.41$ is the Kolmogorov constant and $\kappa_0 = 0.09$ is the Escudier capping constant. Furthermore, δ is a capping distance that is tuned to reproduce the results of higher fidelity models.

This section has introduced the porous media formulation in for one phase flow. The next section explains the modifications implemented in this model for dealing with two-phase flow.

4.2.2. Multidimensional porous-media two-phase drift-flux model

The fundamental idea of the two-phase drift-flux model is to treat the fluid mixture as a single entity rather than as separate phases. By employing constitutive assumptions, it simplifies the local behavior of each phase and the interfacial interactions. Although this approach overlooks some critical aspects of two-phase flow, the model's simplicity makes it highly valuable for many engineering applications. In the analysis of two-phase flow system dynamics, the focus is often on the response of the entire mixture rather than each individual phase. In the planning and designing of two-phase flow experiments and engineering systems, its simplicity allows effective scaling between different systems with the drift-flux model formulation and mixture properties. The drift-flux model implemented in MOOSE includes a separate equation for the dispersed phase continuity and the linear momentum and energy conservation in the fluid phase are modified by mixing homogenization and by adding the drift flux from the dispersed phase. Additionally, the model adds a closure correction for the drift-flux [70].

The set of modified equations for two-phase flow in a porous media reads as follows:

$$
\begin{aligned}
\frac{\partial \gamma \rho_d}{\partial t} + \nabla \cdot (\rho_d \mathbf{u}_d) &= \Gamma_d \quad \text{on } \Omega_f\,, \\
\frac{\partial \gamma \rho_m}{\partial t} + \nabla \cdot (\rho_m \mathbf{u}_m) &= 0 \quad \text{on } \Omega_f\,, \\
\frac{\partial \rho_m \mathbf{u}_m}{\partial t} + \nabla \cdot \left(\gamma^{-1} \rho_m \mathbf{u}_m \otimes \mathbf{u}_m\right) - \nabla \cdot \left[(\mu_m + \rho_m \nu_t)(\nabla \mathbf{u}_m + \nabla \mathbf{u}_m^T)\right] &= \\
-\gamma \nabla p_m + \gamma \rho_m \mathbf{g} - W \rho_m \mathbf{u}_{I,m} + \mathbf{S} - \nabla \cdot \left(\gamma^{-1} \alpha \rho_d \mathbf{u}_{slip,d} \otimes \mathbf{u}_{slip,d}\right) &\quad \text{on } \Omega_f\,, \\
\frac{\partial \gamma \rho_m e_m}{\partial t} + \nabla \cdot \left(\rho_m e_m \mathbf{u}_m + q_p\right) - \nabla \cdot \left(\kappa_{f,m} \nabla T\right) - \nabla \cdot \left(\rho_m \alpha_t \nabla e_m\right) + h_V (T - T_s) &= \dot{q}_l{}''' \quad \text{on } \Omega_f\,, \\
(1-\gamma) \rho_s c_{p,s} \frac{\partial T_s}{\partial t} - \nabla \cdot (\kappa_s \nabla T_s) - h_V (T - T_s) &= \dot{q}_s{}''' \quad \text{on } \Omega_s.
\end{aligned}
\tag{59}
$$

These equations describe, in order, mass conservation for the dispersed phase, mass conservation for the fluid mixture, linear momentum conservation for the fluid mixture, energy conservation for the fluid mixture, and energy conservation for the solid. The current model assumes thermal balance between the liquid and gas phases, i.e., the liquid and gas phases are assumed to be at the same temperature. The notations used in the equations are listed below:

$\mathbf{u}_m$ is the superficial mixture velocity field, defined as $\mathbf{u}_m = \gamma \mathbf{u}_{I,m}$

$\mathbf{u}_d$ is the superficial velocity field of the dispersed phase, defined as $\mathbf{u}_d = \gamma \mathbf{u}_{I,d}$

Γ_d is the volumetric exchange between two phases,

p_m is the pressure field of the mixture fluid,

α is the volume fraction of the dispersed phase, e.g., the gas bubbles in liquid gas mixture,

ρ_m is the mixture fluid density, defined as $\rho_m = (1-\alpha)\,\rho_c + \alpha \rho_d$,

ρ_d is the density of the dispersed phase,

μ_m is the mixture dynamic viscosity, defined as $\mu_m = (1-\alpha)\mu_c + \alpha \mu_d$,

$\mathbf{u}_{slip,d}$ is the slip velocity,

e_m is the mixture mass-specific internal energy, defined as $e_m = (1-\alpha)e_c + \alpha e_d$,

$q_p = \sum_{k=1}^{2} \alpha_k \rho_k e_k \mathbf{u}_k$ is the interfacial momentum-energy transfer term, where α_k is the void fraction of the liquid or gas phase, ρ_k is the density of each phase, e_k is the energy of each phase, which is assumed to be the mixture energy in our model, and $\mathbf{u}_k$ is the phase-specific slip velocity, which is computed as $\mathbf{u}_d$ for the gas phase and $\mathbf{u}_m - \mathbf{u}_d$ for the liquid one.

The mixture fluid properties are defined as the volume-average of the two phase:

$$
p_m = (1-\alpha)\, p_c + \alpha p_d, \tag{60}
$$

where p represents ρ, μ, c denoted continuous phase while d denoted dispersed phase. The mixture velocity is defined as the weighted average velocity of the two phases:

$$\mathbf{u}_m = \frac{\alpha\rho_d\mathbf{u}_d + (1-\alpha)\,\rho_c\mathbf{u}_c}{\rho_m}, \tag{61}$$

Given the definition of the dispersed phase drift velocity as

$$\mathbf{u}_{drift,d} = (1-\alpha_d)\,(\mathbf{u}_d - \mathbf{u}_c) \tag{62}$$

We can derived the velocity of the dispersed phase as a function of mixture velocity $\mathbf{u}_m$ and the slip velocity $\mathbf{u}_{slip,d}$:

$$\mathbf{u}_d = \mathbf{u}_m + \frac{\rho_c}{\rho_m}\mathbf{u}_{slip,d}, \tag{63}$$

Then the continuity equation for the dispersed phase can be expressed as:

$$\frac{\partial\rho_d}{\partial t} + \nabla\cdot(\rho_d\mathbf{u}_\mathbf{d}) = \Gamma_d - \nabla\cdot\left(\frac{\alpha\rho_c\rho_d}{\rho_m}\mathbf{u}_{slip,d}\right) \tag{64}$$

The slip velocity is modeled as

$$\mathbf{u}_{slip,d} = \frac{\tau_d}{f_{drag}}\frac{\rho_d-\rho_m}{\rho_d}\mathbf{a} \tag{65}$$

where τ_d is the particle relaxation time, $f_{drag}$is the linear drag coefficient function, and $\mathbf{a}$ is the acceleration vector.

The particle relaxation time is estimated using Bilicki & Kestin's model[71]:

$$\tau_d = \frac{\rho_d d_d^2}{18\mu_m} \tag{66}$$

where the particle diameter is represented as d_d.

The acceleration vector has contributions from gravity ($\mathbf{g}$), volumetric force($\mathbf{f}$) and mixture velocity($\mathbf{u}_m$),

$$\mathbf{a} = \mathbf{g} + \frac{\mathbf{f}}{\rho_m} - \mathbf{u}_m\cdot\nabla\mathbf{u}_m - \frac{\partial\mathbf{u}_m}{\partial t} \tag{67}$$

4.2.3. Interface area concentration

The mixture model with homogenization approach could describe the interfacial exchanging process. For example, when two control volume have the same void fraction, α, there may still be a different total interface between the liquid and the gas phases. Therefore, an interfacial area transport model is implemented to decribe the axial interfacial exchanging process in two-phase flow. The interfacial area concentration is defined as the interface area between two phases per unit volume, i.e.,$[\xi_p] = \frac{m^2}{m^3}$. This parameter is important for predicting mass, momentum, and energy transfer at interfaces in two-phase flows.

The general equation for interfacial area concentration transport via the mixture model is written as follows:

$$\frac{\partial(\rho_d\xi_p)}{\partial t} + \nabla\cdot\left(\gamma^{-1}\rho_d\mathbf{u}_m\xi_p\right) - \nabla\left(D_b\nabla\xi_p\right) = -\frac{1}{3}\frac{D\rho_d}{Dt} + S_T + \rho_d(S_C + S_B) \tag{68}$$

where D_b is a diffusion coefficient for the interface area concentration, which may be assumed to be '0' if unknown, $\frac{D(\bullet)}{Dt} = \frac{\partial(\bullet)}{\partial t} + \mathbf{u} \cdot \nabla(\bullet)$ is the material derivative, S_T, S_C, and S_B are the interface area concentration sources due to mass transfer, coalescence, and breakage, respectively. These source terms are modeled using a multidimensional version of Hibiki and Ishii's model([7]). The interface area concentration source due to mass transfer is modeled in Eq.69. Since the mass transfer term in Hibiki and Ishii's model is not physical at low volumetric fractions of the dispersed phase. A cutoff volumetric fraction α_d^{co} is introduced assuming bubbly flow regime. The dispersed phase is modeled as spherical particles below the cutoff limit.

$$S_T = \begin{cases} \frac{6\alpha_d}{d_p}, & \text{if } \alpha_d < \alpha_d^{co} \\ \frac{2}{3} \cdot h^{b \to d} \left(\frac{1}{\alpha_d} - 2.0 \right), & \text{otherwise} \end{cases}, \tag{69}$$

where:

α_d is the volumetric fraction of the dispersed phase, e.g., the void fraction if the dispersed phase is a gas,

α_d^{co} is a cutoff fraction for mass transfer model selection,

d_p is the best estimate for the dispersed phase particle diameter,

$h^{b \to d}$ is the mass exchange coefficient from the bulk to the dispersed phase.

The dispersed phase coalescence is considered to occur due to the bubble random collision induced by turbulence in a liquid phase. The reduction in interface area concentration due to coalescence of the dispersed phase is modeled as follows:

$$S_C = -\left(\frac{\alpha_d}{\tilde{\zeta}_p} \right)^2 \frac{\Gamma_C \alpha_d^2 u_\epsilon}{\tilde{d_p}^{11/3} (\alpha_d^{max} - \alpha_d)} \exp\left(-K_C \frac{\tilde{d_p}^{5/3} \rho_b^{1/2} u_\epsilon^{1/3}}{\sigma^{1/2}} \right), \tag{70}$$

where:

u_ϵ is the friction velocity due to pressure gradients which is defined as $u_\epsilon = \left(\|\mathbf{u}\| \ell \|\nabla p\| / \rho_m \right)^{1/3}$, with $\|\mathbf{u}\|$ being the norm of the velocity vector, ℓ a characteristic mixing length, $\|\nabla p\|$ the norm of the pressure gradient, and ρ_m the mixture density,

$\tilde{d_p}$ is the model estimate for the dispersed phase particle diameter defined as $\tilde{d_p} = \psi \frac{\alpha_d}{\tilde{\zeta}_p}$, with ψ being a shape factor, which is, for example, $\psi = 6$ for spherical particles,

α_d^{max} is the maximum volumetric fraction admitted by the model, in absence of data we recommend taking $\alpha_d^{max} = 1$,

ρ_b is the bulk phase density, e.g., for air bubbles in a water flow it would be the density of water,

σ is the surface tension between the two phases,

Γ_C, K_C are closure coefficients of the model which defined as 0.188 and 0.129, correspondingly.

The dispersed phase breakup is considered to occur due to the collision of the turbulent eddy with the bubble. The increase in interface area concentration due to breakage of the dispersed phase is modeled as follows:

$$S_B = \left(\frac{\alpha_d}{\zeta_p}\right)^2 \frac{\Gamma_B \alpha_d (1-\alpha_d) u_\epsilon}{\tilde{d_p}^{11/3}(\alpha_d^{max} - \alpha_d)} \exp\left(-K_B \frac{\sigma}{\rho_b \tilde{d_p}^{5/3} u_\epsilon^{2/3}}\right), \tag{71}$$

where the same set of variables are used as Eq.70, but the closure coefficients of the model are set to $\Gamma_B = 0.264$ and $K_B = 1.370$.

4.3. Model verification and validation

4.3.1. Model verification and order of convergence analyses

The model verification is performed for the two-phase drift flux model implementation in MOOSE. The major transient terms are examined to ensure the code converges to the correct solution when a manufactured solution is given. The convergence analyses are also performed for each test case to ensure the observed accuracy of the numerical approach agrees with the expected formal order of accuracy. The accuracy of the solution is quantified using the l_2-norm defined as:

$$l_2 = \sqrt{e_1^2 + e_2^2 + \cdots + e_n^2} \tag{72}$$

where e is the error vector between the code and the expected solution. A series of MOOSE simulation are performed with time refinements including mass transient and momentum transient.

The same set of mass transient and momentum problems tested for SAM drift flux model[72] is used for model verification. A 2D $1m$ horizontal tube with no friction is used for mass transient test. The model inputs are the mixture velocity and the void fraction of the gas phase (dispersed phase). For the mixture velocity, a constant velocity boundary condition is set for the inlet on the left side of the channel as $1m/s$ and an outflow boundary condition on the right side of it. Non-slip wall condition is applied to the rest boundaries. For the void fraction, a time-varying volume fraction (Eq. 73) is applied to the inlet resulting in a sinusoidal shape varying gas phase into the domain. The phase densities are set to be $1,000$ and $1kg/m^3$ for liquid and gas accordingly. The average void fraction at outlet is estimated and compared with analytical solution shown in Figure. 51. The convergence analysis is performed for three different constant time step sizes $dt = 0.1s, 0.025s$ and $0.0125s$. The log-log plot of the time step size versus the l_2 error reveals the convergence order. Since the second-order backward differentiation formula (BDF2) is employed as the time integration scheme, the error decreases following a second-order slope as the time step size is reduced(Figure. 52).

$$\alpha(t) = 0.05\,(sin\,(2\pi t - \pi/2) + 1) \tag{73}$$

The same geometrical setup is used for momentum transient test case. The fluid behaviour is expressed using an analytical solution so that the time dependent momentum can be predicted and compared with analytical expression. For the pressure, a transient sinusoidal function boundary condition (Eq.74) is applied at the inlet while a fixed value boundary condition for the outlet.

$$P_i(t) = 1560 sin\,(\pi t) + P_0 \tag{74}$$

P_i is the inlet pressure while P_0 is the outlet pressure fixed at $1bar$. The initial and the inlet void is set to be constant. Given the relation between pressure and velocity, one can derive the expression of velocity and applied it as the inlet boundary condition for the mixture velocity:

$$v(t) = 1.992 - 0.9921 cos\,(\pi t) \tag{75}$$

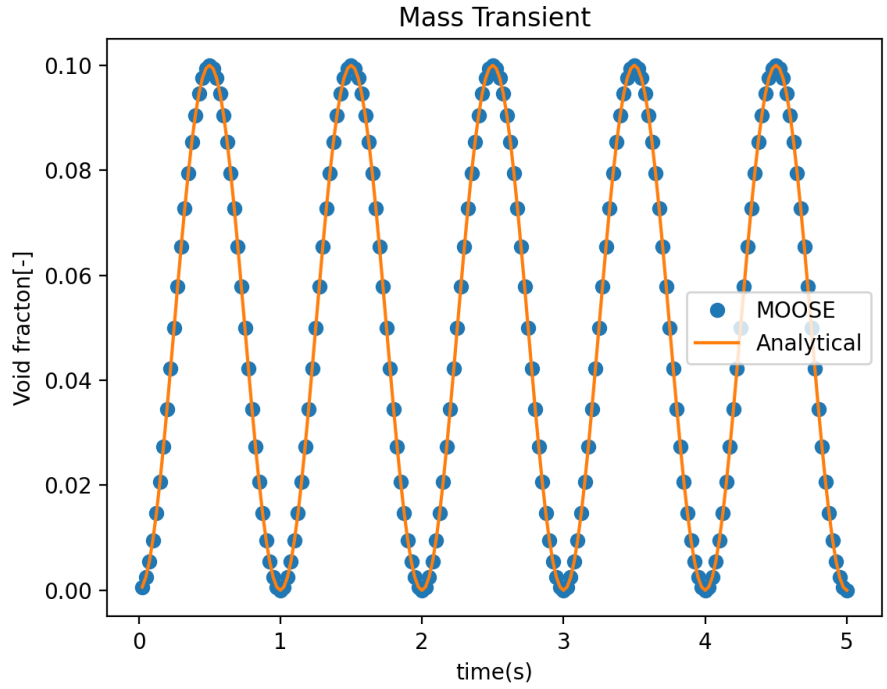

Figure 51. Comparison of Analytical and Simulation Mass Transient in 2D Channel.

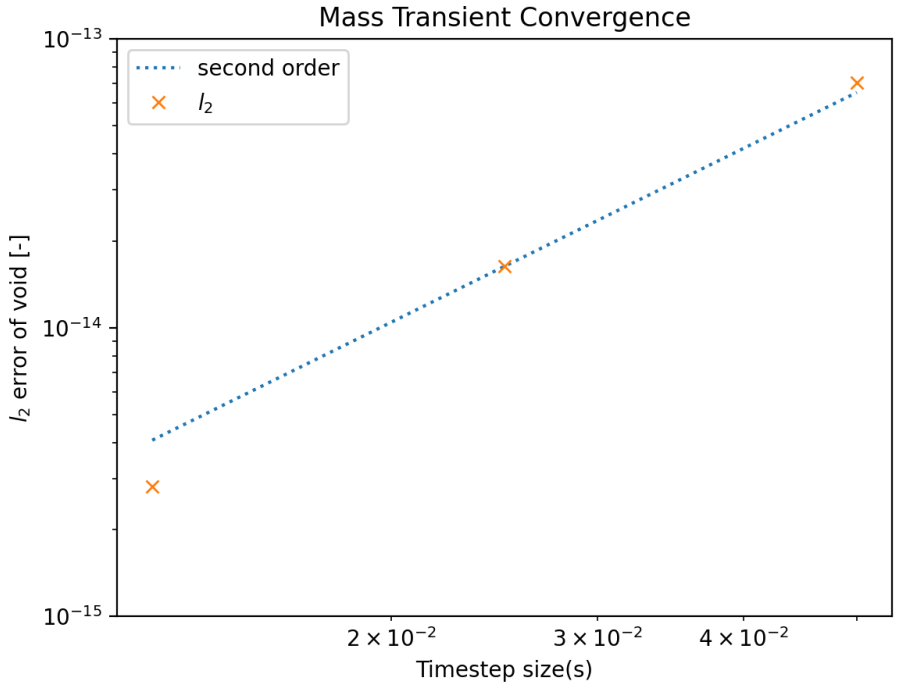

Figure 52. The Convergence Analysis of Mass Transient Simulation in 2D Channel.

The average mixture velocity at the inlet is collected and compared with analytical velocity profile shown in Figure.53 for time step size $dt = 0.0125s$. The simulated results agree well with the analytical solution. For the convergence analysis of the transient momentum term, the implicit backwards Euler is used as time integration scheme. The l_2 error v.s. time step size are shown in Figure. 54. The implicit backwards Euler is a first-order time scheme so as the time step size decreases, the l_2 error is expected to decrease linearly with a slope equal to one. For $dt = 0.0125s$ and $dt = 0.00625s$, the l_2 error agrees well with the first order line and for $dt = 0.05s$, the l_2 error is smaller than the first-order line projection which may come from other embedded optimization in MOOSE solver.

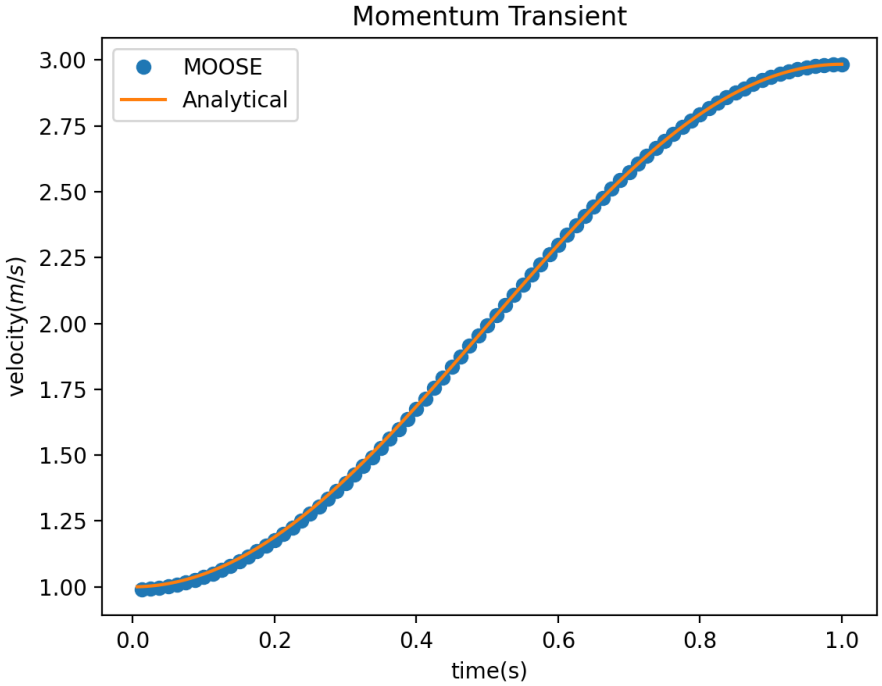

Figure 53. Comparison of Analytical and Simulation Momentum Transient in 2D Channel.

4.3.2. Validation of the drift-flux model

The validation of the drift-flux model is carried out using two sets of experimental data: Hibiki (2001) [73] and Bhagwat (2016) [69]. A wide range of void fractions is covered to ensure comprehensive validation of the simulation results. The experiments are conducted in an upward tube geometry with air/water flow. Since these two-phase experiments use air and water fluids, evaporation and condensation are not considered and the air phase lateral distribution flow is expected to reach a steady-state condition. The drift flux model mainly the advection terms are validated against the experimental data. The axial interfacial area distribution is neglected due to the homogenization assumption of the drift flux model. It will be modeled with an interfacial area concentration model and validated separately in section 4.2.3.. The simulations conducted in this section will focus on the advection of two-phase flow, using the outlet gas velocity as the key quantity of interest against the experimental results.

Hibiki et al.[73] measures the superficial liquid velocity ranged from 0.491 to $5.00 m/s$ and void fraction ranged from 4.90% to 44.2%. The local flow measurements of vertical upward air-water flows in a round tube

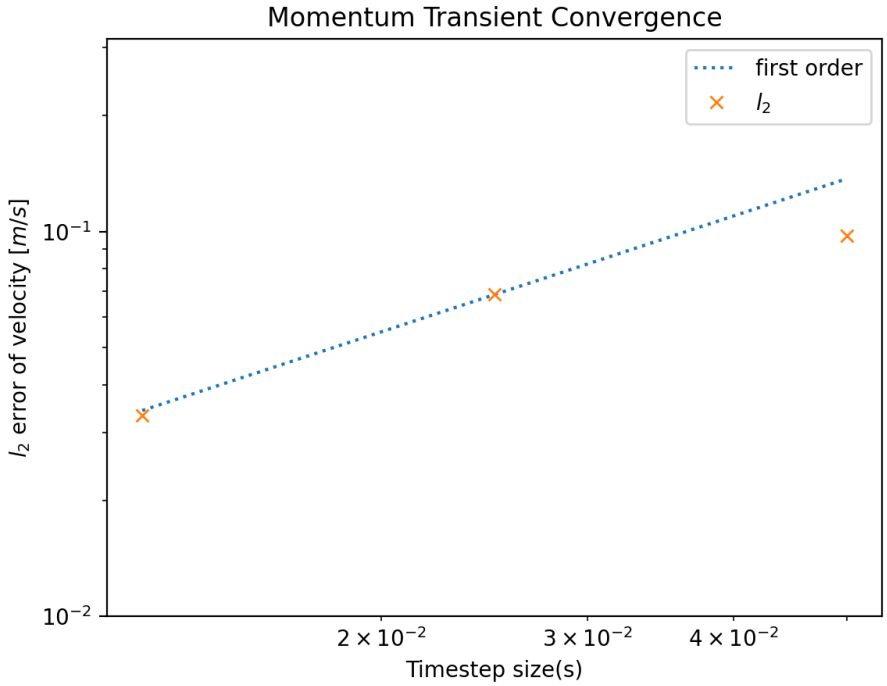

Figure 54. The Convergence Analysis of Momentum Transient Simulation in 2D Channel.

with an inner diameter of 50.8mm were performed at three axial location of $z/D = 6.00$, $z/D = 30.3$ and $z/D = 53.5$. In the simulations, we use a cartesian, 2D, axi-symmetric domain for the tube geometry. The mixture velocity and the void fraction are selected as the inputs of the drift flux model. The outlet gas velocity is selected as the quantities of interest to compare with the experiment measurement at location $z/D = 53.5$. Given the measured superficial phase velocity and void fraction, we can estimate the mixture velocity using 61. Meanwhile, the slip velocity can be expressed in term of experiment-measured superficial velocities and void fraction in Eq. 76. Therefore, one can further estimate the simulated gas velocity at $z/D = 53.5$ with Eq.63. Three different flow conditions are selected for comparison in Table 18. The simulated gas velocities agree well with experimental measurement as shown in Figure. 55.

$$\mathbf{u}_{slip,d} = \frac{\langle j_g \rangle}{\langle \alpha \rangle} - \left(\langle j_g \rangle + \langle j_f \rangle \right) \tag{76}$$

Void Fraction	$J_f(m/s)$	$J_g(m/s)$	$v_{slip}(m/s)$	$v_m(m/s)$
0.049	0.491	0.0275	0.043	0.56
0.092	0.491	0.0556	0.058	0.58
0.192	0.491	0.129	0.052	0.57

Table 18. The Experimental Velocity Data of Hibiki 2001 for Low Void Fractions Scenarios

Bhagwat et al. [69] conducts experiments of non-boiling gas-liquid two phase flow for various upward inclined pipes.They measures flow visualization, void fraction, pressure drop and heat transfer in 12.7mm I.D. polycarbonate pipe using air-water as fluid combination. The gas and liquid phase mass flow rates vary

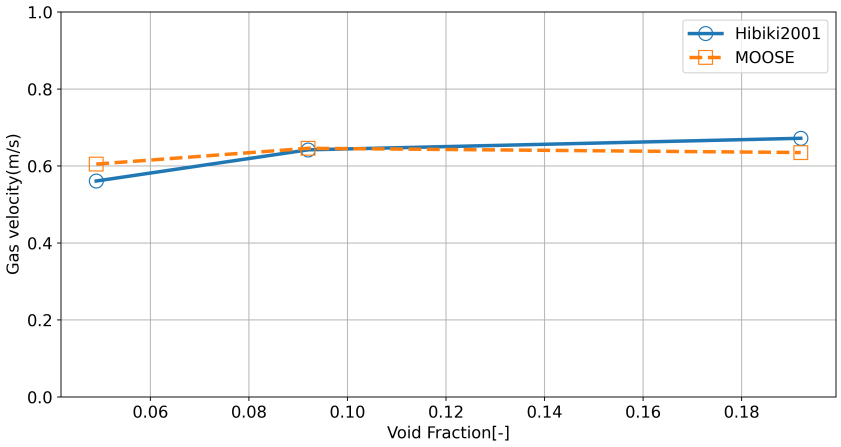

Figure 55. Comparison of Simulation and Experimental Gas Velocity at the Outlet for Low Void Fraction Scenarios.

in a range of $0.0010.2kg/min$ and $110kg/min$, respectively. To validate the drift model, we use the mixture velocity and the void fraction as model inputs and compare the gas velocity at the outlet against experimental data. A cartesian, 2D, axi-symmetric domain is used to simulate the tube geometry. Four experimental data sets with void fraction range from 0.455 to 0.6 are selected as reference in table 19.The averaged gas velocities from the MOOSE simulations are collected at the outlet and compare against the experimental data shown in 56.

Void Fraction	$v_f(m/s)$	$v_g(m/s)$	$v_{slip}(m/s)$	$v_m(m/s)$
0.455	0.15	0.21	0.03	0.15
0.475	0.45	0.58	0.07	0.45
0.55	0.15	0.42	0.12	0.15
0.6	0.15	0.65	0.20	0.15

Table 19. The Experimental Velocity Data of Bhagwat 2016 for High Void Fractions Scenarios

4.3.3. Validation of the interface area concentration model

The interfacial area transport model is implemented to describe the axial interfacial exchanging process in two-phase flow. The validation of the interface area concentration model is performed against the experiments performed by Hibiki and Ishii [7]. In these experiments air bubbles were injected in a water flow in pipes at varying superficial liquid and gas velocity. All experiments were performed on pipes with 50.8mm of diameter. The main parameters for the experimental setup for the cases analyzed are detailed in Table 20. The experiments are designed to test increase and decrease in interfacial area concentration due to pressure gradients, bubble random collision, and turbulent breakup.

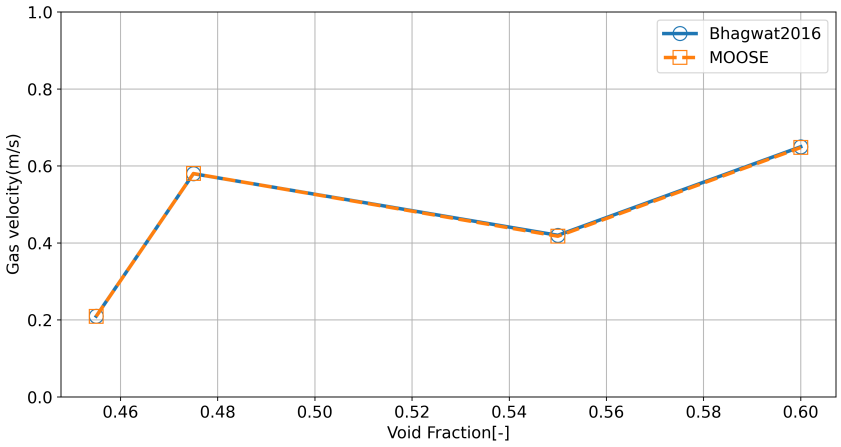

Figure 56. Comparison of Simulation and Experimental Gas Velocity at the Outlet for High Void Fraction Scenarios.

Case Number	Inlet Void Fraction	$j_f(m/s)$	$j_g(m/s)$
1	0.0376	0.491	0.0275
2	0.220	0.491	0.190
3	0.357	5.000	3.900

Table 20. Experimental data for the Hibiki and Ishii [7] experiments for interface area concentration.

The mesh for these studies consisted of a cartesian, 2D, axi-symmetric configuration. In this one, the axis of symmetry is the axis of the pipe. The mesh is refined towards the wall of the pipe with a geometric bias of 1.2, while a uniform axial discretization is implemented in the axial direction. For each case, the mesh was progressively refined until the outlet interface area concentration at the outlet of the pipe varied lees than 10^{-4}. The results of this grid-convergence study are outlines in Table 21.

Refinement	Degrees of Freedom	GCI - Case 1	GCI - Case 2	GCI - Case 3
1	1.00E+03	-	-	-
2	4.00E+03	-	-	-
4	1.60E+04	7.05E-04	2.93E-04	5.08E-03
8	6.40E+04	6.34E-04	2.47E-04	4.92E-03
16	2.56E+05	8.82E-05	3.15E-05	6.20E-04

Table 21. GCI values for different cases and refinements

The results in the Hibiki and Ishii [7] work are reported as variations in the interface area concentration with respect to the inlet value. The experimental results for the three cases studied are compared against the simulation results in Figure 57. The size of the markers in this figure were taken from the original publication by Hibiki and Ishii [7] and it is assumed that the size of these markers are representative on the experimental errors. As observed in Figure 57, the simulation results agree with the experimental measurements.

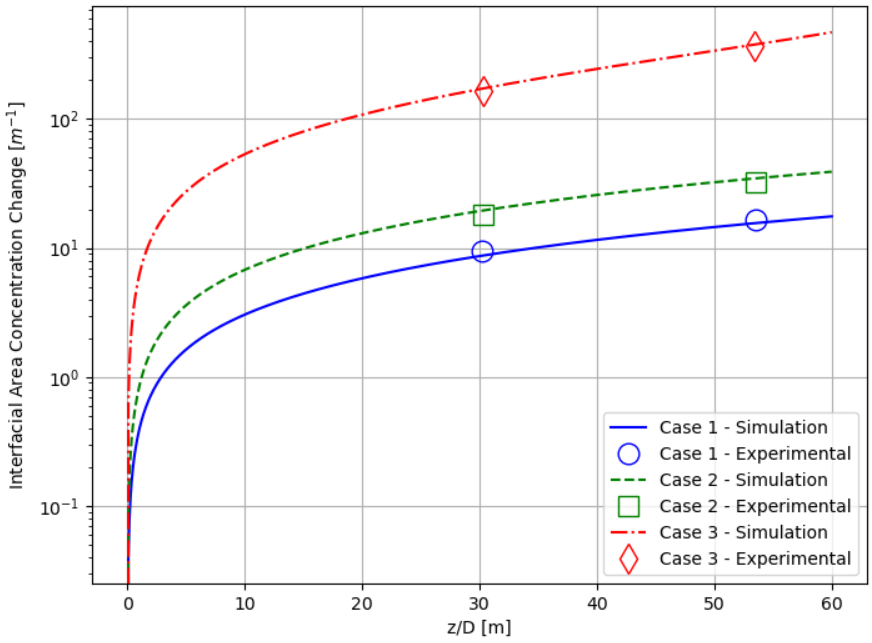

Figure 57. Comparison of Simulation and Experimental Data for Interfacial Area Concentration Change.

4.4. Modeling two-phase flow in Molten Salt Reactors

The previously validated models for the transport of void fraction and interface area concentration are applied to the MSRE. Three models are compared for the MSRE: (i) a 1-dimensional (1D) model, (ii) a 2-dimensional (2D) axi-symmetric model, and (iii) a 3-dimensional (3D) model. For each model, the void fraction and interface area concentration distributions due to gaseous fission products generation are evaluated. The volatilization of fission products and the average size of the bubbles that are generated are a function of many variables, namely, the chemical potential and nucleation sites at the reactor's surfaces, among others, which are not captured in the present model. Hence, a parametric study is developed on the net amount of fission products that are gaseous and the average diameter on the bubbles generated.

Regarding the void fraction production, three of the main fission product contributors to the void fraction production in MSRE are ^{135}Xe, ^{85}Kr, ^{87}Kr. These fission products are noble gases, which indicates that they have a high potential for volatilizing. For thermal fissions from ^{233}U and ^{235}U, the cumulative yield of these fission products is $\sim 9\%$. Nonetheless, previous reports from MSRE have observed that $\sim 1-2\%$ of fission products are gaseous in the molten salt during operation, which indicates that some of the noble gases produced are not volatilizing [39]. Owe to the relative high uncertainty in fission product volatilizing, three different scenarios for void fraction production are studied. First, a low-void production scenario, in which the void fraction production amounts to 0.5% of the fission density. Second, a best estimate scenario, in which the void fraction production is 2% of the fission density. Finally, a high-volatilizing scenario in which the void production is 4% of the fission density. For the final scenario, we do not study the nominal case on which all noble gases are volatilizing and, hence, account for more than 9% of the fission density. The reason for not considering this higher void production scenario is that this case has not been observed in practice during the routine operation of MSRE. All of these cases are compared against a reference case for

which no fission product vitalization is assumed. Also, all these cases assume a best-estimate bubble diameter of 1mm. The parameters for this problem are summarized Table 22. For future reference, this parametric study will be identified as Case A.

Case	Percentage of Gaseous Fission Products	Average Bubble Diameter [mm]
Case A1 - No void fraction (Reference Case)	0%	1
Case A2 - Low Void Fraction	0.5%	1
Case A3 - Best-estimate Void Fraction	2%	1
Case A4 - High Void Fraction	4%	1

Table 22. Test Case A: summary of gaseous fission products and average bubble diameters

Regarding the average size of the gaseous fission product bubbles produced in MSRE, previous reports indicate that the observed size of the bubbles ranged between 0.1 and 1 millimeters [39]. However, in practice, the size of the bubbles may be bigger do to coalescence of bubbles, which is particularly important in regions of low-flow. Therefore, for the average bubble size, three cases are analyzed. First, a case of small bubbles, in which the average bubble diameter is assumed to be 0.1mm. Second, a best-estimate case with bubbles that have an average diameter of 1mm. Finally, a large bubble-case, in which the bubbles are assumed to have an average diameter of 2mm. All of these cases assume a best-estimate void fraction production by fission of 2% of the fission density. For these studies, the reference case for comparison is the case with the bubble diameter of 1mm, since this seems to be the bet-estimate case from previous report [39]. The cases of this parametric study are summarized in Table 23.

Case	Percentage of Gaseous Fission Products	Average Bubble Diameter [mm]
Case B1 - Small Bubbles	2%	0.1
Case B2 - Best Estimate Bubbles (Reference Case)	2%	1
Case B3 - Large Bubbles	2%	2

Table 23. Test Case B: Summary of Gaseous Fission Products and Average Bubble Diameters

Each of these cases will be evaluated in the 1D, 2D, and 3D models. The modeling details for each model are presented in the next section.

4.4.1. Model description for the Molten Salt Reactor Experiment

4.4.1.1. Description of the Molten Salt Reactor Experiment

The MSRE was operated at OakRidge National Laboratory (ORNL) between 1965 and 1969. The reactor was the first thermal-spectrum liquid fuel reactor. The reactor used graphite as it moderator in the core. The

liquid-fuel consisted of a molten salt that served as both a fuel and coolant. The reactor ran for more than 13,000 hours with varying power and fuel composition before its final shut down in 1969. The general layout of the experiment is shown in Figure 58. Additionally, the operational parameters for the MSRE are included detailed in Table 24. Even though the maximum thermal power of the reactor was $10MW_{th}$, we model a case with $5MW_{th}$ in this case as it is more representative of the full power history of MSRE. Now, however, that the conclusions obtained regarding the void fraction distribution and impact on steady-state operation should be approximately independent of the total power of the reactor.

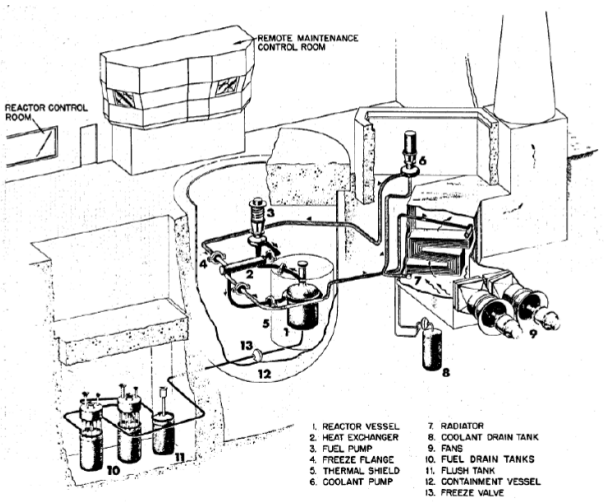

Figure 58. Schematic design of MSRE loops [4].

Table 24. MSRE Reactor Specifications [4]

Parameter	Value
Core Power [MW_{th}]	5
Core height [m]	1.63
Core diameter [m]	1.39
Fuel Salt	LiF-BeF_2-ZrF_4-UF_4
Fuel salt molar mass	65.0%-29.1%-5.0%-0.9%
Fuel salt enrichment	33.0%
Channels in graphite moderator	3.05 cm x 1.016 cm
Channels' rounded corners radii	0.508 cm
Vertical graphite stringers	5.08 cm x 5.08 cm
Mass Flow Rate [kg/s]	130

During operation, the fuel salt was pump by a centrifugal pump, through the primary side of the heat exchanger, and into the downcomer within the reactor vessel. Then, the flow went into the lower plenum, and into the reactor core. The reactor core consisted of rectangular channels in the vertical graphite moderator stringers. Finally, the flow went into an upper plenum and back into the piping that led it to the pump inlet. The circulation time of the fuel in this primary loop was $\sim 25s$.

During operation void in the reactor was introduced by vitalization of the fission products, but also by gas bubbles sparging into the reactor core and entertainment of the cover gas is the centrifugal pump. These two latter effects are not considered in this work since, to the best of our knowledge, they have not been

quantitatively characterized with reasonable experimental uncertainty. Hence, the model developed is not meant to the a faithful representation of the void fraction in MSRE, but rather a tool to evaluate the impact of fission-born void fraction in the steady-state operation of the reactor using different modeling fidelity.

Each of the models developed for MSRE is explained in further detail in the following sub-sections.

4.4.1.2. One-dimensional model

The 1D model is depicted in Figure 59. From left to right in the figure, the model includes the lower-plenum, core, upper-plenum, admission piping to the pump, pump, discharge pumping of the pump, primary side of the heat exchange, admission piping in the reactor core, and downcomer. The length of each of these components has been adapted as the nominal length of the associated MSRE component in order to maintain the circulation time of the liquid fuel. For thermal hydraulics, boundary conditions are used on the between the left and right boundaries of the model in order to link the outlet of the downcomer boundary, on the right, to the lower plenum inlet boundary on the left. The same boundary conditions are used for the transport of neutron precursors. For the neutron flux, fully reflective boundary conditions are assumed at the end of the domain. Note that this implies that the 1D is not modeling leakage. Therefore, for computing the reactivity, the leakage of the model is added via explicit computation of the leakage factors with a $P1$ diffusion approximation.

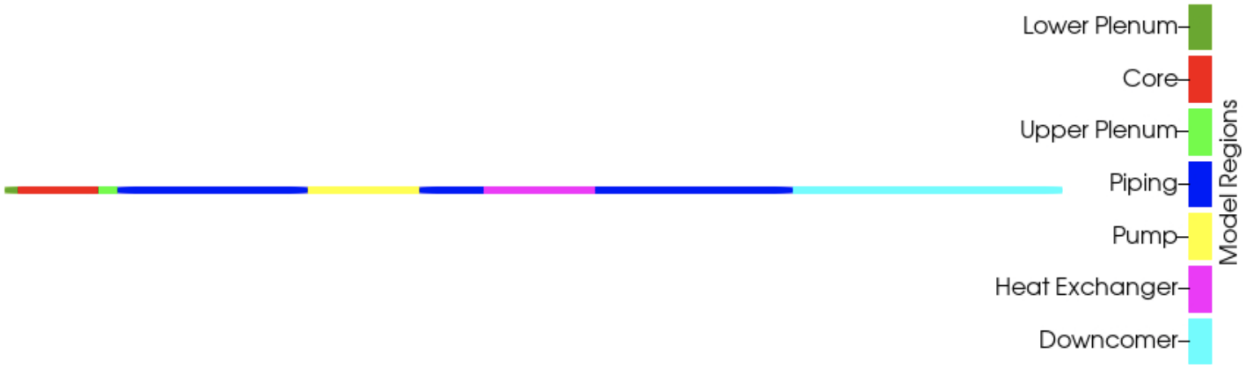

Figure 59. Regions of the 1-dimensional model.

As an example of the model results, key operational fields during steady-state operation are shown in Figure 60. These fields correspond to Case A3, i.e., a void fraction production rate of 2% of the fission density and an average bubble diameter of 1 mm.

The power density peaks at the reactor core and also has a significant peaking power production at the lower and upper plenum. The peaking of the power density at the lower and upper plenum are due to a lower porosity when compared with the reactor core. Downstream, the power density is produced mainly by the decay of the six families of neutron precursors.

The normalized concentrations of neutron precursor families are depicted in the top-right panel of Figure 60. A similar shape than the power density is observed with concentrations peaking at the reactor core and plena and then decaying downstream.

The void fraction and interface area concentration are depicted in the central panels of Figure 60. The void fraction increases as the fuel circulates through the lower plenum, core, and upper plenum. This is due to the void production by the fission density. Then, the void fraction remains constant until the flow reaches the

reactor pump where void is extracted. As expected, the interface area concentration follows a similar shape.

Finally, the fuel salt temperature is depicted in the bottom panel of Figure 60. The temperature increases as the fuel salt circulates through the lower plenum, core, and upper plenum. Then, the temperature remains approximately constant until it is cooled down at the heat exchanger.

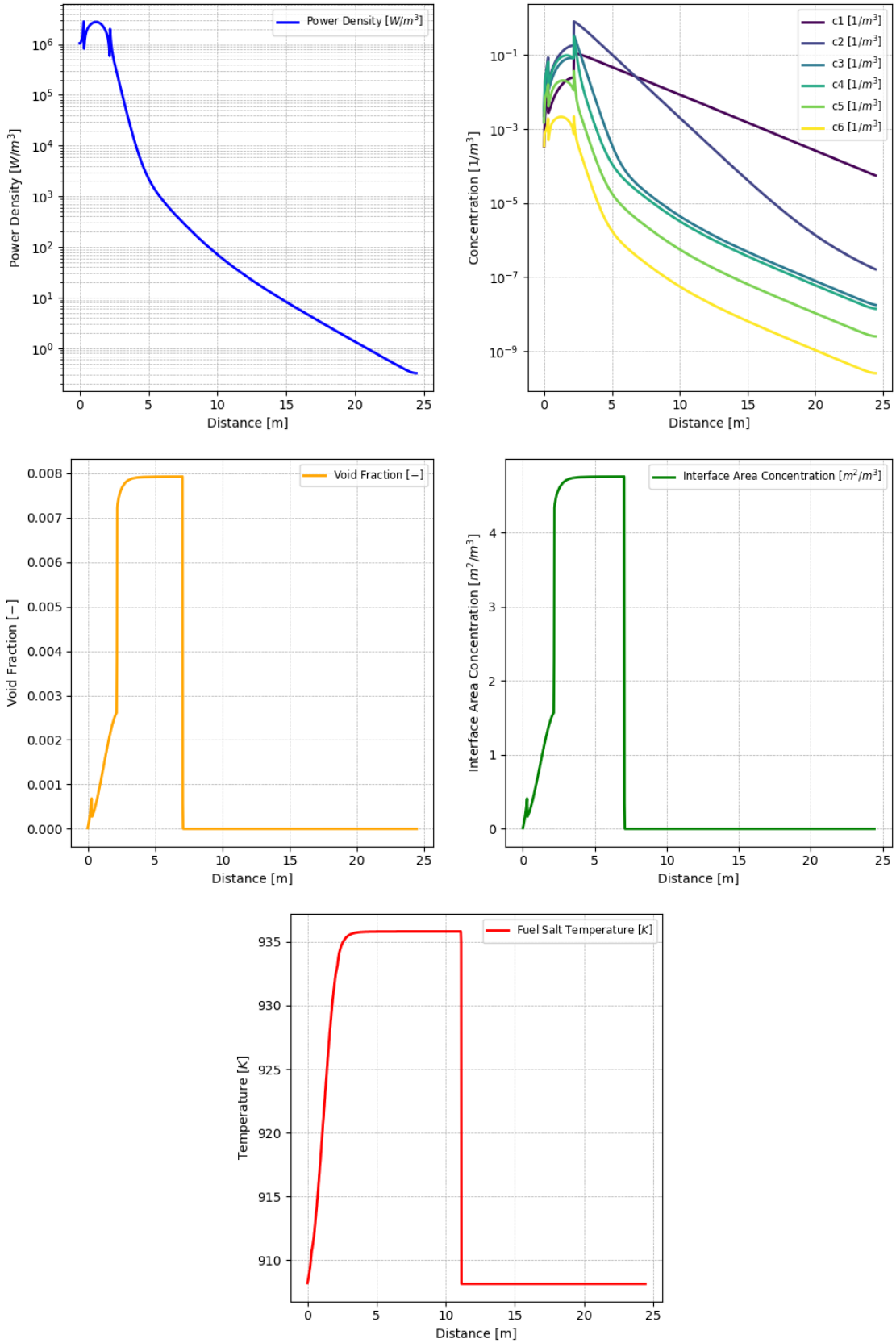

Figure 60. Key operational metrics for Case A3 for the 1D model. Top-left: power density. Top-right: precursor distribution for the six precursor families. Center-left: void-fraction. Center-right: interface area concentration. Bottom: fuel salt temperature.

Grid-convergence studies have been performed by refining the grid until the mean and maximum values of each of the fields studied in Figure 60 varied less then 0.1% under further mesh refinement. This resulted in a mesh with approximately $5,000$ elements. In brief, the 1-dimensional model performs logically within is expected limitations, i.e., inability to model leakage and mixing in the perpendicular direction to the flow one. The 2D axi-symmetric model is analyzed in the next subsection.

4.4.1.3. Two-dimensional, axi-symmetric model

The 2D axi-symmetric model is depicted in Figure 61. The axis of symmetry is the left axis in the domain. In this model, the flow rises in the lower plenum, through the core, and into the upper plenum. Then, the flow goes into an admission pipe and into the pump. The pump volume acts as both linear momentum source and heat exchanger. Then, the flow is pumped through a return into the downcomer and back into the lower plenum. Between the downcomer and core, the core barrel is added, which allows heat transfer between the reactor core and the downcomer. This preheating of the downcomer was necessary for achieving better results for the effective multiplication factor.

For the thermal-hydraulics model, all walls area are assumed to be adiabatic and no-slip boundary. For the neutronics model, all the external boundaries are assumed to be vacuum and the current continuity condition is employed for performing the coupling between internal blocks.

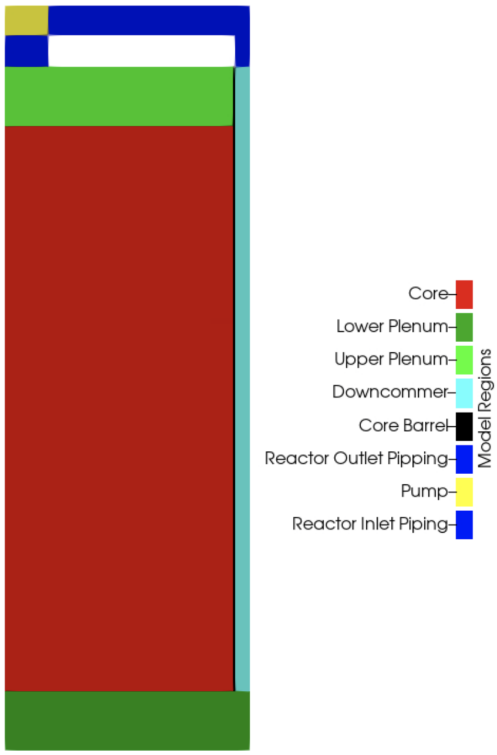

Figure 61. Regions of the 2-dimensional, axi-symmetric model.

The key operation metrics for Case A3 are depicted in Figure 62. A good qualitative agreement is observed when comparing these fields with the average values of the 1D model presented in Figure 60. However, some extra features are observed in this model due to higher fidelity.

Regarding the power density, the expected cosine-like distribution is observed for the power density at the core because of the resolved leakage in the radial and axial directions. Additionally, as for the 1D model, the higher density of fuel salt in these regions when compared to the reactor core results that the power density peaks in the lower and upper plena .

For the delayed neutron precursor families, a significant mixing and advection is observed for the long-lived precursors of family 1, while the distribution for the short-lived precursors of family 6 follow approximately the power density. The distributions for the rest of the families of neutron precursors lie between these two. Beyond the expected axial and radial distributions due to the spatial shape of the power density, a significant amount of mixing is predicted in the radial direction. This gives more validity compared to the 1D model for precursor tracking.

The velocity field behaves as anticipated, showing a uniform upward flow through the reactor core. In the simulation, the flow is restricted to axial channels within the core, preventing any significant radial movement in this area. However, considerable mixing occurs in both the lower and upper plenums. In the lower plenum, this mixing is primarily caused by the inflow from the downcomer. In the upper plenum, the mixing is largely driven by the exit geometry, which accelerates the flow towards the reactor's central axis.

The flow configuration at the reactor core exit plays a critical role in influencing the temperature and void distribution in these regions. Within the core, the temperature distribution corresponds to the power density. However, upon exiting the core, significant mixing occurs, leading to rapid temperature homogenization in the upper plenum. Similarly, the void fraction accumulates near the axis of the model, where the power density is higher. As the flow enters the upper plenum, mixing not only makes the void fraction more uniform, but also traps voids in the upper-right corner of the plenum due to flow blockage and the buoyancy of gas bubbles in that area. The distribution of interface area concentration approximately follows the spatial pattern of the void fraction.

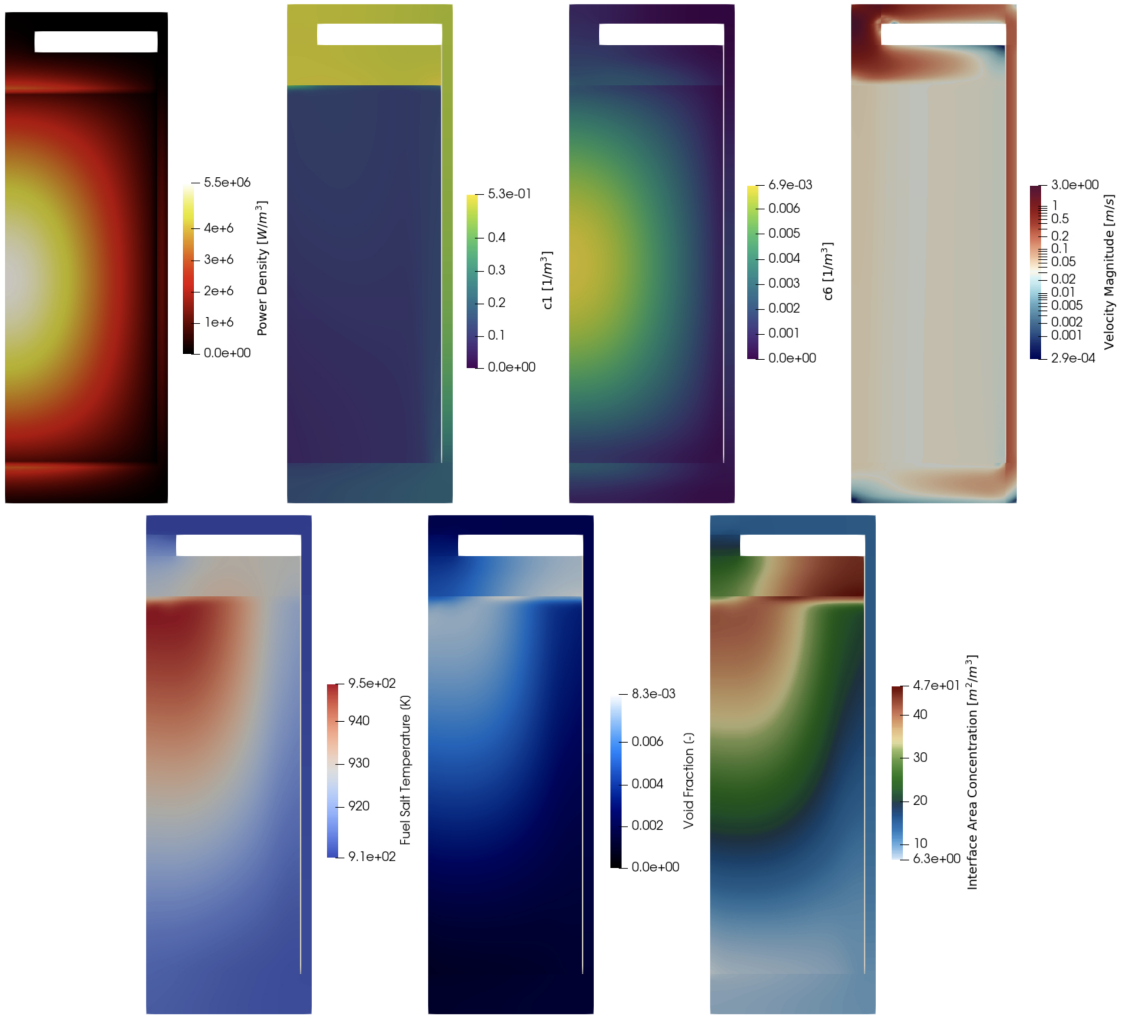

Figure 62. Key operational metrics for Case A3 for the 2D axi-symmetric model. Top-row, from left to right: power density, neutron precursors of family 1 (longest lived), neutron precursors of family 6 (shortest lived), and velocity magnitude (in logarithmic scale). Bottom-row, from left to right: fuel salt temperature, void fraction, interface area concentration.

For this 2D case, a grid convergence studied has been performed for the axi-symmetric model by progressively refining the mesh until the region-wise average and maximum fields presented in Figure 62 varied less than 0.1%. This resulted in a mesh that has approximately 60,000 cells.

In summary, the steady-state operation model analyzed here shows a reasonably good qualitative agreement between the radial-averaged values of the 2D axi-symmetric model and the 1D model. However, the 2D axi-symmetric model offers higher resolution of operational fields, enhancing the model fidelity. Of particular interest for this study is the observation that the void fraction distribution is not radially uniform, necessitating a more detailed model to accurately capture this behavior.

While the 2D axi-symmetric model improves upon the approximations of the 1D model, it still has limitations, such as capturing flow swirling and the detailed geometry of the reactor plena. These challenges are addressed by the 3D model, which is discussed in the next section.

4.4.1.4. *Three-dimensional model*

The 3D model is depicted in Figure 63. For ease of visualization, an isometric view of the reactor core is presented along with an axial cut of the core in this figure. The model involves the regions described for the 2D axi-symmetric model in the previous section. However, there are a few key differences. First, the return piping, heat exchanger, and admission and discharge piping into the pump are modeled in detail. Additionally, the injection of the pipe into the downcomer follows the actual geometry specified for the MSRE. This leads to an injection with a significant tangential components, which causes the flow to swirl through the downcomer and into the lower plenum.

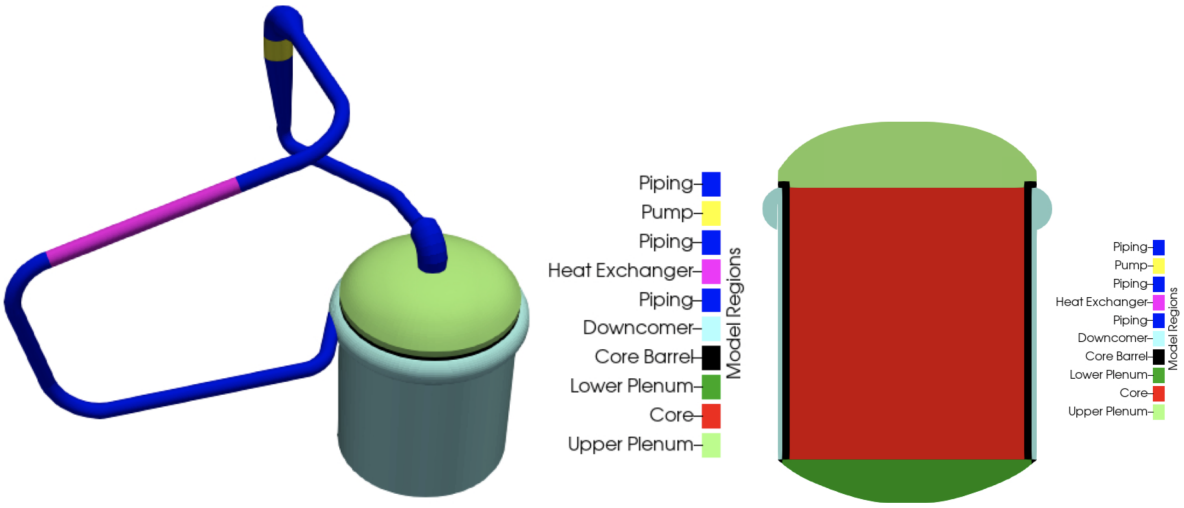

Figure 63. Regions of the 3-dimensional model. Left: full 3D model. Right: detail of the regions in the reactor core.

The streamlines for the circulation of the fuel salt through the core are depicted in Figure 64. The flow swirls at the entry of the downcomer due to the injection by the inlet piping that has a significant tangential components. Then, the flow mixes at the downcomer and rises thtough the core. There is a significant amount of mixing observed at the upper plenum thanks to the sudden flow expansion when exiting the reactor core and its acceleration to the outlet piping.

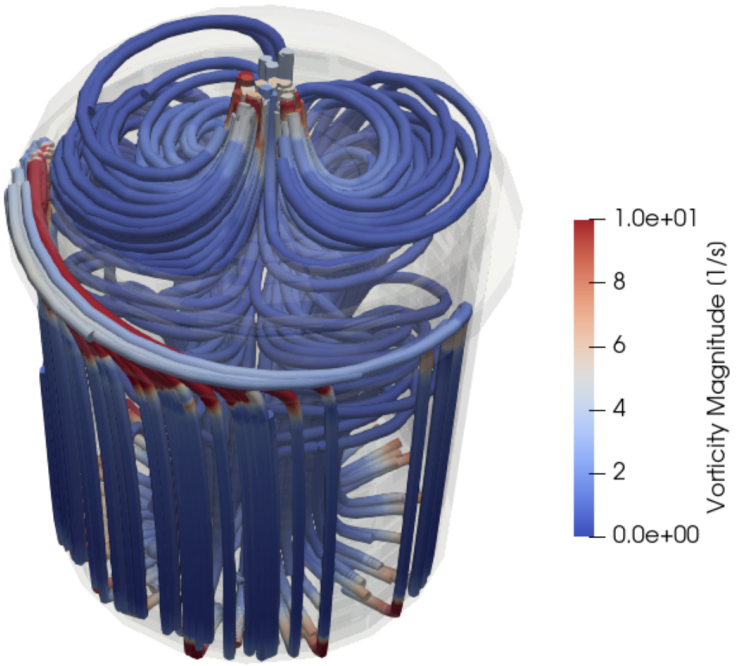

Figure 64. Streamlines for the velocity through the reactor core colored with the magnitude of vorticity.

The operational fields for Case A3 are shown in Figure 65. The main difference with the 2D axi-symmetric model descends to the flow swirling at the downcomer and the mixing at the top plenum. The conjugation of these two effects results in a non-uniform pressure profiles at the reactor core inlet and outlet. This non-uniform difference, in turn, yields a slightly lower flow rate in the core next to the inlet of the reactor core. Note that this non-symmetry may be an artifact of not resolving in detail the structures in the lower plenum. However, it is physically reasonable that the streamlines next to the inlet have a larger pressure drop than the ones further away due to the larger curvature needed to the streamline to get into the reactor core. Hence, this model is a good representation of the 3D effects that may not be fully resolved when using an axi-symmetric model. This is because this axi-symmetric model cannot account for swirling effects and non-uniform in the azimuthal mixing in the top plenum. Beyond this difference, the fields observed are in close qualitative agreement with the 2D axi-symmetric model and the radial averages qualitatively agree with the 1D model.

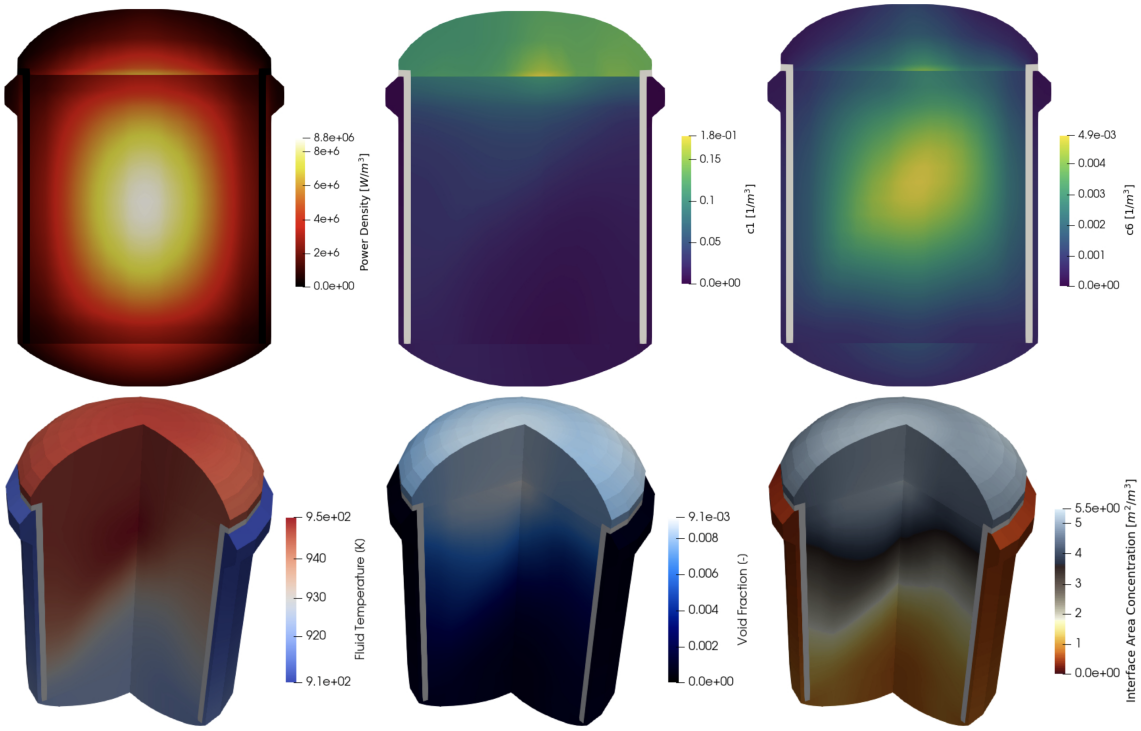

Figure 65. Key operational metrics for Case A3 for the 2D axi-symmetric model. Top-left: power density. Top-row, from left to right: power density, neutron precursors of family 1 (longest lived), neutron precursors of family 6 (shortest lived). Bottom-row, from left to right: fuel salt temperature, void fraction, interface area concentration.

Similar to the two previous cases, mesh convergence studies have been developed on the fields shown in Figure 65 by refining the mesh until the region-wise average and maximum of the fields varied less than 0.5%. The higher tolerance used in this case with respect to the other two cases was to alleviate the computational burden of the simulations and since the changes observed in the quantities of interest at the final grid level were already significantly below than the associated effects caused by the void fraction.

Although the models developed appear physically reasonable, they must be benchmarked to quantitatively demonstrate their accuracy. The details of this benchmarking process are provided in the following section.

4.4.1.5. Model benchmarking

The data reported for MSRE consists mainly of integral data, which makes it challenging to benchmark the higher fidelity models used in this work. Therefore, for testing the thermal-hydraulics model, only the estimate of the pressure drop across the core from inlet to outlet is used. This pressure drop is reported on Figure 65 of the fluid dynamics tests of MSRE [74]. At a mass flow rate of $130 kg/s$, the pressure drop at the core is $\sim$ 10.1 feet of fluid, which equates to $\sim$ 63.5kPa. The pressure drop predicted by the three analyzed models, 1D, 2D axi-symmetric, and 3D, is detailed in Table 25. For all cases, the pressure drop is close to the one estimated during operation, which yields more confidence in the thermal-hydraulics models used. The reason why the pressure is different for the 1D model is that these code relies on correlations for capturing the pressure drop at the reactor downcomer and plena, while the 2D axi-symmetric and 3D model capture the friction against the walls explicitly in the model. Nonetheless, a reasonable agreement is obtained between

the estimated operational pressure drop and the ones predicted by the models.

For benchmarking the neutronics model, the zero power eigenvalue during the ^{235}U-based operation or the MSRE benchmark [8] is used as a reference. The value computed by Serpent 2.1.30 for this case is 1.02132, which is know to be higher than the reference benchmark value of 0.99978. This overestimation has been previously justified on uncertainties in the thermal scattering cross sections for graphite. It is observed that for the zero-power case, the eigenvalues predicted by the 2D axi-symmetric and 3D models agree reasonably well with the eigenvalue predicted by the Monte Carlo code. The 1D model presents a slightly worse agreement, which is reasonable because the leakage in this model is estimated from a P1 extrapolation of the flux at the boundary. Nonetheless, we can conclude with confidence that the models agree well with the benchmark data.

Model	Pressure Drop [kPa]	Effective Multiplication Factor
Expected	63.5 [74]	1.02132 [8]
1D Model	58.1	1.01739
2D Axi-symmetric Model	63.6	1.02223
3D Model	63.6	1.02211

Table 25. Comparison of Pressure Drop and Reactivity across Different Models. The pressure drop is taken from the estimated MSRE operation. The eigenvalue reference value is taken as the one from the MSRE benchmark [8].

This section has detailed the models for MSRE an analyzed operational fields during steady-state operation. Additionally, the models have been compared against operational MSRE data and results from the MSRE benchmark. In the next section, the results for the parametric studies to void fraction production are outlined.

4.4.2. Impact of void generation and bubble mean diameter on the steady-state operation of MSRE

For the three modeling approaches analyzed in this work, the impact of the void fraction production by fission (CASES A) and the average bubble diameter (CASES B) are analyzed in this section. The section is split into three parts. First, the impact on the reactivity is analyzed. Second, the effect on the average and maximum temperature in the fuel salt and the fuel salt at the core are studied. Finally, the influence on the void fraction and interface area concentration in the lower plenum, core, and upper plenum are inspected.

4.4.3. Impact on steady-state effective multiplication factor

For analyzing the impact on reactivity, only the reduction in the mixing density due to void production is analyzed. This means that the extra absorption by fission products accumulating in the gas bubbles are neglected. This is a reasonable approximation for this study since the main scope is to assess if the modeling approach has an impact on the expected reactivity of MSRE.

Table 26 shows the changes in reactivity for the three volatilization scenarios analyzed, CASE A2, CASE A3, and CASE A4, against the non-volatilization reference CASE A1. As expected, reactivity reduces as void is introduced in the fuel salt. This is because the fuel salt is displaced away from the reactor core due to the production of gas bubbles. For all cases, the higher the void fraction production, the higher the reduction in reactivity. However, significant differences are observed in the reactivity reduction predicted by each model.

For instance, for the 1D model, the reduction in reactivity is produced only by the reduction in fission over absorption. Note that this model does not capture leakage and hence, as expected, the observed reduction in reactivity is smaller than the other two cases. In the 2D axi-symmetric model there is no possibility of azimuthal void shifts as the power density varies due to void production. This leads to an over-estimation of void towards the external radius of the reactor, which ultimately results in an over-prediction of leakage due to void fraction production. This is the main reason why the 2D axi-symmetric model predicts a reduction of reactivity with void accumulation that is higher than the 3D model.

Case / Reactivity Introduced [pcm]	**1D Model**	**2D Axi-symmetric Model**	**3D Model**
Case A1 - No void fraction (Reference Case)	-	-	-
Case A2 - Low Void Fraction	-6.2	-82.0	-56.0
Case A3 - Best-estimate Void Fraction	-30.8	-410.7	-263.6
Case A4 - High Void Fraction	-61.3	-824.1	-535.8

Table 26. Comparison of reactivity differences introduced by void for varying void fraction production from fission (Case A) across different models.

The changes in reactivity due to the size of the bubbles are presented in Table 27. This table compares the cases of small bubbles, CASE B1, and large bubbles, CASE B3, against the reference case CASE B2. Contrary to the void fraction, the average size of the bubbles does not have a significant impact in reactivity as they do not change the average density of the salt. The effect is at most of second order since the size of the bubbles will change the drift velocity, which will, in turn, affect the transport of bubbles throughout the reactor loop. For the 1D model, this effect is negligible since these changes in the drift velocity do not significantly affect the void distribution in the core and plena because cross flows are not captured in this model. For the 2D axi-symmetric case the effect is larger due to void reaccommodation as the drift velocity changes. As expected, the effects in the 3D model are even larger because of the possibility of void re-distribution into the azimuthal angle. Nonetheless, for every case, the reactivity changes introduced by the changes in bubble diameter can be neglected without incurring in significant errors.

Case / Reactivity Difference [pcm]	**1D Model**	**2D Axi-symmetric Model**	**3D Model**
Case B1 - Small Bubbles	-5.40×10^{-6}	-1.40×10^{-1}	-3.90×10^{-1}
Case B2 - Best Estimate Bubbles (Reference Case)	-	-	-
Case B3 - Large Bubbles	4.20×10^{-6}	4.30×10^{-1}	9.10×10^{-1}

Table 27. Comparison of Reactivity Differences for Varying Bubble Sizes (Case B) across Different Models

4.4.4. Impact on the fuel salt temperature

The impact of the void fraction production on the temperature fields in the fuel salt are depicted in Figure 66. The temperature changes observed due to void distribution are rather small and could be neglected

for most engineering purposes. However, it is interesting to examine the dynamics of temperature changes as a progressively larger void fraction is produced from CASE A2 to CASE A4. For the 1D model, the behaviour follows a simple enthalpic balance. As more void is produced, the mixture mass heat capacity reduces and hence, both the average and maximum temperature increases. The situation is more complex for the higher-dimensional models. As void is introduced in the 2D-asymmetric and 3D models a larger mixing is produced at the reactor core and plena due to the density gradients caused by the void fraction.

This increased mixing results in a reduction of the maximum temperature in all cases. When examining the average temperature, the 2D axisymmetric model shows the expected increase due to the reduced mass heat capacity of the salt. However, the 3D model follows this trend only in the high void fraction scenario. In cases with lower void fractions, the additional head generated by the buoyancy of fission gases effectively increases the flow rate, which in turn reduces the average temperature. This effect cannot be captured by the 2D axisymmetric model because the heights of the pump, heat exchanger, and return piping do not match the actual configuration of the MSRE primary loop.

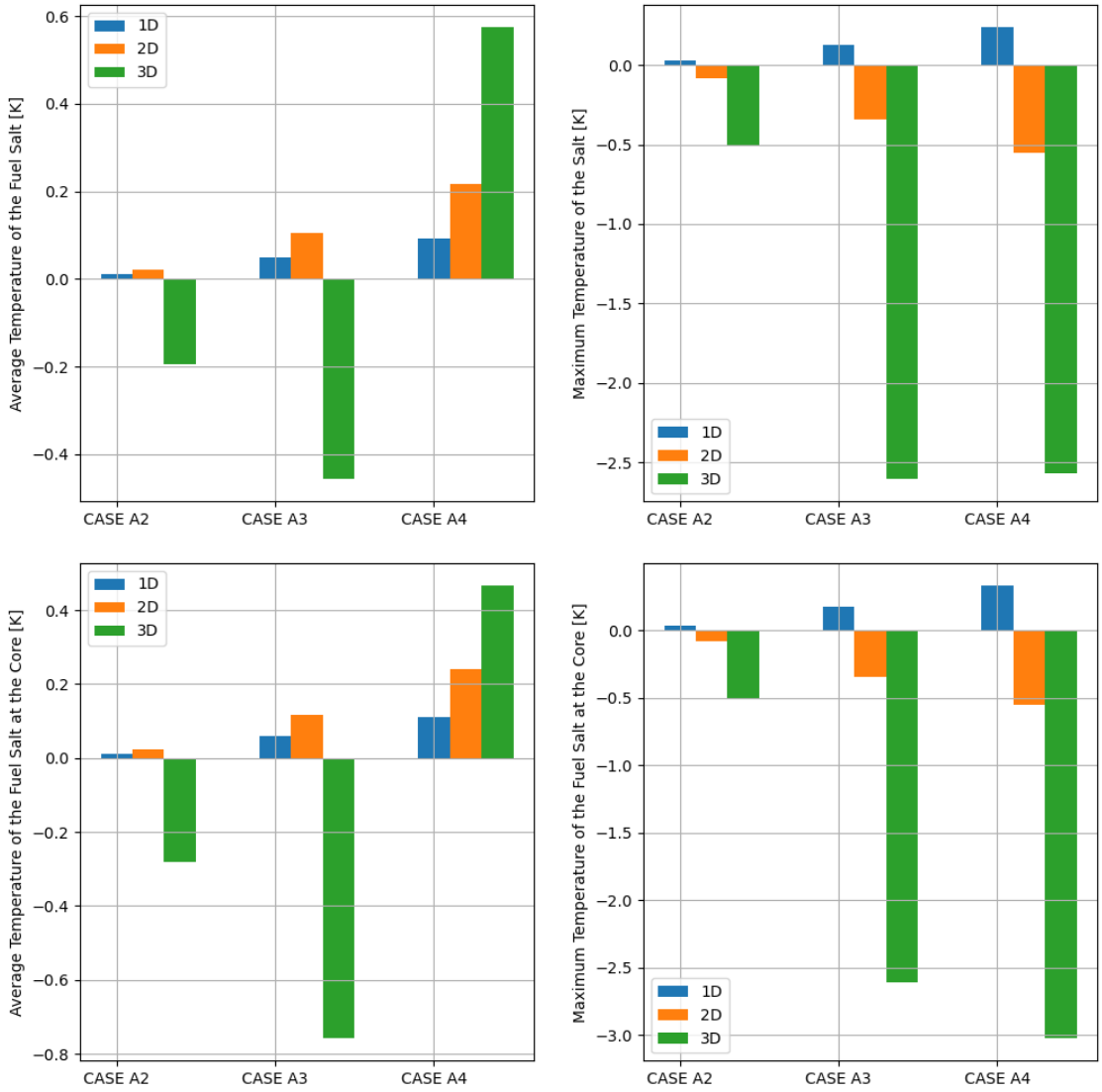

Figure 66. Temperature changes for CASE A2-A4 compared against CASE A1 for the different models developed in this study.

The temperature changes due to the varying mean bubble diameter are presented in Figure 67. As for the reactivity, the effects of the bubble size on temperature change are small and mostly based on second order effects. Even though these changes follow physical behavior, its analysis is too intricate to serve for any practical purpose. Hence, this study simply demonstrates that the average bubble diameter has a small effect on the temperature field and further analysis of the observed trends is purposely omitted.

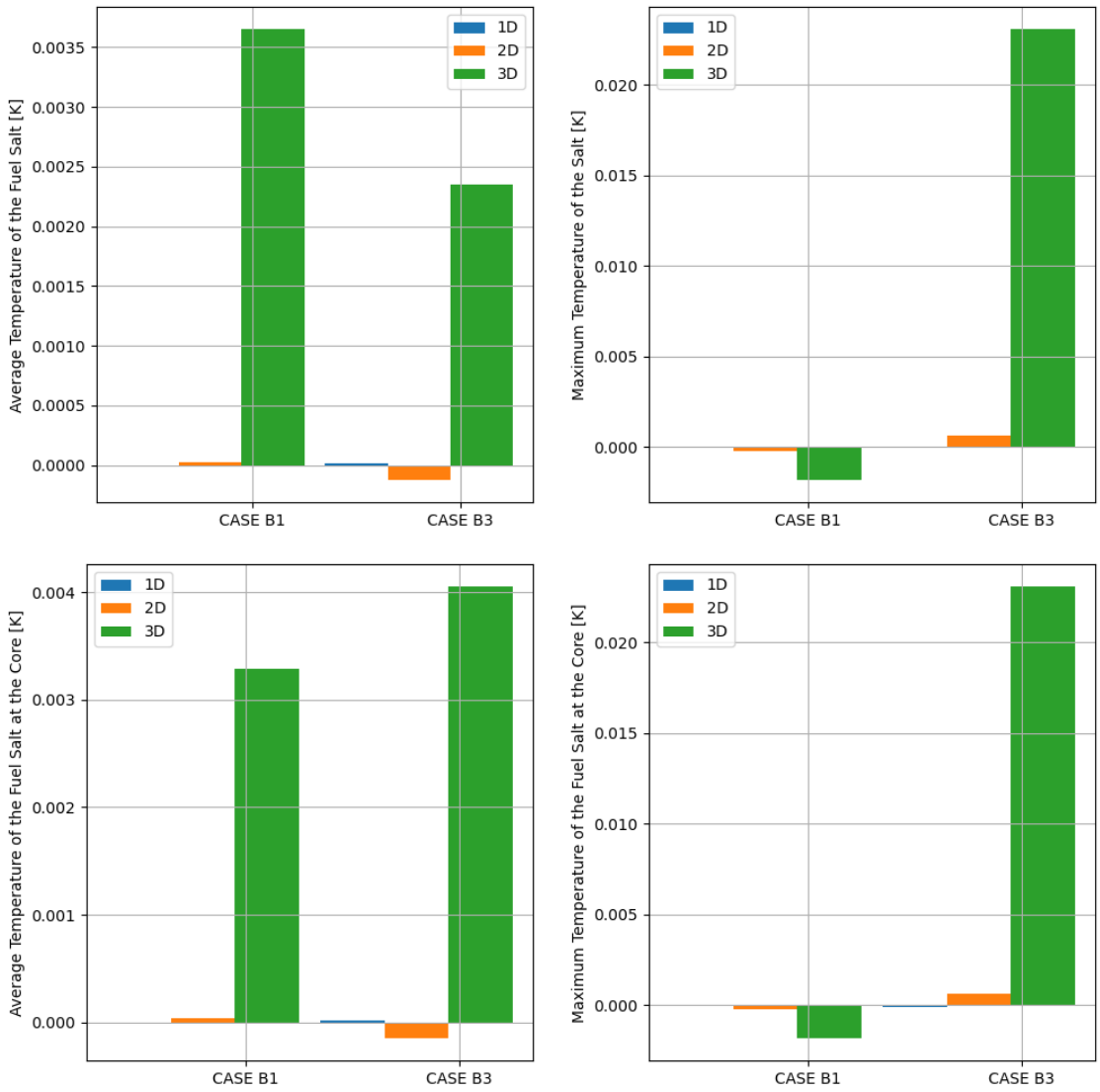

Figure 67. Temperature changes for CASES B1 and B3 compared against CASE B2 for the different models developed in this study.

4.4.5. Impact on the void fraction and interface area concentration distribution

The impact of the rate of void fraction production from fission on the distribution of void and interface area concentration is shown in Figure 68. As expected, both the average and the maximum void fraction increase as the volatization rate of fission products increases. The trends predicted by the three models is similar. However, when comparing these models in further detail one sees that the 2D axi-symmetric models predict a higher increase of void fraction at the lower plnum and core, wheres for the 1D and 3D models predict a higher increase at the upper plenum. This higher prediction in the upper plenum for both models follow different reasons. For the 1D model, since the radial distribution of the fission density is not modeled, the fission density in the upper plenum is over-predicted. This leads to the higher void fraction observed for the upper plenum. For the 3D model, the flow towards the external radius of the upper plenum is significantly occluded when compared to the one in the 2D axi-symmetric model. This leads to an accumulation of void in

the upper plenum that is higher in the 3D model. Finally, the interface area concentration follows a similar trend as the void fraction distribution. This suggests that the interface area concentration primarily depends on bubble diameter, with bubble breakup and coalescence effects being similarly minimal across all models.

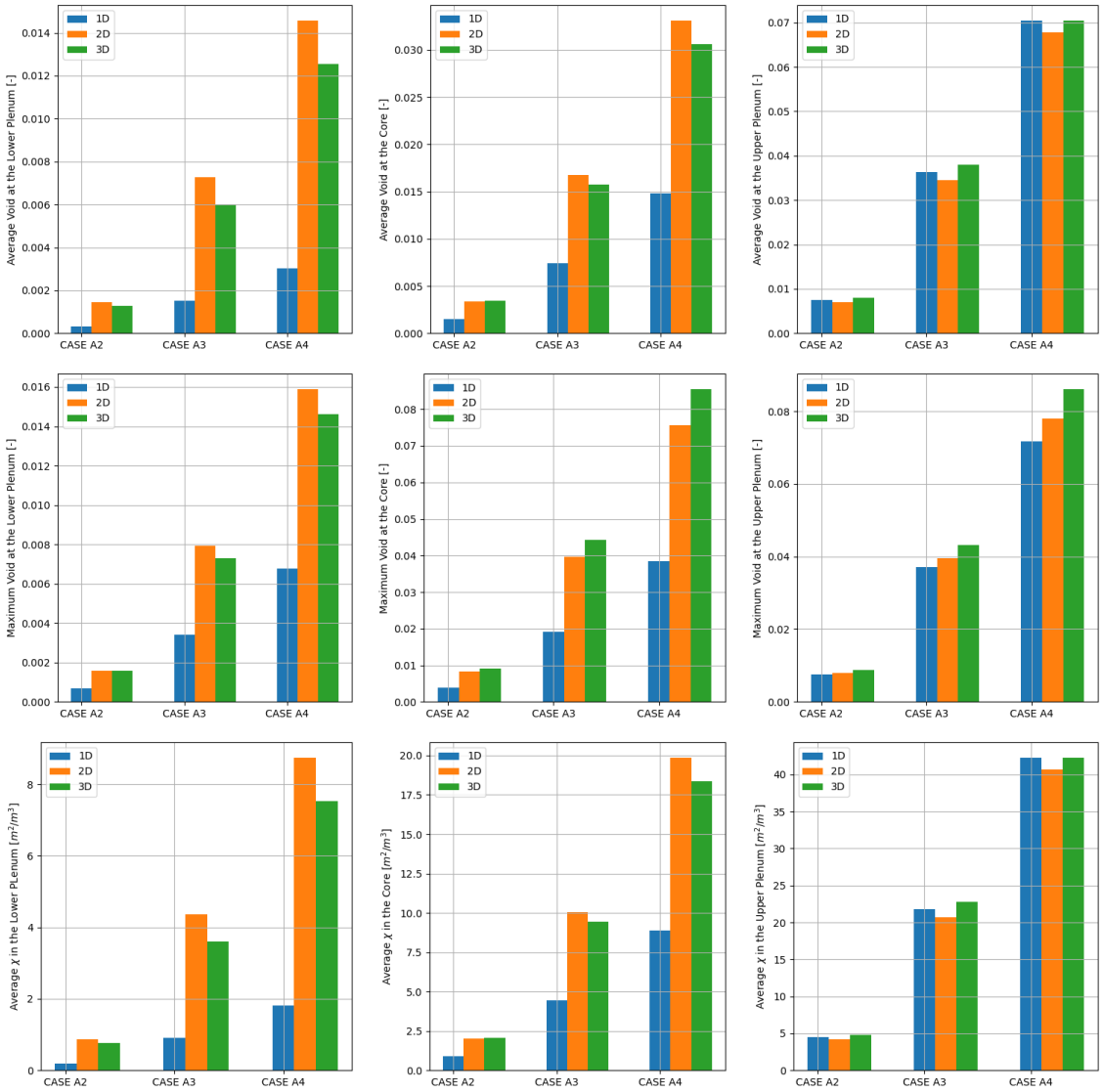

Figure 68. Void fraction and interface area concentration changes for CASE A2-A4 compared against CASE A1 for the different models developed in this study.

The effect of the mean bubble diameter on the void distribution and interface area concentration are depicted in Figure 69. As expected, the effect of bubble diameter is insignificant for the void fraction distribution on the 1D model. This is because, the 1D slip velocity is very lightly affected by the bubble diameter, which, in turn, do not significantly affect the void fraction distribution. The situation is different for the higher fidelity models where the bubble diameter has an more significant impact on the slip velocity and hence, the void fraction distribution. In the 2D axisymmetric model, the effect of bubble size is more linear. Smaller bubbles are more easily transported by the flow field, leading to an increase in void concentration throughout the primary loop. Conversely, larger bubbles are less mobile and tend to reduce void concentration.

The dynamics in the 3D case are more complex. Large bubbles have a lower slip velocity, resulting in their accumulation in the lower plenum and more efficient clearing of bubbles from the reactor core and upper plenum as they enter the inertial regime. The opposite occurs for smaller bubbles, which are less likely to accumulate and more readily carried through the system. However, within the range of bubble sizes studied, the impact of bubble diameter on void distribution remains relatively small.

Finally, changes in interface area concentration show a strong dependence on bubble size. For smaller bubbles, interface area concentration increases significantly, while for larger bubbles, it decreases. This effect is nonlinear: the relative decrease in interface area concentration for larger bubbles is smaller than the relative increase observed for smaller bubbles. This is essential since non-equilibrium models as the one described in Eq. (68) are needed for accurate modeling of the interface area concentration tracking.

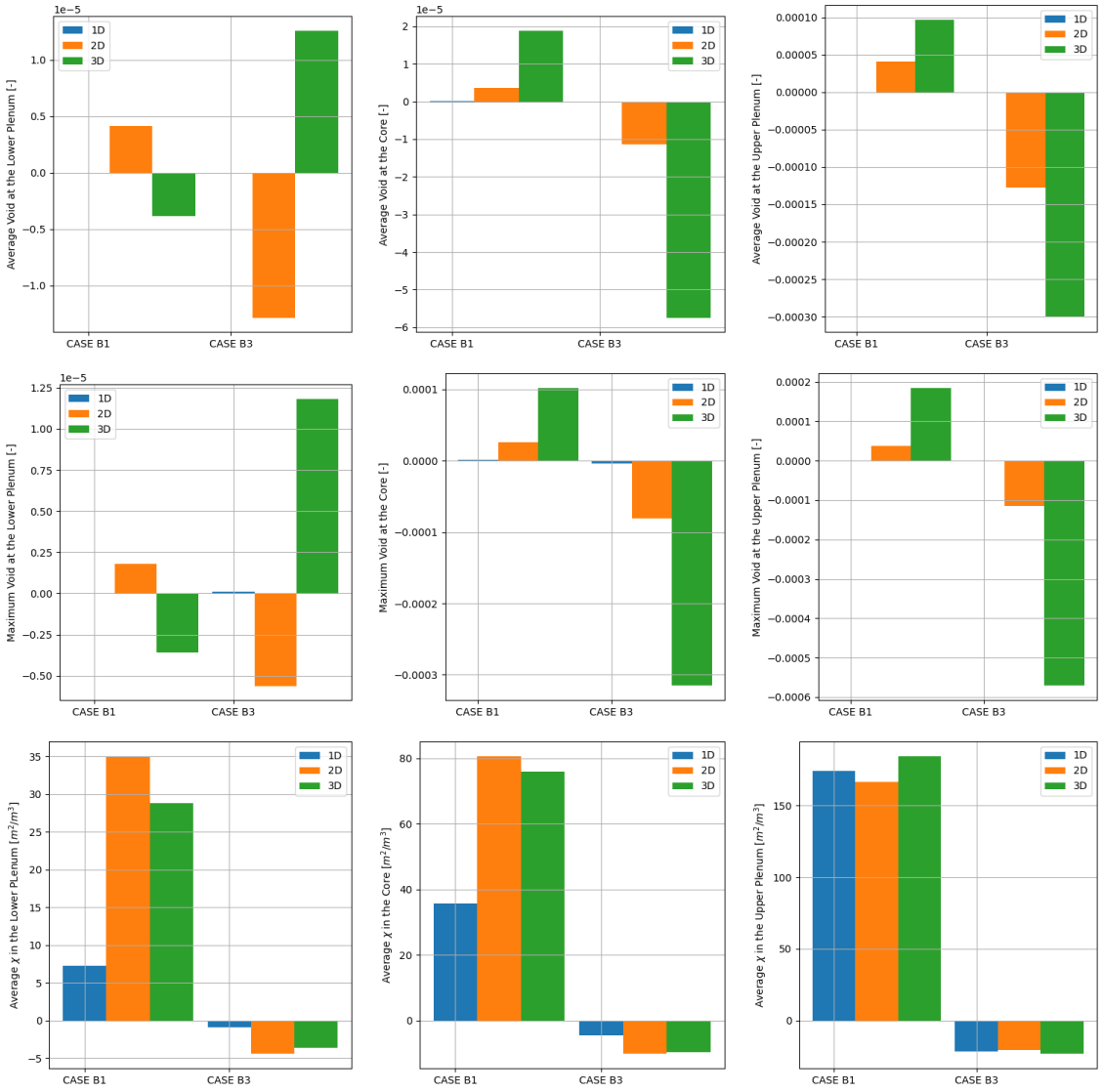

Figure 69. Void fraction and interface area concentration changes for CASES B1 and B3 compared against CASE B2 for the different models developed in this study.

4.5. Recommendations for two-phase modeling of MSRs

Based on the results of this study, several recommendations for advancing two-phase flow modeling in MSRs are proposed.

The current model demonstrates good agreement with experimental data in two-phase air-water experiments. However, further validation for this model is needed for a gas phases in molten salt coolants. Validation efforts should ideally focus on benchmark comparisons with MSR-specific experiments, particularly those that provide detailed measurements of void fraction and interface area concentration. The results from this study, particularly in capturing the impact of void fraction on reactivity and temperature distributions, indicate that more comprehensive validation is needed for ensuring the model's accuracy in predictive simulations.

The sensitivity analysis performed in this work has shown that key parameters such as void fraction production rates, bubble sizes, and slip velocities significantly influence reactor behavior. The observed differences in void fraction distribution and temperature profiles across 1D, 2D, and 3D models suggest that 3D models are needed for better capturing the the void distribution in the reactor core and plena.

For evaluating the performance of MSRs, the integration of two-phase flow models into multiphysics simulations is necessary. The results have demonstrated that coupling the fluid dynamics model with neutronics and thermal-hydraulics is needed for accurately capturing the reactor's reactor reactivity. The observed impact of void distribution on reactivity, particularly in the 3D model, supports the recommendations to use multiphysics platforms, like MOOSE, for MSRengineering evaluation.

The study's results also suggest that while 1D and 2D models can be more computational efficient, they fail to capture some critical 3D effects such as flow swirling and non-uniform void distributions. The 3D model provided more accurate predictions of these effects, particularly in regions with more complex flow configuration like the reactor core and plena. Therefore, for detailed reactor design and safety analysis, 3D modeling should be prioritized to ensure all significant physical phenomena are accurately represented.

The dynamic response of the reactor to transient scenarios, such as reactivity insertion and loss of flow accidents, was not fully captured in this study, which was mainly focus on predicting the impact of void on the steady-state reactor operation. Extending the two-phase flow model to transient scenarios is necessary. The 3D model's ability to capture flow dynamics with higher fidelity suggests that it would be particularly effective in simulating these transient events, where rapid changes in void distribution can significantly impact reactor safety.

The study also points to the need for future experimental work that provides high-fidelity data specific to MSRconditions, including detailed measurements of interface area concentration, bubble dynamics, and two-phase flow behavior under various pressures and temperatures. Such data are needed for refining the model's predictive capabilities. These recommendations, grounded in the results obtained in this work, aim to improve the reliability and accuracy of two-phase flow models in MSRs, supporting their safe and efficient operation.

4.6. Conclusions

This work has developed a methodology for simulating two-phase flow dynamics in MSRs, focusing on void fraction transport from fission gas volatilization. Implemented in MOOSE, the model integrates a multidimensional drift-flux formulation with an interface area concentration model. Validation against experimental data has shown accuracy within 5% in predicting void fraction distributions and interface area concentrations. The model has then been applied to a previously validated model of the MSRE to study the impact of the dimension of the model on the void distribution predicted during the steady-state operation of

the reactor.

Key results include a void fraction increase of up to 2.5% in the reactor core under high fission gas production scenarios (4% of fission density), leading to a reactivity reduction of 500 pcm in the 3D model. The 2D axi-symmetric model predicted a 410 pcm reduction, and the 1D model predicted a 61 pcm reduction. The interface area concentration increased by 15% when the average bubble diameter decreased from 2 mm to 0.1 mm, impacting mass, momentum, and energy exchange. Void fractions in the upper plenum reached up to 6%, particularly under higher gas production rates.

These findings underscore the necessity of three-dimensional, multiphysics models to capture the full impact of void formation on MSRreactivity and thermal-hydraulic behavior. The 3D model's ability to predict a 500 pcm reactivity reduction, compared to the lower reductions seen in 2D and 1D models, demonstrates the limitations of lower-dimensional approaches. Accurate modeling of void distribution is essential for predicting reactivity changes, which can considerably affect the reactor design. Also, the observed reduction in reactivity due to void accumulation directly affects reactor control and stability, making it an important factor in safety assessments and operational planning.

Future work should extend the model to dynamic scenarios such as reactivity insertion and loss-of-flow accidents. Further validation against MSR-specific experiments, particularly under variable pressure and temperature conditions, is necessary. Integrating detailed bubble dynamics and expanding the approach to real-time simulation platforms is recommended.

5. IMPROVEMENTS IN DOMAIN-OVERLAPPING COUPLING ACTION BETWEEN PRONGHORN AND SAM

This section contains some of the content of a journal article that will be submitted to Nuclear Engineering and Design in September 2024 as part of this milestone.

5.1. Introduction

This year, our research group at the INL has supported the United States Department of Energy (DOE) Nuclear Energy Advanced Modeling and Simulation (NEAMS) program by implementing improvements and corrections to the BlueCRAB (Comprehensive Reactor Analysis Bundle) code suite, specifically to its multiscale coupling between thermal-hydraulics simulations. Enabling multiple approaches for modeling and simulating fluid flow and heat transfer has been a research topic of great interest over the past two decades [75]. The motivation for these works is given by the broad spectrum of scales existing in both time and space that manifest in reactor core analysis, for which different numerical methods can have their own set of advantages.

BlueCRAB is a comprehensive code suite designed to analyze advanced reactor designs, including molten salt reactors, fluoride salt-cooled high-temperature reactors, and microreactors. This simulator is based on the MOOSE framework [76], and it can cope with the requirements for reactor analysis discussed above while coupling Pronghorn [77] and the System Analysis Module (SAM) [78]. It should be noted that similarly to BlueCRAB, Pronghorn, and SAM are also MOOSE-native applications, which facilitate transfers of data across their concurrent simulations.

Specifically, Pronghorn is a homogenized multiscale analysis tool based on the Finite Volume Method. BlueCRAB leverages Pronghron as its engineering scale tool while modeling the reactor core and related components using a two or three-dimensional representation—e.g., downcomer and plena regions. At the same time, SAM—which is based on the Finite Element Method—utilizes a zero and one-dimensional formulations to model fluid-flow in piping components, for instance, including conduits, elbows, valves, and pumps, which composes systems connected to the reactor. Both approaches are tailored to support computationally affordable transient simulations of reactor cores on desktop computers.

In Ref. [75], several coupling strategies are extensively reviewed, and these can be categorized based on the approach used to decompose the computational domain of the coupled simulations. In most previous works, researchers pursued separate domain coupling methods and proposed to split up the simulation domains, the idea being to solely exchange data via the inlet/outlet interfaces between the two simulations. BlueCRAB implements an overlapping domain approach similar to what was described in a previous work [5]. Conversely, this technique proposes transferring data not only via the interface boundary between the two domains but also within the overlapping region. Recent studies have demonstrated that coupling approaches based on the domain overlapping are more robust than conventional separate domain approaches [79, 80], thus justifying its choice.

Ref. [5] introduced a coupling methodology, including its formulation and execution scheme, that enables an agnostic interface between the overlapping simulation domains of SAM and Pronghorn. The proposed approach ensures that each simulation retrieves the same momentum and energy balance across the coupled section, even considering multiple inlets and outlets. This technique achieves converged values for the quantities of interest through Picard iterations in an explicit scheme. Namely, BlueCRAB dictates a scheme based on fixed point iterations leading to pressure drops and energy that are in good agreement. For this reason, these results are termed “self-consistent”.

As part of its mission to support the development of advanced non-LWRs, the BlueCRAB code suite must demonstrate the ability to simulate coupled analyses using Pronghorn and SAM while considering diverse flow and heat transfer conditions relevant to safety analysis. While the original implementation proposed in Ref. [5] predicts "self-consistent" results as shown in that technical report, the present work introduces improvements and—in some instances—corrections to the original version.

First, we review and propose adaptations to the coupling momentum formulation to extend this method to address not only incompressible, but also compressible flows. Second, we implement support for handling flow reversal, which requires a control logic based on SAM predictions and a specialized set of switching boundary condition in Pronghorn. Finally, a correction to the original method has been implemented and tested to ensure appropriate coupling in unevenly heated regions, for instance if modeling both riser and core. This correction is crucial because the original version could lead to unrealistic heating in regions without the presence of heat source, e.g., in the riser, within the coupled SAM simulation.

The present work propose a series of problems to test the implementation of the abovementioned applications. First, BlueCRAB address canonical pipe flow setups under laminar conditions, considering both incompressible and compressible fluids. These setups are carefully chosen such that simple hand calculations for the verification of the numerical predictions. Second, the method for handling flow reversal is tested using a pump driven loop with varying head that causes the circulation to alternate. Again, the setup is simple enough to ensure that the predictions match with analytical solutions. Lastly, we perform coupled simulations considering a more complex setup of the High-Temperature Reactor-Pebble-bed Module (HTR-PM). In this setup, the coupling between SAM and Pronghorn encompass the riser, the core, plena regions, and the discharge chute, whereas SAM models the entire primary system. While comparisons with experiments are not included in the results for this case, one verifies that operation parameters are—which includes core pressure drops and inlet/outlet temperatures—matches between the coupled simulations and, at the same time, are in good agreement with the specifications of the reference facility.

We stress that the domain overlapping coupling approach in BlueCRAB is not taylored for a specific non-LWR design. This work adopts the HTR-PM as a practical application case to demonstrate that the coupling formulation is suitable for compressible coolants, thereby introducing additional complexity. At the same time, the code can also support incompressible cases, including MSRs.

This work is organized as follows: Section 5.2. presents the revised coupling methodology, detailing both advancements in the implementation and corrections compared to what orginally proposed in Ref. [5]. Section 5.3. presents the test cases and simulation setups. Finally, the results are displayed and discussed, followed by a conclusion and recommendations for future work.

5.2. Coupling Formulation and Methodology

This section presents the revised overlapping domain coupling formulation developed in this work. The key aspect of this method is to match the momentum and energy balance between the two simulations by transferring physical quantities where the multimentional and the system-level simulation domains overlap. Fig. 70 schematically represents, for an arbitrary wall-bounded flow configuration, the required transfers of coupled simulations based on the overlapping domain approach. One may notice the that the goal of the proposed diagram is simply to illustrate the quantities being transferred in the coupled simulations, thus it does not provide a complete description of the implementation in BlueCRAB.

While a system-level simulation holistically models any setup of interest, it can naturally provide the required boundary conditions (BCs) to a coupled multiscale simulation on the interfaces between the two domains. As indicated in Fig. 70, the system-level model (e.g., SAM) sends the multiscale model (e.g.,

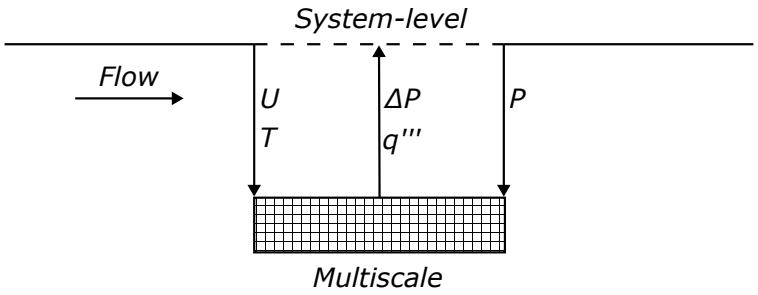

Figure 70. Schematics showing transfers in a overlapping domain coupled simulation.

Pronghorn) the bulk flow velocity U and the temperature T as Dirichlet BCs to the inlet, along with the pressure P at the outflow interface. In return, the system-level simulation receives a pressure drop ΔP and a heat source q''' computed based on the conversation of momentum and energy accross the multiscale domain. Having discussed these concepts, the following sections detail the implementation of these transfers in BlueCRAB.

5.2.1. SAM-Pronghorn Coupling Interface in BlueCRAB

Fig. 71 schematically represents the interface between the two codes considering an arbitrary geometry with multiple interfaces in the coupled region. No changes have been made to the interface between the SAM and Pronghorn codes, as it remains the same as originally proposed in Ref. [5]. Each of the inlet/outlet interfaces of overlapped coupling regions is labeled as E_i, with index ranging from $i = 1$ to the total number of interfaces, in this case $i = 5$ based on the generic, though merely representative, schematic presented. In fact, one should notice that this generic representation does not specify whether any E_i interface is an inlet or an outlet. Instead, the SAM model determines the flow direction while BlueCRAB identifies and transfers the appropriate set of BCs to Pronghorn over its interfaces. Section 5.2.6. details such an aspect, which is important for handling flow conditions.

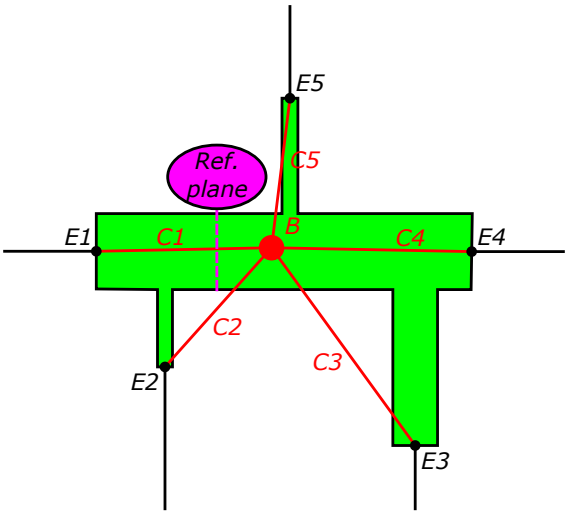

Figure 71. Sample schematics showing agnostic interface between SAM and Pronghorn implemented in the overlapping domain approach of BlueCRAB (adapted from Ref. [5]).

Starting from each of the E_i interfaces, the SAM models one-dimensional pipe components that are

connected to a single branch labeled B. Accordingly, each of these components is identified as C_i. This configuration ensures that all interfaces are connected and form a single and continuous system-level code simulation. In the Pronghorn simulation, a reference plane is defined to pair with each of the E_i interfaces. Conveniantly, each of these pairs can be mapped onto the SAM one-dimensional components C_i. This way, the proposed interface ensures that pressure drops and heat sources computed across plane pairs in the multiscale simulation are transferred to the corresponding overlapping C_i components. Consequently, this methodology is considered agnostic, as the same logic applies to any configuration, regardless of the number of inlets/outlets and geometry.

As discussed in Ref. [5], the branch in SAM model is ultimately arbitrarily defined. In contrast, the reference plane must satisfy certain requirements while dealing with unevenly heated regions. Section 5.2.5. details such an aspect.

The definition of both the reference plane in Pronghorn and the nested SAM branch component is taken such that the coupling framework is designed to preserve the physical conditions only at the E_i interfaces within the coupled region. Therefore, the distributions across the one-dimensional SAM components C_i are, in fact, irrelevant. Next, Sections 5.2.2. and 5.2.5. detail the physical formulations for momentum and energy, respectively, that satisfy this condition.

5.2.2. Momentum and Mass Conservation

This section derives the formulae implemented in BlueCRAB to achieve momentum coupling between the two codes. The correction to its original version is identified and disucussed throughout the derivation process.

5.2.3. Navier-Stokes Governing Equations

The first step in this process is to to state the governing equations in the two codes. Eqs. 77 and 78 present the mean momentum governing equations in Pronghorn (Ref. [81]) and SAM (Ref. [78]), respectively. On top of that, both codes also implement mass conservation steeming by continuity constituting the Navier-Stokes governing equations.

$$\frac{\partial \rho \boldsymbol{u_D}}{\partial t} + \nabla \cdot \left(\frac{\rho}{\gamma} \boldsymbol{u_D} \otimes \boldsymbol{u_D} \right) = \nabla \cdot \left(\mu \nabla \frac{\boldsymbol{u_D}}{\gamma} \right) - \gamma \nabla p + \gamma (\boldsymbol{F_g} + \boldsymbol{F_f}) \tag{77}$$

Where ρ is the fluid density, γ is the porosity, μ is the dynamic viscosity, p is the pressure, and $\boldsymbol{u_D}$ is the friction velocity ($\boldsymbol{u_D} = \gamma \boldsymbol{u}$, being u the interstitial velocity). The set of equation in Pronghorn realize not only turbulent-viscous effects, but also more complex dimensional flow effects existing in the simulation domain.

$$\rho \frac{\partial u}{\partial t} + \rho \frac{\partial u}{\partial z} = -\frac{\partial p}{\partial z} - \frac{f}{D_h} \frac{u|u|}{2} - g \tag{78}$$

Where u represents the velocity, z arbitrarily defines a reference system for the flow direction, and D_h is the hydraulic diameter. Compared to Pronghorn, SAM formulates a simplified, one-dimensional description of turbulent-viscous effects using the Darcy friction factor f. This parameter relies on a large number of closure correlations typically based on experimental data to augment the simplified one-dimension framework. As a system-level, SAM is not conceived to realize dimensional flow effects. The next section presents how the overlapping domain coupling can extend the application of SAM to account for this effects.

5.2.4. Coupling Formulations

The overlapping domain approach propose emulating multidimentional effects in a SAM model by computing friction factors based on the results of a concurent Pronghorn simulation. For each C_i overlapping component in the SAM model (see Fig. 71), BlueCRAB implements a friction factor f similarly to what has been proposed in Ref. [5]:

$$\begin{aligned} f_i &= 2\frac{D_{h,i}A_i^2}{L_i}\frac{\Delta P_i'}{\dot{m}_{E,i}\dot{v}_{E,i}} \\ \Delta P_i' &= d[(P_{E,i} - P_{ref}) + (p_{B,i} - p_B)] \end{aligned} \tag{79}$$

Herein, the subscripts i and E indicate the index of an overlapping component and that the physical quantity is computed at a coupled SAM-Pronghorn interface, respectively. On top of that, the parameter d assigns the appropriate order of substraction of the pressure difference terms based on a convetion depending on the flow direction in each coupled component. Specifically, $d = 1$ if the direction of the flow points towards the branch component and $d = -1$ otherwise. Further, $\Delta P'$ is a coupled pressure drop, whereas $\dot{v}_{E,i}$ and $\dot{m}_{E,i}$ are respectively mass and volume flor rates computed by SAM. The coupled pressure drop is composed of two terms. The first one accounts for the pressure difference between the inlets/outlets of the coupled Pronghorn domain (i.e., $P_{E,i}$) and the arbitrarily defined reference plane (P_{ref}). The second term reduces the pressure variations due to velocity changes caused by either uneven flow splits or areas changes accross inlets/outlets of the nested SAM branch component (i.e., $p_{B,i}$) and the pressure at the branch itself (i.e., p_B). Lastly, A_i and L_i consist of the flow area and the lenght of the SAM components, respectively.

Clearly, this correlation corresponds to the Darcy–Weisbach equation (i.e., the second term in the right hand side of Eq. 78). The reader is reffered to Ref. [5] for a detailed interpretation of this formulation. One may notice however that the current equation is slightly different from what previously defined. The former formulation proposed to compute friction factors solely based on Pronghorn results. However, SAM—as the majority system-level codes—implicitly computes this parameter at run time toghether with other variables, particularly the velocity. We observed that such deficiency lead to unrealistic contributions of momentum convection in the case of compressible flows.

As a correction to this problem, the current implementation utilizes the SAM mass flow rates of component C_i at the latest time-step. Altough this adaptation still treats the velocity variable explicitly from the SAM simulation perspective, the results in Section 5.4. confirms the success of such an approach.

Careful attention is required when employing the multidimensional-based friction factor from Eq. 79 due to fundamental limitations [5]. Specifically, this equations is only appropriate at steady-state conditions while the pressure drops computed by Pronhorn ΔP_i includes acceleration effects (i.e., the first term of the left-hand side in Eq. 77), whereas SAM also accounts for this term (i.e., same term from Eq. 78). This situation leads to overestimated values of pressure drops in SAM overlapping components C_i, which does not preserve the values at the interfaces between the two codes. This same logic is also applicable to gravitational effects.

BlueCRAB implementation prevents this condition while performing transient analysis by performing Picard iterations that corrects the friction factors until the pressure drops in both SAM and Pronghorn converges to each other according to a suficiently small tolerance η. The following equation dictates this process at each n iteration:

$$f_i^{(n)} = f_i^{(n-1)} + r\frac{2D_{h,i}A_i^2}{L_i}\frac{\Delta P_i^{(n)} - \Delta p_i^{(n)}}{\dot{m}_{E,i}\dot{v}_{E,i}} \tag{80}$$

Where $r = [0, 1]$ is a relaxation factor that controls the convergence process of the Picard iterations. The term $\Delta P_i = d[P_{E,i} - P_{ref}]$ of the coupled Pronghorn domain and the pressure at a reference plane, while $\Delta p_i = d[p_{B,i} - p_B]$ represents the pressure drop across the component onto which the multidimensional ΔP_i is projected.

5.2.5. Energy Conservation

BlueCRAB couples SAM and Pronghorn for energy transport similarly to the approach Section 5.2.2. proposes for momentum. This time, the multidimensional Pronghorn simulation retrieves an energy balance over an overlapping coupled region for which the system-level SAM simulation receives as a volumetric source term. Following the logic of Eq. 79 that incorporates pressure drops from Pronghorn into a multidimensional-based friction factor, Eq. 81 computes a heat source term for each SAM component C_i that preserves the energy balance of its corresponding multidimensional overlapping domain.

$$q_i''' = \frac{d[\dot{m}_{B,i} H_{ref} - \dot{m}_{E,i} H_{E,i}]}{A_i L_i} \tag{81}$$

Where d has been previously stated as the convention defining the flow direction, thus ensuring the correct order of substraction. Again, $\dot{m}$ is the mass flow rate of SAM components either at the branch connection (i.e., subscript B) or at the coupling interface (i.e., subscript E). The numerator computes an energy balance using enthalpies values computed by Pronghorn at the reference plane (H_{ref}) and at the coupling interfaces ($H_{E,i}$). The denominator represents the volume of the corresponding SAM component C_i for which this a heat balance is taken (see Fig. 71). Finally, the ratio computes the volumetric heat source q_i''' that preserves the energy between SAM and Pronghorn accross their coupled simulation domains.

BlueCRAB handles transfers and coupling within the overlapping domain, assuming that any actual heat source of interest (i.e., excluding the one described in Eq. 81) such as the reactor power, is computed within the Pronghorn model. This choice is natural since. This option is natural since one may whish to account for multidimensional effects in the core region as previously discussed.

Carefful attention is required when selecting the reference plane to compute H_{ref} when coupling multiple regions unevenly heated. For instace, if a coupled simulation includes the core and a riser region over two different SAM components C_i, a poor choice of reference plane could lead to unrealistic heating in some of components that are not aligned accordingtly. At the same time, the amount of heat may also cause the underestimated volumetric heat sources for components.

To prevent this situation, the analyst using BlueCRAB must ensure that the reference plane does not incorporate heating effects into SAM components not intended to experience such effects. In the example of modeling the riser and the core as two coupled regions, the reference plane should be located upstream of the core inlet during normal operation. This same choice also satisfies conditions involving flow reversal; in this case, the plane is located downstream of the core inlet. This condition was not previously considered such that users of BlueCRAB should receive a warning message while not satisfying this requirement.

The application of Eq. 81 for coupling energy faces similar limitations as using Eq. 79 for momentum coupling. Specifically, it is only valid under steady-state conditions because the energy balance computed by Pronghorn (i.e., the numerator of Eq. 81) includes thermal inertia effects, which are also accounted for in the SAM coupled simulation. Hence, BlueCRAB implements Eq. 82 for correcting the coupled volumetric heat sources until the energy balance in both SAM and Pronghorn converges to a same value according to a sufficiently small tolerance η. This approach is equivalent the process proposed by Eq. 80 while dealing with momentum coupling.

$$q_i'''^{(n)} = q_i'''^{(n-1)} + r\frac{\dot{H}_i^{(n)} - \dot{h}_i^{(n)}}{L_i A_i} \tag{82}$$

Where $\dot{H}_i^{(n)} = d[\dot{m}_{B,i}^{(n)} H_{ref}^{(n)} - \dot{m}_{E,i}^{(n)} H_{E,i}^{(n)}]$ and $\dot{h}_i^{(n)} = d[\dot{m}_{B,i}^{(n)} h_{ref}^{(n)} - \dot{m}_{E,i}^{(n)} h_{E,i}^{(n)}]$ are the energy balance accross overlapping regions in Pronghorn and SAM, respectively. On top of that, BlueCRAB also implements a quasi-Newton method to improve the convergence process of energy coupling. For a detailed description of its implementation, the reader is referred to Ref. [5].

5.2.6. Flow Reversal Logic Controller

Handling flow reversal is another application that deserves attention while performing safety analysis in different concepts of advanced nuclear reactors. For instance, thermal stratification and mixing effects in pool-type Lead Fast Reactors (LFRs) can lead to flow oscillations and even changes in flow direction. This phenomenon is well known and has been extensively tested at the Thermal-Hydraulic ADS Lead Bismuth Loop (TALL)-3D facility [82, 83] to support the development and validation of numerical models.

Another example involves Pressurized Loss of Forced Circulation (PLOFC) events in High-Temperature Gas-cooled Reactors (HTGRs). These transients are characterized by the loss of forced convection in the gas coolant, followed by a transition to natural circulation and subsequent flow reversal [84]. These two examples provide compelling reasons to extend BlueCRAB's capabilities to include support for flow reversal.

The key aspect for enabling flow reversal support when coupling SAM and Pronghorn is to satisfy the transfer structure indicated in Fig. 70. Namely, the BC at the inlet of Pronghorn receives the velocity corresponding to the mass flow rates from the SAM simulation, while the outlet BC receives a pressure value. It is essential to maintain this sequence to prevent the Pronghorn simulation from becoming ill-posed, which could lead to diverging convergence that violate mass conservation.

Pronghorn can prevent this situation with newly implemented switchable inlet and outlet BCs objects, named "`WCNSFVSwitchableInletVelocityBC`" [85] and "`INSFVSwitchableOutletPressureBC`" [86], respectively. Both objects are activated or deactivated during runtime depending on a boolean parameter "`switch_bc`". In coupled simulations, this parameter is dynamically adjusted based on the flow rates, which can be defined via "`BoolFunctionControl`", thus enabling the appropriate sequence of BCs as illustrated in Fig. 70.

Tab. 28 describes the implementation of the switchable BCs for pressure and velocity. The scalar f or vector $\boldsymbol{f}$ corresponds to a Dirichlet BC definition. The direction of u_{SAM} is aligned with the SAM simulation's coordinate system and $\boldsymbol{n}$ is the unit normal vector to the boundary.

Table 28. Implementation of switchable BCs in a coupled Pronghorn-SAM coupled simulation.

Object	Input	Implementation
"`BoolFunctionControl`"	SAM velocity Postprocessor value u_{SAM}	$u_{SAM} \geq 0 \rightarrow$ `switch_bc=true` `switch_bc=false, otherwise`
"`WCNSFVSwitchableInletVelocityBC`"	Result of "`BoolFunctionControl`"	`switch_bc=true` $\rightarrow \boldsymbol{u} = \boldsymbol{f}$ `switch_bc=false` $\rightarrow \nabla \boldsymbol{u} \cdot \boldsymbol{n} = 0$
"`INSFVSwitchableOutletPressureBC`"	Result of "`BoolFunctionControl`"	`switch_bc=true` $\rightarrow P = f$ `switch_bc=false` $\rightarrow \nabla P = 0$

In coupled simulations, the Pronghorn model consider both "`WCNSFVSwitchableInletVelocityBC`"

and "`INSFVSwitchableOutletPressureBC`" at each boundary interface. Only one of them is enabled at runtime, depending on the SAM flow direction as described in Tab. 28. Section 5.3.3. details the test case of a pump-driven loop in which the flow alternates circulation between clockwise and counter-clockwise. This setup employes the switchable BCs and the controling logic presented here. While this report details the implementation and use of these BCs, BlueCRAB users are not required to implement the full set of objects described in Table 28, as an option should automatically implement this logic with its constraints.

5.3. Test Cases and Simulation Details

This section presents the cases developed for testing the application proposed in Section 5.2.. Each case has its own complexity level and is carefully defined to demonstrate that BlueCRAB can attain its scope of application.

5.3.1. Isothermal Pipe Flow Tests

Horizontal pipe flow simulations were carried out in consideration of both incompressible and compressible fluids—using not only a coupled Pronghorn-SAM simulation, but also standalone calculations stemming from each the two codes. The test cases were chosen such that simple analytical hand calculations could be employed to verify the accuracy of the numerical predictions. Fig. 72 schematically presents the three types of simulations considered in analyzing the proposed tests.

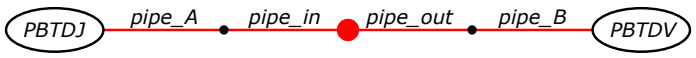

(a) SAM standalone pipe model.

(b) Pronghorn standalone pipe model.

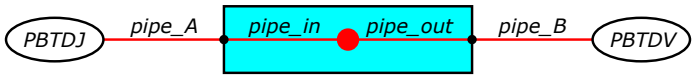

(c) SAM-Pronghorn coupled model.

Figure 72. Schematics showing the standalone and coupled models used to simulate the isothermal pipe flow test cases.

The flow condition is defined based on BCs in the SAM model. Specifically, the PBTDJ and PBTDV BC components in SAM defines the inlet velocity and the outlet pressure, respectively. Further, all simulations consider a total length of L. In the coupled simulations, the overlapping region extends over $L/2$ and is located at the center of the domain.

Tab. 29 presents the parameters defining the first test. Water enters a pipe with a fully developed profile. This condition is implicitly assumed by the SAM model while it does not include entrance effects unless specified by the user through appropriate form loss coefficients. Differently, the Poiseuille velocity profile (Eq. 83) prescribes the inlet in the case of Pronghorn models, regardless of whether it is a standalone or a coupled simulation.

Data	Symbol	Description	Values and units
Water properties	ρ	Density	$996.6\,kg/m^3$
	μ	Dynamic viscosity	$8.5E-4\,Pa\cdot s$
Pipe geometry	D	Diameter	$2.0\,cm$
	L	Total length	$4.0\,m$
Flow conditions	U	Bulk inlet velocity	$0.05\,m/s$
	Re	Reynolds number	$1,172$

Table 29. Incompressible pipe flow parameters.

$$u(r) = 2U\left[1 - \left(\frac{r}{R}\right)^2\right], \tag{83}$$

where U is the bulk velocity at the inlet, R is the pipe diameter, and r is the radial distance from the pipe centerline.

In the second test, helium enters a pipe with an outlet at low pressure, which ensures a Reynolds number of roughly $Re = 400$ at the inlet, along with compressible effects throughout the entire length of the pipe. Again, Eq. 83 prescribes the inlet of the Pronghorn simulations such that no entrance effects are considered here. Tab. 30 presents the parameters for the definition of this test.

Table 30. Compressible pipe flow parameters.

Data	Symbol	Description	Values and units
Helium properties	M	Molar mass	$4E-3\,kg/mol$
	μ	Dynamic viscosity	$3.2E-5\,Pa\cdot s$
Pipe geometry	D	Diameter	$10.0\,cm$
	L	Total length	$4.0\,m$
Flow conditions	$\dot{m}_{He}$	Mass flow rate of helium	$1.015\,mg/s$
	P_{out}	Outlet pressure	$1000\,Pa$
	V_{in}	Inlet velocity	$78.0\,m/s$
	Re	Inlet Reynolds number	400
	T	Temperature (isothermal)	$300\,K$

In the case of laminar incompressible flows, it is trivial to obtain analytical hand-calculated reference values were obtained using the Darcy-Weisbach equation, which computes the pressure drop ΔP across a length L of pipe:

$$\frac{\Delta P}{L} = f\frac{\rho}{2}\frac{U^2}{D_h}, \tag{84}$$

where $f = 64/Re$ is the Darcy friction factor, ρ is the fluid density, and U is the mean flow velocity across the cross-section area a with hydraulic diameter value D_h.

Regarding the compressible setups, we compared our numerical predictions by employing an analogy based on incompressible flows. To aid in that task, Eq. 85 establishes a relation between the mass flow rate of an isothermal compressible laminar flow $\dot{m}$ (Tab. 30) and an equivalent mass flow rate $\dot{m}_e$ obtained while assuming incompressibility that would produce the same pressure drop (i.e., $\Delta P = P_{out} - P_{in}$, where P_{in} and P_{out} are inlet and outlet pressures, respectively):

$$\dot{m}_e = \frac{\dot{m}_{He}}{2}\left(1 + \frac{P_{in}}{P_{out}}\right) . \tag{85}$$

The derivation to obtain such formulae—along the corresponding underlying assumptions—can be found in Ref. [87]. For the sake of brevity, it is not presented here.

The equivalent mass flow rate $\dot{m}_e$ serves as a reference value for an analogous mass flow rate $\dot{m}_a$ computed based on the numerical predictions. The first step to obtain such quantity is to obtain an analogous average velocity U_a that represents a laminar incompressible flow:

$$U_a = \frac{\Delta P\, D_h^2}{32\,\mu\, L} , \tag{86}$$

where μ is the dynamic viscosity. One can easily derive Eq. 86 using the Darcy-Weisbach equation (Eq. 84) such that U_a can be computed using the pressure drop ΔP obtained from the numerical simulation dealing with a compressible flow. Hence, the analogous mass flow rate $\dot{m}_a$ can be obtained as:

$$\dot{m}_a = \bar{\rho} U_a A , \tag{87}$$

where $\bar{\rho}$ is the aritimetic average density considering the inlet and the outlet and A is the cross-section area. Note that ρ_{in} can be easily determined in this analysis by assuming that the compressible fluid is an ideal gas for which the inlet temperature is a known parameter.

Ultimately, the analogous mass flow rate $\dot{m}_a$ obtained using the numerical models should closely match the equivalent mass flow rate $\dot{m}_e$ if the numerical models are accurate. Therefore, the result section evaluates both the absolute and the relative differences between these quantities to demonstrate that the developed numerical models are accurate.

Finally, for comparisons proposed in the isothermal tests of this section, Tab. 31 offers a hand calculation guide in order to ensure the accuracy of the numerical models, depending on whether the simulated flow is incompressible or compressible.

Table 31. Hand calculation guide for the verification of canonical stationary test cases.

Flow type	Simulation results of interest	Hand calculation & verification
Incompressible	ΔP	Direct comparison: Eq. 84 $\rightarrow \Delta P$
Compressible	$P_{in,out}$	Analogy comparison: Eq. 85 $\rightarrow \dot{m}_e(P_{in,out})$ Eq. 87 $\rightarrow \dot{m}_a(P_{in,out})$

5.3.2. Heated Pipe

Here, we extend the incompressible pipe test from Section 5.3.1. to include heat flux on the surface of the Pronghorn model. The governing parameters for fluid flow are the same as those defined in Tab. 29. Further, the BCs are the same as previously defined with a constant power of $\dot{q} = 2\,kW$ (i.e., roughly $q'' = 8.0\,kW/m^2/$ as shown in Fig. 73.

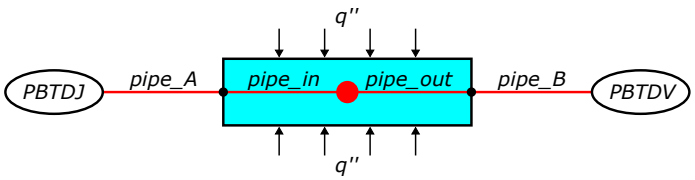

Figure 73. Schematics showing the SAM-Pronghorn coupled model used to simulate the heated pipe test case.

The temperature is initialized with a fixed value of $T = 300\,K$. We compare the predictions between SAM and Pronghorn to check if the SAM simulation retrieves the development of the the thermal boundary realized by Pronghorn. On top of that, we compare the temperature rise once the simulation reaches steady-state using a simple analytical hand calculation given by Eq. 88 as part of a verification exercise. Finally, the verification for momentum coupling is proven similarly to the incompressible pipe case detailed in Section5.3.1., as the same flow parameters were used.

$$\Delta T = \frac{\dot{m} C_p}{\dot{q}} \tag{88}$$

5.3.3. Oscilating Pump-Driven Loop

We test the flow reversal implementation proposed in Section 5.2.6. with a simple isothermal pump-driven loop. Fig. 74 presents the schematic setup of this test case. The loop is rectangular with a height of $300D$ and a width of $75D$, being $D = 2\,cm$ the diameter of its circular cross section. This configuration is chosen to ensure that friction losses are dominant, thus neglecting any form losses in the bends or pump components.

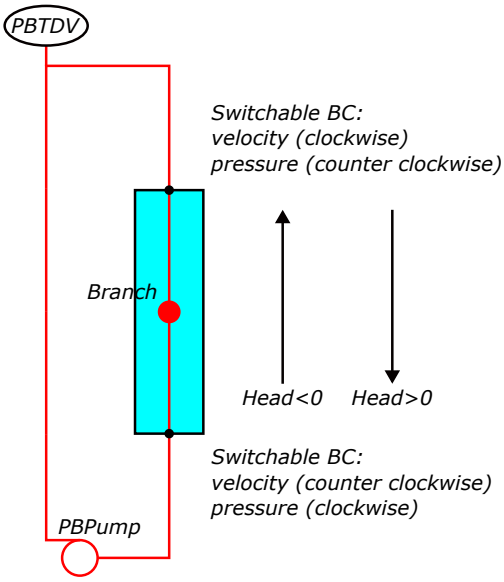

Figure 74. Schematics showing the SAM-Pronghorn coupled model used to simulate the isothermal pump-driven loop test case.

Tab. 32 presents the controling parameters of the pump-driven test case. A step function controls the pump head in the PBPump component causing the flow to circulate in both clockwise and counterclockwise directions. Similar to the schematics proposed in Fig. 72c, an overlapping region extends through $150D$, i.e.,

half of the vertial pipe length. The switchable BCs defined in Section 5.2.6. are employed to account for changes in the flow directions depending on the pump head operation. Here, both inlet velocity and pressure outlets are treated as a homogenized single values.

Table 32. Incompressible pipe flow parameters.

Data	Symbol	Description	Values and units
Water properties	ρ	Density	$996.6\,kg/m^3$
	μ	Dynamic viscosity	$8.5E-4\,Pa\cdot s$
Loop geometry	D	Diameter	$2.0\,cm$
	H	Total length	$75D = 1.5\,m$
	W	Total length	$300D = 6.0\,m$
	L	Total length	$2(H+W)D = 15.0\,m$
Flow conditions	H_p	Alternating pump head	$34\,Pa$
	T	Period of oscilation	$12\,min$
	Re	Peak Reynolds number	$1,172$

Section 5.4.3. presents results demonstrating that the proposed setup ensures the flow remains within laminar conditions (i.e., $Re \leq 1,172$). This simplification is convenient, as it reduces the modeling requirements while still retrieving the effects of flow reversal.

5.3.4. High-Temperature Reactor-Pebble-bed Module (HTR-PM)

The High-Temperature Reactor-Pebble-bed Module (HTR-PM) is a helium-cooled modular demonstration reactor design from China. This concept is primarily based on scaled up version of the also Chinese HTR-10 [88] and the former German Pebble-Bed Reactor (PBR) program experiences [89], both of which were successful campaigns. Currently, there are two operating HTR-PM units at the Shidao Bay nuclear power plant in China. Each of its units contains a pebble-bed core that generates up to 250 MW_{th} connected to its own steam generator.

Fig. 75 shows an overview of the reactor and main components. The photograph shows details during the instalation of graphite internals, which has been completed in 2017 [6]. Specifically in this photo, the central circular opening is the refulling channel whereas the surrounding ones are part of the control rod system.

Current efforts at INL support the Nuclear Regulatory Commission (NRC) in developing modeling approaches for analyzing non-LWRs [9]. In this context, BlueCRAB is employed to perform multi-physics simulations of an HTR-PM unit [9]. We seek developing a model to perform simulations that account for heat conduction within solid materials, conjugate heat transfer—including convection as well as thermal radiation—and neutron transport throughout the core. To model all these aspects, BlueCRAB leverages both SAM and Pronghorn to simulate fluid flow and heat transport while Griffin performs equilibrium core calculations.

Fig. 76 depicts the HTR-PM Pronghorn model. The model is axisymmetric, with the rotation axis indicated by the dashed vertical line. The computational domain spans $2,404$ degrees of freedom and it is built on a structured mesh with 860 elements. Cold coolant flows upward through the riser channel before entering the upper plenum, where it is distributed into the cavity, upper reflector, and rod control channels. Helium enters the active core from the upper cavity. The hot gas exiting the active region is then mixed with a core bypass fraction within both the lower plenum and reflector. Finally, the heated coolant exits the Pronghorn model at the outlet BC.

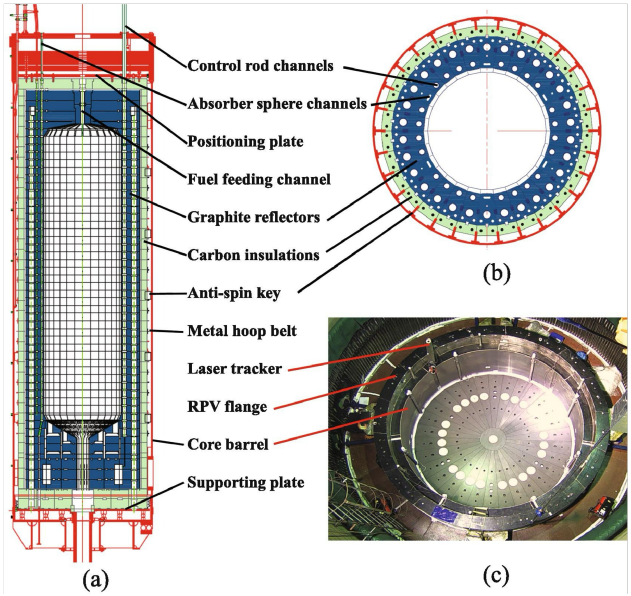

Figure 75. Structure of the internal in HTR-PM, (a) Vertical view, (b) Section view of the side reflectors, (c) Top view of the internals (reproduced from Ref. [6])

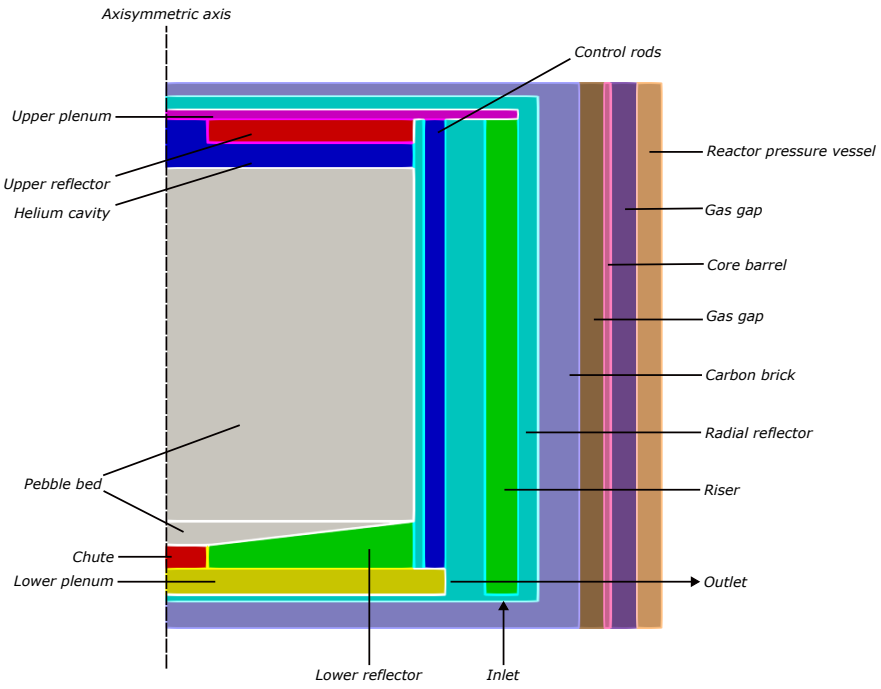

Figure 76. Pronghorn model of an HTR-PM unit (image horizontally scaled by a factor of 5 for improved visualization).

The present HTR-PM Pronghorn model is similar to the one developed in Ref. [9], with some enhancements. The modifications are not discussed here for brevity while this work focus on coupling this model with the remaining loop piping and components using SAM. For this same reason, the fission power is prescribed as a heat source in Pronghorn whereas the proposed setup is not coupled with Griffin.

BlueCRAB couples Pronghorn with SAM to model the remaining components of the HTR-PM primary loop, including the steam generator, blower, and other piping components. SAM uses its one and zero-dimensional components to model the loop system. The SAM setup employed here is largely based on the model developed on Ref. [90], but adapted to couple the Pronghorn model from Fig. 76 using the overlapping domain approach described in the present work.

Fig. 77 shows the SAM-Pronghorn model of an HTR-PM unit, developed as a demonstration case for testing the implementation of domain overlap coupling in BlueCRAB. Tab. 33 presents the design specifications considered for developing this model. As noted, two one-dimensional SAM components emulates the flow and heat transfer effects that the Pronghorn simulation retrieves. The model schematics shown in Fig. 77 presents a sample of the fluid temperature distribution within each model at steady state during normal operation.

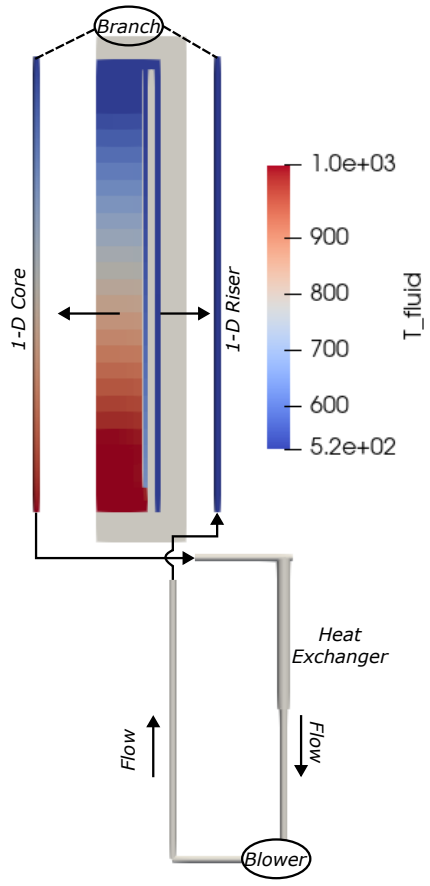

Figure 77. Schematics of the coupled model (SAM overlapping components are exploded).

Table 33. Main core parameters used in Pronghorn model (Ref. [9]).

Parameter	Values and units
Core power	250 MW_{th}
Core inlet temperature	523.15 K
Core outlet temperature	1023.15 K
Core outlet pressure	7.0 MPa
Pebble-bed radius	1.5 m
Pebble-bed height	11.0 m
Reflector outer radius	12.5 m
Barrel outer radius	2.69 m
Bypass outer radius	1.69 m
Number of pebbles	420,000
Pebble packing fraction	0.61

5.4. Results

5.4.1. Canonical Tests Results

Tabs. 34 and 35 compare the simulation results with the reference hand-calculated values indicated in Tab. 31. All the simulations were in close agreement with the reference values, demonstrating their accuracy.

Table 34. Verification of the incompressible isothermal test.

Method	ΔP $[Pa]$	$\epsilon_{rel} = 100 \times \frac{\Delta P - \Delta P_{Darcy}}{\Delta P_{Darcy}}$
Analytical solution ΔP_{Darcy} (Eq. 84)	1.36	0
SAM (Fig. 72a)	1.36	$2.4E-9\%$
Pronghorn (Fig. 72b)	1.36	-0.2%
SAM-Pronghorn (Fig. 72c)	1.36	$-5.5E-2\%$

In the case of incompressible flow (i.e., Tab. 34), the SAM pressure drop matches the correlation within the error tolerance of the solver. This is agreement is expected since the SAM code implements the Darcy friction factor, the same analytical solution considered by Eq. 84. Pronghorn computes a pressure drop with a relative error of -0.2% compared to the analytical value. Such a descrepancy is also expected and is largely explained by discretization errors. Lastly, the coupled SAM-Pronghorn prediction, which encompasses both modeling strategies and their effects, aligns with the standalone model's results. In any case, the lower prediction error obtained by the coupled model in comparison to the Pronhorn standalone simulations should not be incorrectly interpreted as an improvement, but rather as a casual combination of the individual standalone modeling effects just described.

Regarding the compressible isothermal flow test case, Tab. 35 shows that the SAM standalone simulation slightly under estimate the analogous mass flow rate $\dot{m}_a$ (Eq. 87) in comparison to the equivalent mass flow rate $\dot{m}_e$ (Eq. 85), which serves as a reference value. This results is potentially explained since SAM incorporates pressure values into the fluid equation of state model for all its primitive variables. As a consequence, a SAM standalone simulation is prone to slight reductions in pressure values as energy dissipates through the

Table 35. Verification of the compressible isothermal test.

Result	Description	SAM (Fig. 72a)	Pronghorn (Fig. 72b)	SAM-Pronghorn (Fig. 72c)
m_e	Equivalent mass flow rate (Eq. 85)	$1.032\,mg/s$	$1.032\,mg/s$	$1.032\,mg/s$
m_a	Analogous mass flow rate (Eq. 87)	$1.025\,mg/s$	$1.030\,mg/s$	$1.031\,mg/s$
$\epsilon_{\%}$	Analogy rel. error $100 \times \left(\frac{\dot{m}_a - \dot{m}_e}{\dot{m}_e}\right)$	-0.6%	0.1%	0.1%
N	Mass deviation $100 \times \left(1 - \frac{\dot{m}_{He}}{\dot{m}_e}\right)$	1.64%	1.64%	1.64%

streamwise direction. In contrast, the CFD simulation is governed by the weakly compressible version of the NS equation, preventing property variations due to dissipation effects. Again, the SAM-Pronghorn coupled simulation should account for both modeling aspects, as was previously highlighted when discussing the results from Tab. 34.

5.4.2. Heated Incompressible Pipe

Fig. 78 presents the temperature evolution at the outlet interface of the coupled section in the heated pipe test (Fig. 73). The temperatures in both Pronghorn and SAM simulations are initizalied at $T = 300\,K$ whereas the streamwise velocity as a constant value of $0.05\,m/s$. The Pronghorn model retrieves the development of both the momentum and thermal boundary layers during heat-up due to the imposed heat flux until the outlet temperature reaches a steady value of $330.55\,K$.

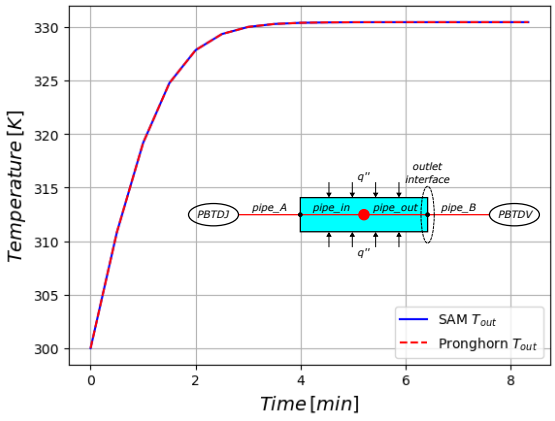

Figure 78. Temperature values evolution at the outlet interface of coupled heated pipe Pronghorn-SAM simulation.

The coupled simulation is carried out using the interative scheme proposed by Eqs. 80 and 82—for matching momentum and energy, respectively—since its initialization. Fig. 78 shows that the temperature predictions at the outlet interface of the two simulations are in good agreement throughout the entire transient. These results confirms that the proposed schemes leads to "self-consistent" predictions [5], even after the

modifications implemented here. At steady state, the coupled outlet temperatures match the analytical value computed based on the energy balance using Eq. 88, with less than a 0.2% relative difference.

5.4.3. Pump-Driven Loop Results

Fig. 79 presents results of the Pronghorn-SAM simulation for the pump-driven loop test case (Fig. 74). The flow conditions in the loop are defined according to the specifications in Tab. 32. The dashed line in the plot shows the prescribed variation in the pump head, which is implemented as a step function, with values provided on the right-side axis. The left-side axis represents the loop velocity, depicted by the solid blue line. Finally, the plot also includes an schematics showing the reference orientation system of the loop. Specifically, the reference system assumes a clockwise circulation as the positive direction and the counter clockwise as negative.

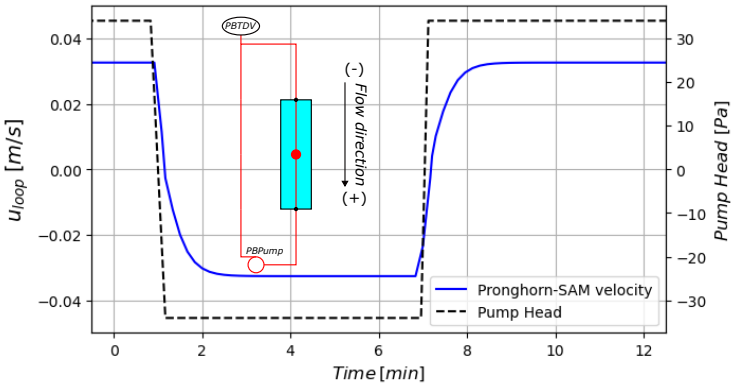

Figure 79. Schematics showing the standalone and coupled models used to simulate the heated pipe test cases.

The results in Fig. 79 show that flow circulation computed by the coupled Pronghorn-SAM simulation responds accordingtly to the head variations. The maximum Reynolds number after each reversal is $Re = 1,172$ causing the flow to become the same as the incompressible pipe test case (Tab. 29). At this condition, the pressure gradient cross the piping components closely match the analytical values obtained with Eq. 84 (see Tab. 34). Thus, the results of the pump-driven test case demonstrate the adequacy of the implementation for flow reversal support in BlueCRAB when coupling SAM and Pronghorn.

5.4.4. High-Temperature Reactor-Pebble-bed Module (HTR-PM) Demonstration

This section presents the results obtained with the coupled HTR-PM model for transients during a normal ramp-up and coastdown of reactor power. We assume that both transients occur over approximately 8 hours, with the power linearly increasing during ramp-up and then decreasing during coastdown.

Fig. 80 presents the numerical predictions over the overlapping coupled region (Fig. 77). The riser inlet and the lower plenum outlet corresponds to the coupling interfaces between SAM and Pronghorn (see schematics from Fig. 77). Specifically, Fig. 80a shows the evolution of the pressure drop computed between these two boundaries whereas Fig. 80b presents the development of their temperature values.

Both plots compare the simulation results obtained by SAM and Pronghorn. The temperature in both simulations is initizalied at $T = 523.15\,K$ defined as the core inlet temperature (Tab. 33). Further, the flow is initialized as stagnant with no power in the core region of the Pronghorn model.

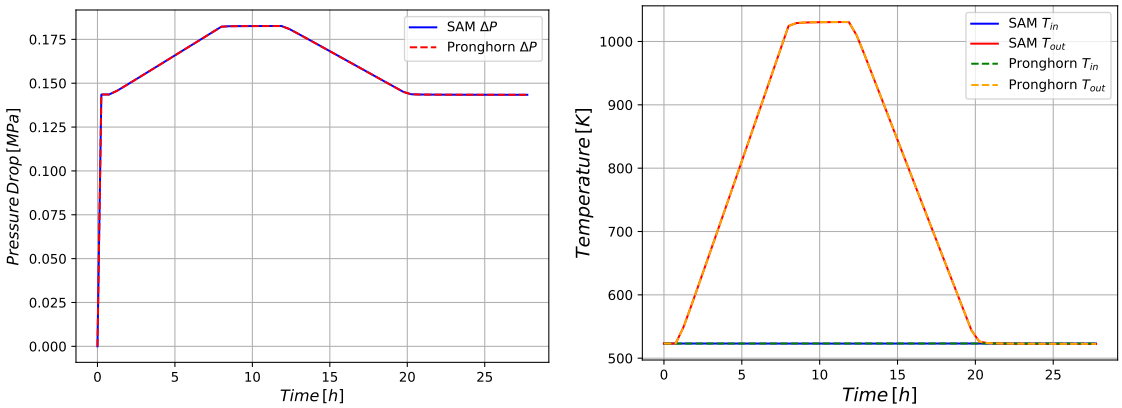

(a) Evolution of coupled pressure drop.

(b) Evolution of coupled temperatures.

Figure 80. Power ramp-up and costdown results.

Stating at its initialization, the coupled simulation employs the iterative scheme defined in Eqs. 80 and 82, thus ensuring "self-consistent" predictions [5] throughout the entire run for both momentum and energy, respectively.

The first simulated hour only consider fluid flow driven by the blower while not including any power source within the core. This stage ensures the flow to fully develop throughout the loop. Following that, the power in the core region increases linearly along 8 hours up to 250 MW_{th} according to a prescribed heat source. After this process, the outlet temperatures in both SAM and Pronghorn rise to 1030.69 K, with a pressure of 7.0 MPa, while the core inlet temperature remains relatively stable.

The power and coolant flow rate remain at nominal values for the next 4 hours. The numerical predictions during this period demonstrate that the coupled Pronghorn-SAM model of the HTR-PM unit satisfactorily predicts the design specifications proposed in Tab. 33.

At 12 hours of simulated time, the power linearly decreases to zero over 8 hours. The predicted temperature and pressure respond accordingly, returning to the original values observed during the first stage. Finally, the simulation ends 28 hours after it began.

5.5. Conclusion

The present work developed improvements and corrections to the BlueCRAB code suite, specifically to its support for multiscale coupling between Pronghorn and SAM based on a domain overlapping approach. The approach is largely based on the method introduced by Ref. [5] that enables an agnostic interface between the two codes.

First, we review and propose adaptations to the coupling momentum formulation for extending the previous implementation to address both incompressible and compressible flows. Further, we include support for handling flow reversal based on specialized set of switching boundary condition in Pronghorn which is controled by a boolean logic depending on SAM flow predictions. Finally, the original coupling implementation for energy was reviewed and corrected to ensure proper distribution of heat sources across different Pronghorn-SAM overlapping regions.

We define four verification cases and an additional demonstration one to test the proposed coupling methodology and implementation. The verification cases involve setups that are simple enough to allow for

analytical hand calculations, thus providing a comparative baseline for the numerical predictions. These cases include isothermal pipes with either incompressible or compressible flows, a heated pipe, and a pump-driven loop with flow reversal. The demonstration case involves a coupled Pronghorn-SAM simulation of an HTR-PM unit, serving as a more complex and practical application for reactor analysis. In this case, a developed coupled Pronghorn-SAM model perform predictions in good agreement with the specifications of the reference facility.

It should be noted that we adopt the HTR-PM as a demonstration case while its helium coolant impose additional challenge to the coupling formulation due to compressiblity effects. At the same time, the coupling approach also support incompressible flows such that it is also appropriate for performing analysis of MSRs.

We emphasize that all Pronghorn-SAM simulations performed in this work successfully preserved both energy and momentum across overlapping coupled regions. More importantly, no numerical instabilities were observed, which is the primary reason the NEAMS program sponsors activities entailing the overlapping domain approach rather than more traditional separate domain techniques. Ultimately, these outcomes are essential for the program to fullfill its mission of accelerating the deployment of non-LWRs.

6. WORKFLOW IMPROVEMENTS

Recent experience at user workshops has shown that many users struggle to set up models for coupled MSR problems. While the user input for MOOSE-based simulations may be relatively user-friendly compared to competing numerical software, it is critical to make the user experience as streamlined as possible to maximize the usability of the software. A particular area of difficulty is the setup of MSR simulations that couple neutronics and thermal hydraulics. This coupling necessitates the creation and interaction of various MOOSE objects and would greatly benefit from some input simplification. The recently developed `Physics` system in MOOSE provides an excellent foundation for simplifying user input. This system was leveraged to create the `MSRNeutronicsFluidCoupling` syntax.

The neutronics-fluid coupling for an MSR is achieved by the use of a `MultiApp`, where the main application is the neutronics application, e.g., Griffin, and the sub-application is the thermal fluid application, Pronghorn. This kind of multi-app setup requires the use of two input files, one for the main application and one for the sub-application. `MSRNeutronicsFluidCoupling` simplifies the coupling input for the *neutronics* input file.

The coupling model is summarized as follows. Each solve of the neutronics application produces the power density and fission source density, which are transferred to the fluids application. The fluids application produces the distribution of delayed neutron precursor (DNP) group concentrations and fluid temperature, which are transferred to the neutronics application. `MSRNeutronicsFluidCoupling` does the following (all in the neutronics application):

- Adds auxiliary variables:
  - A constant monomial variable on the fluid subdomain for each DNP group
  - A constant monomial array variable on the fluid subdomain for the array of DNP concentrations
  - A constant monomial variable on the fluid subdomain for the fluid temperature
  - A first-order Lagrange variable on the solid domain for the fluid temperature
- Adds an `AuxKernel` for the DNP concentration array variable
- Adds an `IC` for the fluid temperature variable
- Adds a `MultiApp` for the fluid application
- Adds `Transfers`
  - Power density to the fluid application
  - Fission source density to the fluid application
  - Fluid temperature from the fluid application to the fluid blocks
  - Fluid temperature from the fluid application to the solid blocks
  - Individual DNP concentrations from the fluid application

MSFR example (https://mooseframework.inl.gov/virtual_test_bed/msr/msfr/) in the Virtual Test Bed, whose mesh is shown in Figure 81, utilizes this syntax:

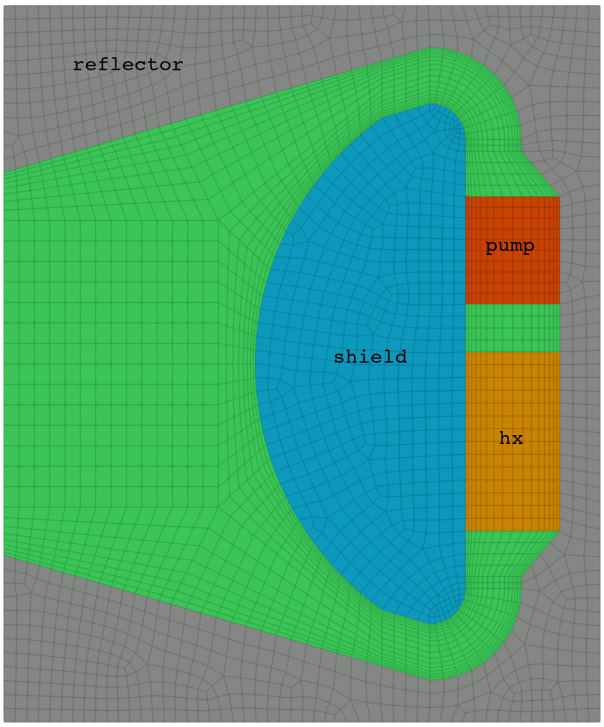

Figure 81. Mesh for the Molten Salt Fast Reactor example.

```
[MSRNeutronicsFluidCoupling]
  fluid_blocks = 'fuel pump hx'
  solid_blocks = 'reflector shield'
  n_dnp = 6
  use_transient_multi_app = false
  fluid_app_name = ns
  fluid_input_file = run_ns.i
  initial_fluid_temperature = 873.15
  fluid_temperature_name_neutronics_app = tfuel
  fluid_temperature_name_solid_suffix = _constant
  fluid_temperature_name_fluid_app = T_fluid
  dnp_name_prefix = c
  dnp_array_name = dnp
[]
```

Listing 1. MSR Neutronics-Fluid Coupling Configuration

This block of input, comprised of 14 lines, replaced 124 lines of input. Moreover, these lines are much less error-prone due to dedicated documentation via the syntax documentation page for `MSRNeutronicsFluidCoupling`, available to licensed users of Pronghorn:

https://pronghorn-dev.hpc.inl.gov/site/syntax/MSRNeutronicsFluidCoupling/index.html.

To summarize the input parameters used in the example above:

- `fluid_blocks`: The fluid blocks in the neutronics application.
- `solid_blocks`: The solid blocks in the neutronics application.
- `n_dnp`: The number of delayed neutron precursor groups.

- `use_transient_multi_app`: Whether to use a `TransientMultiApp` (else a `FullSolveMultiApp`).
- `fluid_app_name`: Name to give the fluid application.
- `fluid_input_file`: Fluid input file.
- `initial_fluid_temperature`: Initial fluid temperature function for the auxiliary variables in the neutronics application.
- `fluid_temperature_name_neutronics_app`: Name to give the fluid temperature variable in the neutronics application on the fluid blocks.
- `fluid_temperature_name_solid_suffix`: Suffix to add to `fluid_temperature_name_neutronics_app` for the fluid temperature variable in the neutronics application on the solid blocks.
- `fluid_temperature_name_fluid_app`: Fluid temperature variable in the fluid application.
- `dnp_name_prefix`: Prefix for the delayed neutron precursor variables in both the neutronics application and fluid application.
- `dnp_array_name`: Delayed neutron precursor array variable name.

Future work could yield some improvements. One improvement would be user input creating the necessary MOOSE objects for both sides of the coupling, not just the neutronics side. Currently the only way to do this would be to translate user input from a neutronics-side syntax into command-line arguments to supply to the sub-application input, which has the potential to be tedious to implement and maintain. However, the development of some infrastructure could help with this approach. An alternative to achieving a shared syntax is by having the main and sub applications interact directly to share input, but this approach would require further consideration to determine if it is feasible. If the input cannot be shared directly between applications, then it may be advantageous to at least perform some consistency checks between the applications.

7. CONCLUSIONS AND FUTURE WORK

7.1. Conclusions

This work has made significant advancements in the modeling and simulation capabilities for Molten Salt Reactors (MSRs) within the Pronghorn framework, addressing several critical thermal-hydraulic challenges that are pivotal for the safe and efficient operation of these reactors.

The integration of two-equation RANS turbulence models into Pronghorn represents a major advancement in the accurate prediction of turbulent mixing and heat transfer in MSRs. These models have been rigorously validated against experimental data, showing their capability to accurately capture the complex flow patterns that characterize the primary and secondary loops of MSRs. This advancement is crucial as turbulent mixing plays a significant role in the distribution of temperature and fission products, directly impacting reactor performance and safety.

The introduction of near-wall turbulence corrections to account for effects of wall roughness and curvature addresses a previously unmodeled complexity in MSR simulations. In MSRs, where molten salt flows interact with reactor structures, these corrections are essential for predicting the thermal-hydraulic behavior accurately. The developed corrections were validated against experimental data, including friction factor measurements and swirling flow cases, showing that they significantly improve the accuracy of predictions in near-wall regions. This work demonstrates the importance of considering such factors in the design and analysis of MSRs, where material degradation and flow-induced stresses are critical concerns.

Furthermore, the development of multidimensional two-phase drift-flux models for Pronghorn marks a substantial enhancement in the capability to model the behavior of gas bubbles within the molten salt. Gas bubbles, whether resulting from fission gas release or sparging operations, play a crucial role in influencing both the reactivity and thermal-hydraulics of the reactor. The drift-flux model developed in this work provides a more detailed and accurate prediction of void fraction distributions, which are critical for safety analyses and reactor control. Validation of this model against historical data from the Molten Salt Reactor Experiment (MSRE) demonstrates its effectiveness in capturing the complex dynamics of two-phase flow in MSRs.

Improvements in the domain-overlapping coupling between Pronghorn and SAM have addressed critical challenges related to the accurate simulation of weakly compressible flows and flow reversals in MSRs. These improvements ensure that the coupling between thermal-hydraulics and neutronics is handled with greater accuracy, reducing the likelihood of inconsistencies that could affect simulation outcomes. The enhanced coupling methodology has been validated through application to various MSR scenarios, demonstrating its effectiveness in improving the fidelity of integrated reactor simulations.

Additionally, the development of an MSR-specific action in Pronghorn significantly simplifies the process of setting up coupled MSR models. This new capability reduces the complexity of input files, allowing for more streamlined and error-free model setup, which is particularly beneficial in complex multiphysics simulations. By replacing extensive input requirements with a simplified syntax, this development enhances user accessibility and efficiency, facilitating broader adoption of Pronghorn for MSR simulations.

Collectively, these advancements push the boundaries of current MSR modeling capabilities. The work significantly enhances the accuracy and reliability of thermal-hydraulic simulations, which are essential for the design, safety analysis, and operational support of MSRs. By addressing critical challenges in turbulence modeling, near-wall effects, two-phase flow dynamics, domain coupling, and model setup, this research contributes to the development of safer and more efficient MSR technologies, positioning Pronghorn as a leading tool in the field of advanced reactor modeling.

7.2. Future Work

While this work has significantly advanced the modeling and simulation capabilities for MSRs within the Pronghorn framework, several challenges remain that require further research and development.

Future work should also focus on integrating the Saline module into the MOOSE framework to enhance the modeling of MSRs by accurately accounting for the variable thermophysical properties of molten salts. The current models in Pronghorn assume constant composition of the fuel salt, which is inaccurate as the fuel salt evolves due to depletion and impurity accumulation during MSR operation. Saline, with its capability to provide temperature-dependent and composition-dependent properties, would enable more precise simulations of heat transfer, fluid dynamics, and species transport within the reactor. By coupling Saline with existing thermal-hydraulic models in MOOSE, this integration would allow for more realistic predictions of reactor behavior, particularly in scenarios involving transient operations or non-uniform salt compositions, thereby improving the safety and efficiency assessments of MSRs.

Another critical area is the need for more sophisticated models that account for the chemical interactions between the molten salt and reactor materials, especially in the context of corrosion and material degradation. The current models primarily focus on the thermal-hydraulic aspects, but integrating corrosion kinetics and material degradation processes into the simulations could provide a more comprehensive understanding of long-term reactor behavior. This integration would be particularly valuable for predicting the lifespan of reactor components and for developing maintenance and replacement strategies.

The development of more advanced multiphase flow models is also a priority for future work. The current drift-flux models have improved the prediction of gas bubble behavior in MSRs, but there is a need for models that can better capture the interactions between multiple phases, including liquid, gas, and solid precipitates that may form under certain conditions. These models would need to account for the complex dynamics of phase change, bubble coalescence, and the impact of these processes on reactor reactivity and heat transfer.

In addition, future work should focus on enhancing the domain-overlapping coupling methodologies to include more robust and efficient algorithms for real-time simulations. As MSRs operate under highly dynamic conditions, the ability to accurately simulate transient scenarios in real-time is crucial for both safety analysis and operational decision-making. Developing faster and more scalable coupling methods that can handle the increased complexity of these simulations would be a significant step forward.

Moreover, there is a need to extend the MSR-specific action in Pronghorn to support a broader range of reactor designs and operational scenarios. While the current developments have simplified the setup for certain MSR configurations, expanding these capabilities to include more diverse reactor geometries, fuel compositions, and operating conditions will make the tool more versatile and widely applicable.

Addressing these challenges through future work will further enhance the predictive capabilities of Pronghorn, contributing to the safe and efficient deployment of MSRs.

Finally, one area for future work should be the enhancement of turbulence models for high-temperature and high-Prandtl number fluids like molten salts. The current two-equation RANS models provide a good balance between accuracy and computational efficiency, but they may not fully capture the complex turbulence structures that arise in more extreme operating conditions. Future efforts could focus on developing LES or hybrid RANS-LES models that can provide more detailed insights into turbulence phenomena at a reasonable computational cost.

8. REFERENCES

[1] J. Kim, P. Moin, and R. Moser, "Turbulence statistics in fully developed channel flow at low reynolds number," *Journal of fluid mechanics*, vol. 177, pp. 133–166, 1987.

[2] D. M. Driver and H. L. Seegmiller, "Features of a reattaching turbulent shear layer in divergent channelflow," *AIAA journal*, vol. 23, no. 2, pp. 163–171, 1985.

[3] M. Anwer, R. So, and Y. Lai, "Perturbation by and recovery from bend curvature of a fully developed turbulent pipe flow," *Physics of Fluids A: Fluid Dynamics*, vol. 1, no. 8, pp. 1387–1397, 1989.

[4] M. Fratoni, D. Shen, G. Ilas, and J. Powers, "Molten salt reactor experiment benchmark evaluation," 5 2020.

[5] S. Schunert, M. E. Tano Retamales, and M. K. Mohammad Jaradat, "Overlapping domain coupling of multidimensional and system codes in neams - pronghorn and sam," 5 2023.

[6] D. Tian, L. Shi, L. Sun, Z. Zhang, Z. Zhang, and Z. Zhang, "Installation of the graphite internals in htr-pm," *Nuclear Engineering and Design*, vol. 363, p. 110585, 2020.

[7] T. Hibiki and M. Ishii, "One-group interfacial area transport of bubbly flows in vertical round tubes," *International Journal of Heat and Mass Transfer*, vol. 43, no. 15, pp. 2711–2726, 2000.

[8] D. Shen, M. Fratoni, G. Ilas, and J. Powers, "Molten-salt reactor experiment (msre) zero-power first critical experiment with 235u," *under evaluation as MSRE-MSR-EXP-001 for inclusion in the IRPHE Handbook*, 2019.

[9] M. K. M. Jaradat, S. Schunert, and J. Ortensi, "Gas-cooled high-temperature pebble-bed reactor reference plant model," 4 2023.

[10] J. Bao, "Development of the model for the multi-physics analysis of molten salt reactor experiment using gen-foam code," *Paul Scherrer Institute, Villigen, Switzerland*, 2016.

[11] C. Fiorina, I. Clifford, M. Aufiero, and K. Mikityuk, "Gen-foam: a novel openfoam® based multi-physics solver for 2d/3d transient analysis of nuclear reactors," *Nuclear Engineering and Design*, vol. 294, pp. 24–37, 2015.

[12] K. Podila, Q. Chen, and Y. Rao, "Cfd simulations of molten salt reactor experiment core," *Nuclear Science and Engineering*, vol. 193, no. 12, pp. 1379–1393, 2019.

[13] H. Mochizuki, "Neutronics and thermal-hydraulics coupling analysis using the fluent code and the relap5-3d code for a molten salt fast reactor," *Nuclear Engineering and Design*, vol. 368, p. 110793, 2020.

[14] M. E. Tano and P. Rubiolo, "Development of explainable data-driven turbulence models with application to liquid fuel nuclear reactors," *Energies*, vol. 15, no. 19, p. 6861, 2022.

[15] A. Novak, H. Brooks, P. Shriwise, A. Hegazy, and A. Davis, "Multiphysics coupling of openmc cad-based transport to moose using cardinal and aurora," in *The International Conference on Mathematics and Computational Methods Applied to Nuclear Science and Engineering (M&C 2023). Niagara Falls, Canada*, 2023.

[16] U. Bieder, Y. Gorsse, and F. Martin, "Molten salt fast reactors: a thermal-hydraulics study with rans models and large eddy simulations," in *Proc. Proceeding of the 9th International Conference & Workshop REMOO-2019" ENERGY RELIABILITY*, 2019.

[17] D. Walter, T. Cisnero, S. Goodrich, and Z. Mausolff, "Mcre design description in support of external model development," *TerraPower (Dec. 27, 2022)*, 2023.

[18] S. A. Walker, A. Abou Jaoude, O. W. Calvin, and M. E. Tano Retamales, "Implementation of isotopic removal capability in griffin for multi-region msr depletion analysis," tech. rep., Idaho National Laboratory (INL), Idaho Falls, ID (United States), 2022.

[19] H. Matsuura, R. Takagi, L. Rycerz, and M. Gaune-Escard, "Enthalpies of mixing in molten ucl3-nacl system," *Journal of Nuclear Science and Technology*, vol. 39, no. sup3, pp. 632–634, 2002.

[20] B. Li, S. Dai, and D.-e. Jiang, "First-principles molecular dynamics simulations of ucl n–nacl (n= 3, 4) molten salts," *ACS Applied Energy Materials*, vol. 2, no. 3, pp. 2122–2128, 2019.

[21] A. Rao and K. Narender, "Studies on thermophysical properties of cao and mgo by-ray attenuation," *Journal of Thermodynamics*, vol. 2014, 2014.

[22] A. C. Victor and T. B. Douglas, "Thermodynamic properties of magnesium oxide and beryllium oxide from 298 to 1,200 k," *Journal of Research of the National Bureau of Standards. Section A, Physics and Chemistry*, vol. 67, no. 4, p. 325, 1963.

[23] S. D. I. Software, "Simcenter star-ccm+, version 2021.1," Siemens 2021.

[24] M. Tano, P. Rubiolo, and J. Ragusa, "Accuracy analysis of near wall thermal-hydraulics modeling of molten salt reactors," *18th International Topical Meeting on Nuclear Reactor Thermal Hydraulics, NURETH 2019*, pp. 2795–2808, 2019.

[25] A. J. Hutchinson, N. Hale, K. Born, and D. P. Mason, "Prandtl's extended mixing length model applied to the two-dimensional turbulent classical far wake," *Proceedings of the Royal Society A*, vol. 477, 2021.

[26] R. J. Kind, F. M. Yowakim, and S. A. Sjolander, "The law of the wall for swirling flow in annular ducts," *Journal of Fluids Engineering-transactions of The Asme*, vol. 111, pp. 160–164, 1989.

[27] C. Jayatilleke, "The influence of prandtl number and surface roughness on the resistance of the laminar sub-layer to momentum and heat transfer," 1966.

[28] R. P. King, "2 – flow of fluids in piping systems," 2002.

[29] M. Orych, S. Werner, and L. Larsson, "Roughness effect modelling for wall resolved rans – comparison of methods for marine hydrodynamics," *Ocean Engineering*, 2022.

[30] J. Jimenez, "Turbulent flows over rough walls," *Annual Review of Fluid Mechanics*, vol. 36, pp. 173–196, 2004.

[31] M. R. Kadivar, D. Tormey, and G. McGranaghan, "A review on turbulent flow over rough surfaces: Fundamentals and theories," 2021.

[32] J. Nikuradse, "Laws of flow in rough pipes," 1950.

[33] J. E. Danberg and A. Sigal, "Analysis of turbulent boundary-layer over rough surfaces with application to projectile aerodynamics," 1988.

[34] N. Kim and D. L. Rhode, "Swirling streamline-curvature law of the wall from a novel perturbation analysis," *Numerical Heat Transfer Part B-fundamentals*, vol. 36, pp. 331–350, 1999.

[35] H. Yokosawa, H. Fujita, M. Hirota, and S. Iwata, "Measurement of turbulent flow in a square duct with roughened walls on two opposite sides," *International journal of heat and fluid flow*, vol. 10, no. 2, pp. 125–130, 1989.

[36] P. Clausen, S. Koh, and D. Wood, "Measurements of a swirling turbulent boundary layer developing in a conical diffuser," *Experimental Thermal and Fluid Science*, vol. 6, no. 1, pp. 39–48, 1993.

[37] J. A. C. Humphrey and F. Pourahmadi, "Generalized algebraic relation for predicting developing curved-channel flow with a k-epsilon model of turbulence," 1981.

[38] E. Shemon, J. Fang, T. Hua, Y. Miao, N. Stauff, A. Abou-Jaoude, G. Giudicelli, V. Kyriakopoulous, M. Tano, and S. Walker, "Neams model contributions in 2023 to the national reactor innovation center virtual test bed for use by industry and other stakeholders," tech. rep., Argonne National Laboratory (ANL), Argonne, IL (United States), 2023.

[39] E. Compere, S. Kirslis, E. Bohlmann, F. Blankenship, and W. Grimes, "Fission product behavior in the molten salt reactor experiment," tech. rep., Oak Ridge National Lab.(ORNL), Oak Ridge, TN (United States), 1975.

[40] R. A. P. Dwijayanto, F. Miftasani, and A. W. Harto, "Assessing the benefit of thorium fuel in a once through molten salt reactor," *Progress in Nuclear Energy*, vol. 176, p. 105369, 2024.

[41] S. Yoo, W. Lee, and K.-Y. Lee, "A conceptual design of supercritical co2 brayton cycle for a small modular molten salt reactor," in *Transactions of the Korean Nuclea r Society Spring Meeting Jeju, Korea*, 2022.

[42] T. Kamei, "Recent research of thorium molten-salt reactor from a sustainability viewpoint," *Sustainability*, vol. 4, no. 10, pp. 2399–2418, 2012.

[43] B. M. Elsheikh, "Safety assessment of molten salt reactors in comparison with light water reactors," *journal of radiation research and applied sciences*, vol. 6, no. 2, pp. 63–70, 2013.

[44] E. Cervi, "Modeling of fission gas behavior in molten salt reactors," *Nuclear Engineering and Design*, vol. 331, pp. 345–352, 2018.

[45] P. Jr Vicente Valdez, B. R. Betzler, W. A. Wieselquist, and M. Fratoni, "Modeling molten salt reactor fission product removal with scale," tech. rep., Oak Ridge National Lab.(ORNL), Oak Ridge, TN (United States), 2020.

[46] P. N. Haubenreich and J. Engel, "Experience with the molten-salt reactor experiment," *Nuclear Applications and technology*, vol. 8, no. 2, pp. 118–136, 1970.

[47] S. Kirslis, F. Blankenship, and W. Grimes, "Fission-product behavior in molten-salt reactors.," tech. rep., Oak Ridge National Lab., Tenn., 1967.

[48] A. J. Lee and T. Kozlowski, "Effects of sparging gas entrainment on void and temperature coefficients in the transatomic power molten salt reactor core," *Annals of Nuclear Energy*, vol. 192, p. 110013, 2023.

[49] T. Price, Z. Taylor, and O. Chvala, "A review of circulating voids and gaseous fission product behavior in molten salt reactors," *Journal of Nuclear Engineering and Radiation Science*, vol. 6, no. 4, p. 041302, 2020.

[50] D. J. Diamond, N. R. Brown, R. Denning, and S. Bajorek, "Phenomena important in molten salt reactor simulations," tech. rep., Brookhaven National Lab.(BNL), Upton, NY (United States), 2018.

[51] N. R. Brown, D. J. Diamond, S. Bajorek, and R. Denning, "Thermal-hydraulic and neutronic phenomena important in modeling and simulation of liquid-fuel molten salt reactors," *Nuclear Technology*, vol. 206, no. 2, pp. 322–338, 2020.

[52] Z. Taylor, R. Salko, A. M. Graham, B. S. Collins, and G. I. Maldonado, "Implementation of two-phase gas transport into vera for molten salt reactor analysis," *Annals of Nuclear Energy*, vol. 165, p. 108672, 2022.

[53] P. Bajpai, V. La Masa, C. Introini, A. Cammi, and S. Lorenzi, "A multiphysics model for analysis of inert gas bubbles in molten salt fast reactor–part 1: Numerical modelling," in *Proceedings of the 27th International Conference Nuclear Energy for New Europe (NENE 2018)*, pp. 1–8, Nuclear Society of Slovenia, 2018.

[54] E. Cervi, S. Lorenzi, A. Cammi, and L. Luzzi, "Development of an sp3 neutron transport solver for the analysis of the molten salt fast reactor," *Nuclear Engineering and Design*, vol. 346, pp. 209–219, 2019.

[55] R. Rogers *et al.*, "Thermal-hydraulic performance of a molten salt reactor core during startup and operation," *Annals of Nuclear Energy*, vol. 99, pp. 43–53, 2017.

[56] E. Bettis, L. Alexander, and H. Watts, "Design studies of a molten-salt reactor demonstration plant.," tech. rep., Oak Ridge National Lab.(ORNL), Oak Ridge, TN (United States), 1972.

[57] T. J. Price, O. Chvala, and Z. Taylor, "Xenon in molten salt reactors: The effects of solubility, circulating particulate, ionization, and the sensitivity of the circulating void fraction," *Nuclear Engineering and Technology*, vol. 52, no. 6, pp. 1131–1136, 2020.

[58] B. M. Chisholm, S. L. Krahn, and K. N. Fleming, "A systematic approach to identify initiating events and its relationship to probabilistic risk assessment: Demonstrated on the molten salt reactor experiment," *Progress in Nuclear Energy*, vol. 129, p. 103507, 2020.

[59] G. Giustini, "Modelling of boiling flows for nuclear thermal hydraulics applications—a brief review," *Inventions*, vol. 5, no. 3, p. 47, 2020.

[60] J. Křepel, U. Rohde, U. Grundmann, and F.-P. Weiss, "Dyn3d-msr spatial dynamics code for molten salt reactors," *Annals of Nuclear Energy*, vol. 34, no. 6, pp. 449–462, 2007.

[61] N. Habtemariam, C. Fiorina, S. Lorenzi, and A. Cammi, "On the need for multi-dimensional models for the safety analysis of (fast-spectrum) molten salt reactors," *Annals of Nuclear Energy*, vol. 197, p. 110237, 2024.

[62] Z. Li and J. Cai, "Dynamics analysis of the graphite-moderated channel-type molten salt reactors based on serpent/nth3d-msr," *Annals of Nuclear Energy*, vol. 121, pp. 128–134, 2018.

[63] R. Hu, J. Fang, D. Nunez, M. Tano, G. Giudicelli, and R. Salko, "Development of integrated thermal fluids modeling capability for msrs," tech. rep., Argonne National Laboratory (ANL), Argonne, IL (United States), 2022.

[64] V. Singh, A. M. Wheeler, M. R. Lish, O. Chvála, and B. R. Upadhyaya, "Nonlinear dynamic model of molten-salt reactor experiment–validation and operational analysis," *Annals of Nuclear Energy*, vol. 113, pp. 177–193, 2018.

[65] Z. Guo, J. Zhou, D. Zhang, K. S. Chaudri, W. Tian, G. Su, and S. Qiu, "Coupled neutronics/thermal-hydraulics for analysis of molten salt reactor," *Nuclear Engineering and Design*, vol. 258, pp. 144–156, 2013.

[66] D. Gaston *et al.*, "Moose: A parallel computational framework for coupled systems of nonlinear equations," *Nuclear Engineering and Design*, vol. 239, no. 10, pp. 1768–1778, 2009.

[67] J. Wu, J. Chen, X. Cai, C. Zou, C. Yu, Y. Cui, A. Zhang, and H. Zhao, "A review of molten salt reactor multi-physics coupling models and development prospects," *Energies*, vol. 15, no. 21, p. 8296, 2022.

[68] A. Lindsay, G. Giudicelli, P. German, J. Peterson, Y. Wang, R. Freile, D. Andrs, P. Balestra, M. Tano, R. Hu, *et al.*, "Moose navier–stokes module," *SoftwareX*, vol. 23, p. 101503, 2023.

[69] S. M. Bhagwat and A. J. Ghajar, "Experimental investigation of non-boiling gas-liquid two phase flow in upward inclined pipes," *Experimental Thermal and Fluid Science*, vol. 79, pp. 301–318, 2016.

[70] M. Ishii and T. Hibiki, *Thermo-fluid dynamics of two-phase flow*. Springer Science & Business Media, 2010.

[71] Z. Bilicki and J. Kestin, "Physical aspects of the relaxation model in two-phase flow," *Proceedings of the Royal Society of London. A. Mathematical and Physical Sciences*, vol. 428, no. 1875, pp. 379–397, 1990.

[72] R. K. Salko, T. Mui, L. Zou, and R. Hu, "Implementation of a drift flux model into sam with development of a verification and validation test suite for modeling of noncondensable gas mixtures," *Nuclear Technology*, pp. 1–23, 2024.

[73] T. Hibiki, M. Ishii, and Z. Xiao, "Axial interfacial area transport of vertical bubbly flows," *International Journal of Heat and Mass Transfer*, vol. 44, no. 10, pp. 1869–1888, 2001.

[74] R. Kedl, "Fluid dynamic studies of the molten-salt reactor experiment (msre) core.," tech. rep., Oak Ridge National Lab.(ORNL), Oak Ridge, TN (United States), 1970.

[75] J. Long, B. Zhang, B.-W. Yang, and S. Wang, "Review of researches on coupled system and cfd codes," *Nuclear Engineering and Technology*, vol. 53, no. 9, pp. 2775–2787, 2021.

[76] A. D. Lindsay *et al.*, "2.0 - MOOSE: Enabling massively parallel multiphysics simulation," *SoftwareX*, vol. 20, p. 101202, 2022.

[77] A. J. Novak, R. W. Carlsen, S. Schunert, P. Balestra, D. Reger, R. N. Slaybaugh, and R. C. Martineau, "Pronghorn: A multidimensional coarse-mesh application for advanced reactor thermal hydraulics," *Nuclear Technology*, vol. 207, no. 7, pp. 1015–1046, 2021.

[78] R. Hu, L. Zou, T. Mui, D. J. O'Grady, G. Hu, S. Chen, and T. Jayasankar, "Sam assessment report," 12 2023.

[79] T. Grunloh and A. Manera, "A novel multi-scale domain overlapping cfd/sth coupling methodology for multi-dimensional flows relevant to nuclear applications," *Nuclear Engineering and Design*, vol. 318, pp. 85–108, 2017.

[80] A. Huxford, V. C. Leite, E. Merzari, L. Zou, V. Petrov, and A. Manera, "A hybrid domain overlapping method for coupling system thermal hydraulics and cfd codes," *Annals of Nuclear Energy*, vol. 189, p. 109842, 2023.

[81] A. Lindsay, G. Giudicelli, P. German, J. Peterson, Y. Wang, R. Freile, D. Andrs, P. Balestra, M. Tano, R. Hu, L. Zou, D. Gaston, C. Permann, and S. Schunert, "Moose navier–stokes module," *SoftwareX*, vol. 23, p. 101503, 2023.

[82] D. Grishchenko, M. Jeltsov, K. Kööp, A. Karbojian, W. Villanueva, and P. Kudinov, "The tall-3d facility design and commissioning tests for validation of coupled sth and cfd codes," *Nuclear Engineering and Design*, vol. 290, pp. 144–153, 2015. Thermal-Hydraulics of Innovative Nuclear Systems.

[83] W. Ma, E. Bubelis, A. Karbojian, B. R. Sehgal, and P. Coddington, "Transient experiments from the thermal-hydraulic ads lead bismuth loop (tall) and comparative trac/aaa analysis," *Nuclear Engineering and Design*, vol. 236, no. 13, pp. 1422–1444, 2006.

[84] S. J. Ball, M. Corradini, S. E. Fisher, R. Gauntt, G. Geffraye, J. C. Gehin, Y. Hassan, D. L. Moses, J.-P. Renier, R. Schultz, and T. Wei, "Next generation nuclear plant phenomena identification and ranking tables (pirts) volume 2: Accident and thermal fluids analysis pirts," 3 2008.

[85] Idaho National Laboratory, "WCNSFVSwitchableInletVelocityBC." https://mooseframework.inl.gov/source/fvbcs/WCNSFVSwitchableInletVelocityBC.html, 2024. Accessed: 2024-08-18.

[86] Idaho National Laboratory, "INSFVSwitchableOutletPressureBC." https://mooseframework.inl.gov/source/fvbcs/INSFVSwitchableOutletPressureBC.html, 2024. Accessed: 2024-08-18.

[87] J. Hord, "Comparison of incompressible flow and isothermal compressible flow formulae.:," 1967-01-01 05:01:00 1967.

[88] Z. Wu, D. Lin, and D. Zhong, "The design features of the htr-10," *Nuclear Engineering and Design*, vol. 218, no. 1, pp. 25–32, 2002.

[89] H.-J. Allelein and K. Verfondern, "Major milestones of htr development in germany and still open research issues," *Annals of Nuclear Energy*, vol. 116, pp. 114–127, 2018.

[90] Z. J. Ooi, G. Yang, T. Mui, L. Zou, and R. Hu, "Coupled sam/griffin model of a reference pebble bed high-temperature gas cooled reactor for multi-physics simulations," 10 2023.